

NORTHWESTERN UNIVERSITY

Inhibition of amyloid-beta aggregation and toxicity by cobalt(III) Schiff base

A DISSERTATION

SUBMITTED TO THE GRADUATE SCHOOL
IN PARTIAL FULFILLMENT OF THE REQUIREMENTS

for the degree

DOCTOR OF PHILOSOPHY

Field of Interdisciplinary Biological Sciences Program

By

Kaleigh Filisa Roberts

EVANSTON, ILLINOIS

December 2020

© Copyright by Kaleigh Filisa Roberts 2020

All Rights Reserved

ABSTRACT

Inhibition of amyloid-beta aggregation and toxicity by cobalt(III) Schiff base

Kaleigh Filisa Roberts

The interaction of amyloid- β ($A\beta$) with endogenous metal ions is thought to play a role in the pathogenesis of Alzheimer's disease (AD). However, limited tools exist to study and modulate $A\beta$ -metal binding. The Meade lab has developed cobalt(III) Schiff base (Co(III)-sb) complexes as protein inhibitors that competitively displace metals from proteins. This work describes the development of Co(III)-sb as both a tool for studying metal- $A\beta$ interactions and a therapeutic for ameliorating metal-mediated $A\beta$ toxicity in AD.

Effects of Co(III)-sb on $A\beta$ aggregation are explored using a multimethodological approach combining ThT fluorescence, CD spectroscopy, TEM, and AFM. In addition, kinetic aggregation data are modeled using AmyloFit yielding mechanistic insight into the effects of Co(III)-sb on the microscopic processes underlying $A\beta$ aggregation. Aggregation data on the effects of Co(III)-sb binding is further complemented with the addition of computational modeling using MD simulations. This work also explores competitive metal displacement, measurement of ROS and markers of oxidative stress, and effects of Co(III)-sb on $A\beta$ -mediated cellular toxicity. Finally, the last chapter outlines a secondary project towards the development of novel photocleavable contrast agents for TEM.

ACKNOWLEDGEMENTS

The first person I would like to thank is my husband Steve. The best and smartest thing I have done in these last five years is marry you. You have been by my side for all the ups and downs of this PhD. From driving in with me for midnight and 3 am plate reads because I was scared of science zombies in the deserted corridors to cooking and taking care of the pups while I pulled all-nighters before every single grant deadline, this achievement was only possible because of your extraordinary dedication to me and our family. I love and appreciate you sweetbear.

Next, I would like to thank my family. My interest in science was early and encouraged by unending support from my parents. From in-home tutors, to gifted programs, to allowing me to go away to IMSA, my parents gave me every academic opportunity I could hope for. Mom, you taught me resilience in the face of adversity. When I didn't get into an MD/PhD program on my first try, you forced me to suck it up and move forward (a critical skill in science). Dad, you taught me the importance of having fun (after all I started this journey because I loved science, even if it was sometimes easy to forget that). Tom, you taught me the importance of efficiency and practicality, and of translating my work in the lab to tangible real-world applications. Brittany, doing your science fair project every year grades 3-8 was excellent preparation for my PhD (especially when you got a higher ribbon than me). Lab work is often thankless, but our morning chats sustained me. Thank you for always supporting my dreams even when they have kept us geographically separated. Carol and Steve, you have truly made me feel so welcomed into your family and been so tremendously gracious providing meals and helping with the dogs. Without all this family support and sacrifice, I never would have made it in school for this long, and without you guys nagging me to go get a real job, I never would have finished.

Next, I would like to acknowledge my mentor, Tom. I entered your lab an orphan with little background in chemistry. You matched me with excellent mentors, gave me the resources I needed to succeed with experiments, and helped me grow as a scientist and a mentor. You have always supported my ideas and given me the freedom to dictate the direction of my projects. I will always cherish memories of you “spilling the tea” and “throwing shade” at Joy’s defense, your tour-guide like knowledge of the Tetons during I2020, and winning the bet about Sprite and beer and getting lunch for team Aß. Sophie, your influence on my time in the Meade lab was tremendous. Your door was always open and you were there when I needed to vent. I appreciate the countless hours you spent helping me to be a successful graduate student, taking walks to get coffee or snacks, and getting to craft with you at the tea party.

Special thanks to my thesis committee: Drs. Vassar, Klein, Bozza, and Holmgren for your wisdom and guidance over the years and your patience navigating my return to med school. Thank you also to the MSTP leadership for supporting me at every phase of training. Jayms, you have been my go-to since the beginning. I truly appreciate all the advice and look forward to being able to pop in for a chat more often!

I am especially grateful for the opportunities for mentorship that I gained working in the Meade lab. I was lucky enough to contribute to the training of 5 excellent mentees: Anna, Chris, Eleni, Joy, and Damonick. Anna, you were my first ever undergrad. To say I was nervous about taking you is an understatement, but getting to work with you was one of the best parts of my PhD. My favorite memories with you were when you obliterated Steve at MtG on his birthday, when we went to Renn Faire dressed as pirates, and shooting nerf guns in the office.

Chris, you entered the lab with such genuine enthusiasm for our project and have truly grown into the role of my lab little brother. From MtG/board game nights, to helping me decipher

chemistry despite my biologist brain, to even joining me for vegan food festivals, you have always been my right hand. I 100% could not have done this without you. Departing is easy knowing my projects are in such capable hands.

Eleni, girl did you keep me on my toes! You have an incredible way of interacting with people and are genuinely hilarious. Lab was never dull with all your shenanigans. My favorite memories are forcing Charlene to take the Meyer's Briggs personality test in the dark EM room and playing the "what are the odds" game (watching you eat old ketchup packets and saving you from trash can onions). I know you have a great medical career ahead of you (if you don't quit to open that deconstructed restaurant).

Joy, from the moment you joined the lab, team A β got so much cooler. In addition to being super hip, you also navigated an independent project to a manuscript in a few short years which was very impressive! Now you are off making bank and eating popcorn in industry. My favorite memories were all of our pop culture discussions and you introducing us all to Soondubu!

Damonick, my last mentee! I feel so grateful that I got to work with you. First you filled the coolness void left by Joy and Eleni, second you were always so genuinely enthusiastic to learn about the research. My favorite memories were you just randomly asking me questions about gravity in space or other random physics topics. Don't let grad school destroy that curiosity!

I am very grateful to the entire evolving Meade lab for continued support, discussion, and friendship during the last 5 years. Marie, thank you for being my first mentor in the Meade group and getting me started on my project. Your welcoming demeanor set the stage for my entire experience in the Meade group and I am so excited to watch your career advancement Professor! Ruby, you kept my gchat stocked with cute dog imgurs and were always available to answer synthesis questions for me. I appreciated all our MtG excursions, doggie play dates, rides to work,

and especially our double reindeer sweaters. Laura, you are like the female version of Steve (tatted up, strong, angry, Celtic, and so incredibly thoughtful and caring to your loved ones). I am so excited to follow your career and truly hope we can find a way to work together again in the future. Andrew, you were my second lab little brother. Getting to sit next to you the past 3 years was a pleasure, even if you were often being V weird. I will never forget the awesome antibody socks you brought me, being Mystic Twerps, or you wearing the sexy fireman suit. Luke, geeking out together over cool papers/Pacific Rim or inventing million dollar ideas (Power Pork™, CRISPR it into me™, Chocolate Lab™) for the wall kept me enthusiastic about science. Liz, your 3 am meme game is truly superb and I really appreciated getting the opportunity to work with you on the book chapter. To the young ladies of Meade lab (and QBIC) Shaunna, Becky, Meghan, and Megan: getting to know you guys was a pleasure and I hope we will still hang out after I'm gone. Remember to stick together: you are each other's best resources for success in grad school. A special shout out to my I2020 squad: Laura, Liz, Mike, and Nikhil. What a beautiful shitshow that trip was! Thanks Marco! Keith, Justin, Adam, Mike, Nikhil, Nat, Zhidong, Sarah, Matt, Robert, Dan Feld, Casey, Hao, and Tyler: each of were an important part of my grad school career. Even if we didn't directly work together, interacting with you guys was what made Meade lab special.

I would like to acknowledge my previous research mentors Randy Bateman and Skip Binder. Skip, you embodied dedication to the AD field. I came to NU to work for you and am grateful for our brief time together. Your memory lives on in those you taught and inspired. Randy, you taught me that the hardest problems are the most worthwhile and that tenacity is rewarded. You gave me an opportunity at a critical point in my career and truly shaped the entire trajectory of my life since then. I will always be striving to merit your overly high opinion of me.

Finally, thank you to my excellent friends who have not yet been mentioned (Natasha & Tino, Ben & Caitlin, Dave, Brooks & Jupiter, Danny, Mozes, Liz, Burke, and Bearchelle) for keeping me sane these last 5 years. Game nights were and will continue to be the highlight of my week! Special shout outs to Dr. Natasha PhD for doing such excellent work as my high school science lab partner that we were both inspired to get PhDs. Also to Tasha and Bearchelle, my Chandeladies, for getting to start my journey at NU living with such BAMFs. Finally extra thanks Ben and Jupiter for extending the resources of Jewett lab during my darkest plate reader hour.

One last acknowledgement to my furry babies: Buster, Shrimp, Buddy, Margaret, and Hazel. You sweet handsome boys made it so hard to go into lab, no wonder this took so long ☺

LIST OF ABBREVIATIONS

τ	aggregation lag time
2MeIm	2-methylimidazole
2PE	two-photon excitation
4MeIm	4-methylimidazole
7-OHCCA	7-hydroxycoumarin-3-carboxylic acid
A β	amyloid-beta
A β O	amyloid-beta oligomers
acacen	acetylacetonatoethylenediimine
AD	Alzheimer's disease
Ala	alanine
APP	amyloid precursor protein
APTES	aminopropyltriethoxysilane
AUC	area under the curve
BBB	blood brain barrier
BHT	butylated hydroxytoluene
BOC	tert-butoxycarbonyl
BSA	bovine serum albumin
C3Im	coumarin-3-imidazole
CCA	coumarin-3-carboxylic acid
CD	circular dichroism
CHCA	α -cyano-4-hydroxycinnamic acid

CMC	critical micellar concentration
Co(III)	cobalt 3+
Co(III)-sb	Cobalt(III) Schiff base
CoDiIm	Co(III) Schiff base 1,10-diimidazoldecane bridging ligands
CoIm	Co(III) Schiff base imidazole axial ligands
CoNH ₃	Co(III) Schiff base ammine axial ligands
conc	concentration
cryoEM	cryogenic electron microscopy
CSF	cerebrospinal fluid
Cu(I)	copper 1+
Cu(II)	copper 2+
DAB	diaminobenzidine
DCF	2,7-dichlorofluorescein
DCFDA	2,7-dichlorodihydrofluorescein diacetate
DCM	dichloromethane
DFT	density functional theory
DIPEA	<i>N,N</i> -Diisopropylethylamine
DMEM	Dulbecco's modified Eagle's medium
DMF	dimethylformamide
DMSO	dimethyl sulfoxide
DLS	dynamic light scattering
DSSP	define secondary structure of proteins
EDTA	ethylenediaminetetraacetic acid

EDX	energy-dispersive x-ray spectroscopy
ELISA	enzyme-linked immunosorbent assay
EM	emission
EMEM	Eagle's minimum essential medium
EMSA	electrophoretic mobility shift assay
EPR	electron paramagnetic resonance
eq	equivalent
ESI-MS	electrospray ionization mass spectrometry
EX	excitation
FIB	focused ion beam milling
FBS	fetal bovine serum
Fe(III)	iron 3+
FMOCC	fluorenylmethyloxycarbonyl
FSC	forward scatter
Ga(III)	gallium 3+
GAFF	general AMBER force field
HBTU	2-(1 <i>H</i> -benzotriazol-1-yl)-1,1,3,3-tetramethyluronium hexafluorophosphate
HEPES	4-(2-hydroxyethyl)-1-piperazineethanesulfonic acid
HFIP	1,1,1,3,3,3 hexafluoroisopropanol
His	histidine
HNE	4-hydroxy-2-nonenal
HPLC	high pressure liquid chromatography
ICP-MS	inductively coupled plasma mass spectrometry

Im	imidazole
IR	infrared
Ir(III)	iridium 3+
ISF	interstitial fluid
k_+	elongation rate constant
k_n	primary nucleation rate constant
k_{off}	depolymerization rate constant
L	axial ligand
LDH	lactate dehydrogenase
LTP	long term potentiation
Lys	lysine
MALDI	matrix assisted laser desorption ionization
MD	molecular dynamics
MDA	malondialdehyde
MeIm	methylimidazole
MeNH ₂	methylamine
Met	methionine
MNI	4-Methoxy-7-nitroindolinyl
MS	mass spectrometry
MTS	3-(4,5-dimethylthiazol-2-yl)-5-(3-carboxymethoxyphenyl)-2-(4-sulfophenyl)-2H-tetrazolium
MTT	3-(4,5-dimethylthiazol-2-yl)-2,5-diphenyltetrazolium bromide
m_0	initial monomer concentration

M_0	initial fibril mass concentration
MW	molecular weight
NAC	N-acetyl-L-cysteine
n_c	critical nucleus size for primary nucleation
NH_3	amine
NMR	nuclear magnetic resonance
P_0	initial fibril concentration
PBS	phosphate buffered saline
PDB	protein database
PS1	presenilin 1
PyBOP	benzotriazol-1-yl-oxytripyrrolidinophosphonium hexafluorophosphate
RESP	restrained electrostatic potential
Rh(III)	rhenium 3+
ROS	reactive oxygen species
rpm	rotations per minute
Ru(II)	ruthenium 2+
SD	standard deviation
SDS-PAGE	sodium dodecylsulfate polyacrylamide gel electrophoresis
SEC	size exclusion chromatography
SELDI-TOF	surface enhanced laser desorption ionization time of flight
SEM	standard error of the mean
SPPS	solid phase peptide synthesis
SSC	side scatter

TBA	thiobarbituric acid
TBHP	tert-butyl hydroperoxide
TF	transcription factor
ThT	thioflavin T
TEA	triethylamine
TFA	trifluoroacetic acid
TEM	transmission electron microscopy
untx	untreated
V(V)	vanadium 5+
VMD	visual molecular dynamics
XS	excess
ZF	zinc finger
Zn(II)	zinc 2+

Dedicated to the memory of those I lost along the way...

Yiayia and Papou, who sacrificed everything for family. My happiest childhood memories were at 1414 Anna. Alzheimer's disease stole your memories, but your impact will not be forgotten.

Grandma Ev, who made me print my NRSA application in size 20 font so she could read it. You exemplified scientific curiosity and were a wonderful role model for a young woman in science.

...and those I gained.

Posey, may you always want to be a scientist. I'll help you achieve your dreams in any way I can.
Sampito, may you always want to be a shark (just kidding, I hope you'll be a scientist too).

TABLE OF CONTENTS

Abstract.....	3
Acknowledgements.....	4
List of Abbreviations.....	9
List of Figures.....	21
List of Tables.....	25
CHAPTER 1	
1 Introduction: Overview and Review of Literature.....	26
1.1 Dissertation Overview.....	26
1.1.1 Motivations and Objectives.....	26
1.1.2 Dissertation Outline.....	26
1.2 Review of Literature.....	27
1.2.1 Amyloid- β aggregation.....	27
1.2.2 Metal Binding to A β	29
1.2.3 Oxidative Stress in AD.....	32
1.2.4 Downstream Mechanisms of A β Toxicity.....	33
1.2.5 Metal-targeted Tools and Therapeutics.....	34
1.2.6 Cobalt(III) Schiff Base Complex.....	39
1.3 Scope of this Work.....	47
1.4 Publication Information.....	47
CHAPTER 2	
2 Inhibition of Amyloid- β Aggregation with Cobalt(III) Schiff Base Complexes.....	48
2.1 Abstract.....	48

		17
2.2	Introduction.....	48
2.3	Materials and Methods.....	54
2.3.1	Thioflavin T Fluorescence.....	54
2.3.2	Circular Dichroism Spectroscopy.....	55
2.3.3	Transmission Electron Microscopy.....	56
2.3.4	Atomic Force Microscopy.....	57
2.3.5	Kinetic Fitting using AmyloFit.....	58
2.3.6	Negative Control Preparation.....	59
2.4	Results.....	59
2.4.1	Co(III)-sb Alters Aggregation Kinetics by ThT Fluorescence.....	59
2.4.2	Co(III)-sb Mechanistic Insight from Kinetic Fitting.....	63
2.4.3	Co(III)-sb Aggregation Inhibition by CD Spectroscopy.....	67
2.4.4	Co(III)-sb Alters Aggregate Morphology by TEM.....	71
2.4.5	Co(III)-sb Alters Size Distribution by AFM.....	73
2.4.6	Comparison of Negative Controls.....	75
2.5	Discussion.....	79
2.6	Acknowledgements.....	83
2.7	Publication Information.....	84
 CHAPTER 3		
3	Computational Modeling of Cobalt(III) Schiff Base Inhibition of Amyloid- β Aggregation	
3.1	Abstract.....	85
3.2	Introduction.....	85
3.3	Materials and Methods.....	88

		18
3.3.1	Parameterization of the Co(III)-sb Complex.....	88
3.3.2	Molecular Dynamics Simulations.....	98
3.3.3	Synthesis of [Co(acacen)(CH ₃ NH ₂) ₂]Cl.....	101
3.3.4	X-ray Crystallography.....	102
3.3.5	Amyloid-β preparation and Thioflavin T assay.....	105
3.4	Results.....	106
3.4.1	Monomeric Amyloid-β Simulations.....	106
3.4.2	Pentameric Amyloid-β Simulations.....	108
3.4.3	Experimental Aggregation Study.....	113
3.5	Discussion.....	115
3.6	Acknowledgements.....	117
3.7	Publication Information.....	118
 CHAPTER 4		
4	Inhibition of Metal-Mediated Amyloid-β Toxicity with Cobalt(III) Schiff Base Complexes.....	119
4.1	Abstract.....	119
4.2	Introduction.....	119
4.3	Materials and Methods.....	121
4.3.1	Aβ Oligomer Preparation.....	121
4.3.2	Cell Culture.....	122
4.3.3	Peptide Synthesis.....	122
4.3.4	Competitive Binding Studies.....	122
4.3.4.1	Dialysis.....	122

		19
4.3.4.2	Bead Binding Studies.....	123
4.3.5	ICP-MS.....	123
4.3.6	CCA Fluorescence.....	123
4.3.7	DCFDA Fluorescence in Cell Culture.....	124
4.3.8	CellROX Flow Cytometry.....	124
4.3.9	MDA Assay.....	125
4.3.10	MTS Toxicity.....	126
4.4	Results.....	127
4.4.1	Studies of Competitive Metal Displacement.....	127
4.4.2	Studies on ROS Generation.....	131
4.4.3	Toxicity Studies.....	137
4.5	Discussion.....	139
4.6	Acknowledgements.....	140
4.7	Publication Information.....	141

CHAPTER 5

5	TEMarkers: Photoactivatable Contrast Agents to Investigate Synaptogenesis by Transmission Electron Microscopy.....	142
5.1	Abstract.....	142
5.2	Introduction.....	143
5.3	Materials and Methods.....	147
5.3.1	First-Generation Agent Synthesis and Characterization.....	147
5.3.2	Transmission Electron Microscopy.....	149
5.3.3	Nile Red CMC Assay.....	151

		20
5.3.4	UV-Vis Spectroscopy.....	151
5.3.5	Cell Culture.....	151
5.3.6	Agarose Enrobing Procedure.....	152
5.3.7	MTS Toxicity.....	154
5.3.8	Second-Generation Agent Synthesis and Characterization.....	154
5.4	Results.....	156
5.4.1	First-generation agent characterization.....	156
5.4.2	Second-generation agent characterization.....	165
5.5	Discussion.....	173
5.6	Future Directions.....	174
5.7	Acknowledgements.....	177
 CHAPTER 6		
6	Summary and Future Directions.....	178
6.1	Summary.....	178
6.2	Future Directions.....	179
REFERENCES.....		181
Curriculum Vitae.....		202

LIST OF FIGURES

- Figure 1.1 General chemical structure of Co(III)-sb complexes
- Figure 1.2 Dissociative ligand exchange of Co(III)-sb
- Figure 1.3 Schematic of metal displacement from ZFTFs by Co(III)-sb
- Figure 1.4 Specific *in vivo* inhibition of Ci by Co(III)-Ci
- Figure 1.5 Effects of Co(III)-sb on A β oligomer formation
- Figure 2.1 Nucleation Elongation model from AmyloFit software
- Figure 2.2 CD spectra of protein secondary structures
- Figure 2.3 A β ₄₂ aggregation kinetics by ThT fluorescence
- Figure 2.4 AUC analysis of A β ₄₂ aggregation kinetics by ThT fluorescence
- Figure 2.5 A β ₄₀ aggregation kinetics by ThT fluorescence
- Figure 2.6 AUC analysis of A β ₄₀ aggregation kinetics by ThT fluorescence
- Figure 2.7 Half time log plots for kinetic fitting
- Figure 2.8 AmyloFit normalized kinetic curves
- Figure 2.9 Effects of Co(III)-sb on A β ₄₀ aggregation by CD spectroscopy
- Figure 2.10 A β ₄₀ aggregation by CD ellipticity at 218 nm over time
- Figure 2.11 Effect of Co(III)-sb on A β ₄₀ aggregate morphology by TEM
- Figure 2.12 Effect of Co(III)-sb on A β ₄₂ aggregate morphology by TEM
- Figure 2.13 Effect of Co(III)-sb on A β ₄₂ aggregate morphology by AFM
- Figure 2.14 AFM quantification of r-eq and Dmax
- Figure 2.15 A β isoform ratios aggregation kinetics by ThT fluorescence
- Figure 2.16 AUC analysis of A β isoform ratios aggregation kinetics by ThT

Figure 2.17 Structures of Co(III)-sb complexes used as negative controls

Figure 2.18 Negative controls AUC analysis of A β aggregation kinetics by ThT

Figure 3.1 DFT optimized geometry and crystal structure of Co(III)-sb

Figure 3.2 DSSP monomer simulation

Figure 3.3 Contact maps for monomer simulation

Figure 3.4 DSSP pentamer simulation

Figure 3.5 Number of hydrogen bonds between neighboring chains in the pentamer

Figure 3.6 Distance between neighboring chains in the pentamer

Figure 3.7 Average hydrogen bond number and distance between neighboring peptide chains in the pentamer

Figure 3.8 Percent β -sheet content in the pentamer at various equivalencies of Co(III)-sb

Figure 3.9 A β_{42} aggregation kinetics and AUC by ThT fluorescence

Figure 3.10 Comparison of aggregation inhibition by Co(NH₃)₂ vs. Co(MeNH₂)₂

Figure 4.1 Effect of Cu(II) and Co(III)-sb on Ab₄₂ aggregation by ThT fluorescence

Figure 4.2 Metal binding by dialysis with ICP quantitation

Figure 4.3 Metal displacement measured by CCA fluorescence

Figure 4.4 Flow cytometry distributions after treatment with TBHP measured by DCFDA fluorescence

Figure 4.5 Average DCFDA fluorescence from flow cytometry distributions after treatment with TBHP

Figure 4.6 Average DCFDA fluorescence from flow cytometry distributions after treatment with Ab, Cu(II), and Co(III)-sb

Figure 4.7 Flow cytometry distributions after treatment with TBHP measured by CellROX fluorescence

Figure 4.8 Average CellROX fluorescence from flow cytometry distributions after treatment with TBHP (oxidant) and NAC (antioxidant) in two different cell lines

Figure 4.9 MDA concentration in cells following treatment with A β O_s

Figure 4.10 Toxicity of Co(III)-sb in HT22 cells by MTS assay

Figure 4.11 Rescue of A β toxicity by Co(III)-sb in HT22 cells by MTS assay

Figure 5.1 TEMarker schematic

Figure 5.2 First-generation TEMarker structure

Figure 5.3 SPPS of first-generation TEMarker agent

Figure 5.4 London Finder grid

Figure 5.5 Schematic of agarose enrobing protocol

Figure 5.6 Second-generation TEMarker structures

Figure 5.7 Schematic of UV photocleavage of first-generation TEMarker

Figure 5.8 TEM contrast of perfluorocarbon tail

Figure 5.9 Demonstration of TEMarker photocleavage by MALDI

Figure 5.10 UV-Vis kinetics of photocleavage of TEMarker agent

Figure 5.11 First-generation TEMarker contrast by TEM following on grid activation by handheld UV lamp

Figure 5.12 Critical micellar concentration for first generation TEMarker as measured by Nile Red fluorescence

Figure 5.13 First-generation TEMarker toxicity by MTS assay

Figure 5.14 TEM images of agarose noodle embedded cells following two-photon activation

Figure 5.15 Second generation non-tail TEMarker contrast by TEM following on grid activation by handheld UV lamp

Figure 5.16 Second-generation tail TEMarker contrast by TEM following on grid activation by handheld UV lamp

Figure 5.17 Fluorescence imaging of grid from Figure 5.16c

Figure 5.18 Two-photon activation of TEMarker800 on London Finder grids for determination of blotting methodology

Figure 5.19 Two-photon activation of TEMarker800S on London Finder grid demonstrating spatial imprecision

LIST OF TABLES

Table 1.1 Coordination complexes for amyloid- β inhibition

Table 2.1 Global parameters from AmyloFit kinetic fitting

Table 2.2 Protein secondary structure assignment by CD

Table 3.1 Crystal data and structure refinement for $[\text{Co}(\text{acacen})(\text{CH}_3\text{NH}_2)_2]\text{Cl}$

Table 3.2 RESP Partial charges and GAFF atom types for Co(III)-sb calculated from DFT minimized structure

Table 3.3 Bonded (bonds, angles, dihedrals) and nonbonded parameters for additional atom types (CO, nr, nl, ox,oy) used in Co(III)-sb from DFT geometry optimization

Table 3.4 Crystal Structure Fractional Atomic Coordinates ($\times 10^4$) and Equivalent Isotropic Displacement Parameters ($\text{\AA}^2 \times 10^3$) for cx1210a. U_{eq} is defined as 1/3 of of the trace of the orthogonalised U_{ij} tensor.

Table 3.5 Crystal Structure Bond Lengths for $[\text{Co}(\text{acacen})(\text{CH}_3\text{NH}_2)_2]\text{Cl}$

Table 3.6 Crystal Structure Bond Angles for $[\text{Co}(\text{acacen})(\text{CH}_3\text{NH}_2)_2]\text{Cl}$

CHAPTER 1

Introduction: Overview and Review of Literature**1.1 Dissertation Overview****1.1.1 Motivations and Objectives**

The interaction of amyloid- β ($A\beta$) with endogenous metal ions is thought to play a role in the pathogenesis of Alzheimer's disease (AD). However, limited tools exist to study and modulate $A\beta$ -metal binding. The Meade lab has developed cobalt(III) Schiff base (Co(III)-sb) complexes as protein inhibitors that competitively displace metals from proteins. This work details the development of Co(III)-sb as both a tool for studying metal- $A\beta$ interactions and a therapeutic for ameliorating metal-mediated $A\beta$ toxicity in AD.

1.1.2 Dissertation Outline

The remainder of Chapter 1 will be a thorough review of the pertinent literature including background on AD, $A\beta$, coordination complexes, and Co(III)-sb in particular. In Chapter 2, I will discuss the *in vitro* effects of Co(III)-sb on $A\beta$ aggregation using a variety of protein aggregation assays. In Chapter 3, I will describe a collaborative project involving computational modeling of Co(III)-sb inhibition of $A\beta$ aggregation. Chapter 4 will cover experiments measuring the ability of Co(III)-sb to displace metal ions from $A\beta$ and decrease $A\beta$ -mediated generation of reactive oxygen species (ROS) and toxicity. Chapter 5 will describe my secondary project developing photoactivatable contrast agents for transmission electron microscopy (TEMarkers). In Chapter 6, I will summarize my work and outline future directions for the development of Co(III)-sb complexes as $A\beta$ inhibitors.

1.2 Review of Literature

The amyloid- β ($A\beta$) peptide is a key mediator in the etiology of Alzheimer's disease (AD), the most common form of age-related dementia and 6th leading cause of death in the US [1, 2]. Significant data has implicated $A\beta$'s interaction with endogenous metal ions in the pathogenesis of AD, however the precise effects of metal binding remain controversial [3, 4]. $A\beta$ binds transition metals Cu(II), Zn(II), and Fe(III) with high affinity at the N-terminal histidines (His) residues and this binding has been shown to affect both aggregation and toxicity of $A\beta$ [4-7]. Experiments modulating metal ion concentrations have demonstrated that metal ions accelerate $A\beta$ aggregation and act to stabilize conformations that lead to the production of toxic aggregates [8-10]. As such, modulation of $A\beta$ -metal interactions has emerged as a prominent therapeutic strategy for the treatment of AD.

1.2.1 Amyloid- β Aggregation

There is strong evidence linking disruption in the metabolism of $A\beta$ to AD.[11] *In vivo*, $A\beta$ is generated by sequential cleavage of the amyloid precursor protein (APP) by β -secretase and γ -secretase. The two primary isoforms of $A\beta$ are $A\beta_{40}$ and $A\beta_{42}$, which differ in sequence only by two additional hydrophobic amino acids at the C-terminus in $A\beta_{42}$. $A\beta_{40}$ is the most abundant isoform, while $A\beta_{42}$ more readily aggregates and is therefore believed to be the more pathogenic isoform.

Either through over-production or under-clearance, $A\beta$ accumulates as amyloid plaques in the AD brain [2]. Pathologically, AD is characterized by both amyloid plaques composed of $A\beta$ and intracellular aggregates composed of hyperphosphorylated microtubule-associated protein tau.

Disruptions in tau processing are common to many neurodegenerative disorders, and in the case of AD, generally believed to be downstream of A β toxicity [12]. The precise mechanism by which these pathological changes induce synaptic dysfunction and neurodegeneration remains unknown.

AD is one example of a broader group of disorders known as amyloidoses, which are characterized by the conversion of soluble innocuous proteins into insoluble amyloid fibrils [13]. Amyloid is a generic protein quaternary structure consisting of long unbranched fibrils with cross- β structure that are formally defined by exhibition of green birefringence under cross-polarized light when stained with the dye Congo Red [13]. Amyloid plaques are a common phenomenon in neurodegenerative diseases including Parkinson's disease (α -synuclein), Lewy Body dementia (α -synuclein), and Creutzfeldt-Jakob disease (prion protein), but can also be observed in other diseases including cancer and diabetes [13].

Despite difficulty with crystallization, structural information on amyloid fibrils has been gained through NMR, cryo-EM, and x-ray diffraction studies [14, 15]. As amyloids aggregate, the initially unstructured monomers adopt a β -turn- β conformation where residues 1-17 are unstructured, 18-26 form β -strand 1, 27-30 comprise the turn, and 31-42 form the antiparallel β -strand 2 [14]. Monomers then stack perpendicular to the long axis in an array of conformations to form fibrils ~10 nm in diameter with length up to the micron scale [13].

Amyloid aggregation follows a sigmoidal growth curve and has been described as nucleation-dependent polymerization. An initial lag phase corresponds to nucleation, wherein monomers form oligomeric seeds for aggregation. This is followed by a rapid growth polymerization phase that eventually plateaus once equilibrium between A β monomers, oligomers, and fibrils has been reached [13]. A broad spectrum of oligomeric species have been identified both *in vivo* and *in vitro*. However, structural studies of A β oligomers are challenging

due to their polymorphism and transient nature [7]. Although it remains unclear whether A β oligomers represent intermediates to fibril formation or distinct aggregation pathways, significant data has implicated oligomers as the toxic species of A β [12, 16-18]. While both monomers and fibrils are relatively inert toward neurons, oligomer toxicity has been demonstrated using both *in vitro* aggregation of synthetic A β and *ex vivo* isolation of soluble oligomers from AD brain [17]. Additionally, soluble A β oligomers better correlate to synaptic loss and markers of disease severity than insoluble plaques *in vivo*, making oligomeric species the most likely etiologic agent and a promising target for therapeutic strategies [19, 20].

Aggregation of A β is modulated by a variety of factors including metal binding, peptide concentration, buffer composition, temperature, agitation, molecular crowding, and pH [21, 22]. These factors affect generation of both oligomers and fibrils since both processes require the self-association of A β . In order to study the amyloid aggregation pathway, purified or synthetic A β can be aggregated *in vitro* [23]. *In vitro* aggregation kinetics have been shown to correlate to rates of disease progression in AD patients and animal models and represent a useful metric for testing A β -targeted therapeutics [24-26]. However, the dependence of aggregation assays on such a large number of variables and lack of standardization in protein preparation or assay setup has resulted in wide variability in published A β aggregation data. As such, it is generally accepted that multiple techniques should be employed for optimal characterization of A β aggregation [27, 28].

1.2.2 Metal Binding to A β

Significant evidence implicates metal ions in the pathogenesis of AD. Early work identified drastic disruptions in metal homeostasis in AD patients and animal models [29]. For example,

amyloid aggregates extracted from human AD brain show high (μM - mM) levels of Cu(II) and Zn(II) directly bound to $\text{A}\beta$ [30]. However, total brain levels of the metals remain unchanged, indicating significant miscompartmentalization [31]. Further, addition of chelators results in partial dissolution of the plaques, implicating metals in the aggregation process [32]. Experiments using animal models of AD also illustrate the importance of metal ions. Genetic manipulations disturbing zinc and copper metabolism alter $\text{A}\beta$ metabolism in transgenic mice and chelators have shown cognitive benefits when used as therapeutics [33, 34]. Additionally, extensive *in vitro* work has demonstrated the ability of metal ions to alter aggregation and modulate toxicity of $\text{A}\beta$ [35-37].

In order to better understand the role of metals in the AD brain, the specific binding interactions between $\text{A}\beta$ and metal ions have been characterized by a variety of structural techniques *in vitro*. Cu(II) , Zn(II) , and Fe(III) coordinate $\text{A}\beta$ in a 1:1 stoichiometry at the same binding site [35]. Cu(II) has two separate binding modes (Component I and Component II), which both have square planar geometry. In Component I, Cu(II) coordination is mediated by the N-terminal amine nitrogen of Asp1, the carbonyl oxygen of the Asp1-Ala2 amide bond, the imidazole nitrogen of His6, and the imidazole nitrogen of either His13 or His14 [38, 39]. In Component II, Cu(II) is coordinated by the N-terminal amine nitrogen of Asp1, the deprotonated nitrogen of the Asp1-Ala2 amide bond, the carbonyl of the Ala2-Glu3 peptide bond, a one imidazole nitrogen of a His residue with no preference for which one [39]. Zn(II) coordination is more poorly defined, but is also thought to include the imidazole side chains of His6, His13, and His14 in a tetrahedral geometry [39-42].

In all cases, the metal coordination site is restricted to the N-terminal portion of the peptide, which is common to both $\text{A}\beta_{40}$ and $\text{A}\beta_{42}$ isoforms and remains outside of the β pleated core formed

by residues 18-42 as A β aggregates. *In vitro* studies of metal ion binding to A β show that Cu(II) and Zn(II) bind to monomeric or fibrillar A β with identical affinity and coordination geometry, suggesting that metal-binding is independent of the aggregation state of A β [41, 43].

As with studies of A β aggregation, reported metal ion binding affinities vary greatly due to variation in experimental conditions [44]. The binding affinity for Cu(II) ranges from attomolar to nanomolar, while the binding affinity for Zn(II) is in the low micromolar range [35, 41, 45-51]. These low affinities make binding unlikely at the physiological Cu(II) and Zn(II) concentrations in cerebrospinal fluid (CSF) [52]. However, transient synaptic release of labile metal ions during neurotransmission can raise local concentrations significantly, allowing association with A β . Zn(II) is classically released in synaptic vesicles by a subset of glutamatergic neurons [52, 53]. Following release, synaptic concentrations of Zn(II) increase to 200-300 μ M before reuptake into neurons. The released zinc is considered a labile pool because it is not tightly bound to biological ligands, and is therefore able to interact with weaker ligands at the synapse including A β [38]. Likewise, evidence suggests that copper can also be released into the synaptic cleft during neurotransmission [54]. A similar labile pool of Cu(I/II) is present in some glutamatergic neurons and can raise synaptic copper concentrations to 10-100 μ M [4, 38]. Because A β processing is also localized to the synaptic cleft, it is thought that the interaction between A β and the labile Zn(II) and Cu(II) pools may initiate aggregation [55].

Metal ions have been shown to affect both the morphology of amyloid aggregates and the kinetics of aggregation. Possible mechanisms for metal-induced protein aggregation include amyloidogenic rearrangement of the peptide by metal coordination, intermolecular crosslinking between monomers, stabilization of species that facilitate aggregation, destabilization of non-

pathogenic structures, and oxidative modifications of the peptide that increase aggregation due to metal catalyzed redox reactions [7]. Initial studies showed that Zn(II) and Cu(II) markedly accelerate A β aggregation [35, 36]. Another early study concluded that A β aggregation *in vitro* does not occur if metal ions are rigorously excluded, further stressing the role of metal ions in A β aggregation [56]. However, more recent studies have reported diverse and contradictory results. Cu(II) has been shown to accelerate fibrillization kinetics,[57] inhibit fibril formation by promoting amorphous aggregation,[58-60] and stabilize oligomeric species [61, 62]. Similar contradictory results have been reported for Zn(II) [7, 46, 58, 63, 64]. A study demonstrating that the effect of metal binding depends on the stoichiometric ratio between A β and metal ions may partly explain the broad spectrum of reported results [57]. Additionally, variable experimental conditions and different assays for monitoring aggregation contribute to the poor agreement within the literature.

1.2.3 Oxidative Stress in AD

Oxidative stress has been identified as a key component of AD pathology and a potential mechanism for A β -induced neurotoxicity. High oxygen consumption, relatively low antioxidant levels, and limited regenerative potential make the brain particularly susceptible to this type of damage [4]. Oxidative stress in the brain is generated by the redox active metal ions Cu(II) and Fe(III), which activate molecular oxygen and generate reactive oxygen species (ROS) [3]. For this reason, these metals are rigorously regulated by numerous binding proteins [3].

In addition to altering aggregation, metal binding to the N-terminal His residues of A β has demonstrated importance in modulating its neurotoxicity [65, 66]. Metal-mediated production of H₂O₂ by A β has been observed for both Cu(II) and Fe(III) *in vitro*, but Fe(III) is not anticipated to

play a significant role *in vivo* [10, 67]. A β -mediated reduction of Cu(II) to Cu(I) is thought to be the primary physiologic mechanism for A β generation of ROS *in vivo* through activation of molecular oxygen and formation of superoxide [8, 68]. Superoxide is then rapidly converted to H₂O₂, which readily diffuses across membranes and can generate downstream highly reactive free radicals by Fenton and Haber-Weiss chemistry [4]. A β -mediated generation of ROS by reduction of Cu(II) induces oxidation of another species. The most likely candidate within the A β peptide is the sulfur of Met35. Studies isolating A β oxidized at Met35 and bound to copper support this redox scheme [69]. Alternatively, biological reducing agents such as dopamine, cholesterol, or ascorbate may be oxidized, allowing redox cycling of the metal ion without net oxidation of the A β peptide [10].

Unlike Cu(II) and Fe(III), Zn(II) is not redox active and does not generate ROS. When Cu(II) and Zn(II) ions are co-incubated with A β peptides, redox inactive Zn(II) suppresses Cu(II)-mediated H₂O₂ production by competitively displacing Cu(II) ions from the metal binding site [70]. Concordantly, Cu(II)-binding increases A β toxicity to cultured cells, while Zn(II)-binding decreases toxicity in a concentration-dependent manner [4, 66]. Observations that addition of the H₂O₂-degrading enzyme catalase or metal chelators decreases A β toxicity to cultured neurons, further support Cu(II)-generated H₂O₂ as a likely mediator for neuronal damage [10, 71].

1.2.4 Downstream Mechanisms of A β Toxicity

The precise mechanism by which A β leads to cellular toxicity is widely debated and likely multifactorial. There is evidence for involvement of many mechanisms including oxidative stress, disrupted biometal homeostasis, aberrant calcium signaling, impaired axonal transport, altered

membrane integrity, mitochondrial dysfunction, and pathologic tau processing [72]. While Cu(II)-binding is not thought to be exclusively responsible for A β cytotoxicity, it can be linked to many of the other pathologic mechanisms [57]. Likely a variety of both downstream and parallel processes contribute to the complex physiologic dysregulation leading to synaptic dysfunction and neuronal cell death in AD. While the precise mechanisms of neurotoxicity in AD are not elucidated, disruption of Cu(II)-binding represents an ideal therapeutic target as ROS generation is an early pathologic event that is involved in other proposed mechanisms.

1.2.5 Metal-targeted Tools and Therapeutics

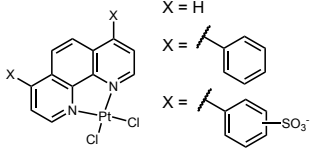
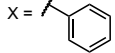
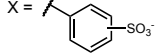
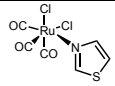
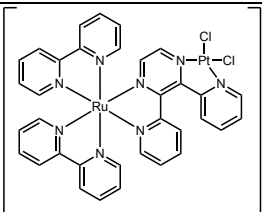
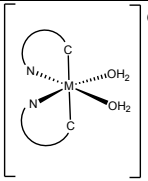
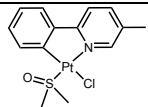
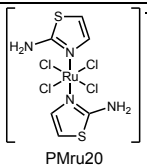
The current toolbox for studying and modulating A β -metal interactions is limited. Early studies used metal chelation to experimentally control metal ion concentrations [56]. The use of organic chelators targeting Cu(II) and Zn(II) has allowed precise modulation of metal concentrations *in vitro* and facilitated much of the structural work on metal-binding [32, 63]. Chelators have also been applied *in vivo* for mechanistic studies of metal-binding [34]. Promising results of metal chelation in animal models led to the development of several chelating drugs, some of which are currently in clinical trials [73-75].

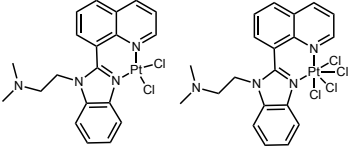
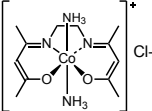
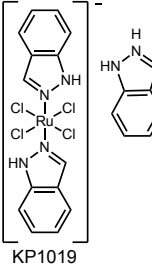
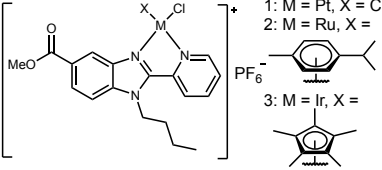
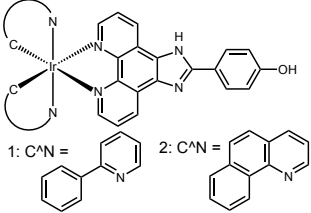
However, metal chelation both as a research tool and as a therapeutic approach has significant drawbacks including decreased bioavailability of necessary metal ions, poor metal selectivity, and inability to disrupt interactions between the metal-binding site and unchelated metals [76, 77]. Additional evidence that endogenous metal levels are not elevated, only miscompartmentalized, in the AD brain, further argues against the strategy of removing metal ions via chelation in favor of a strategy that prevents the metal ions from binding to the A β peptide [31].

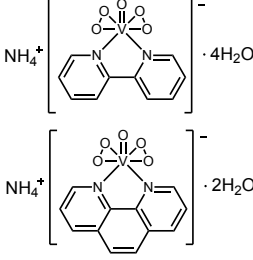
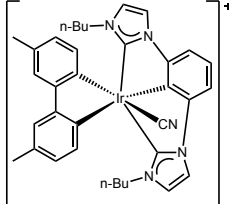
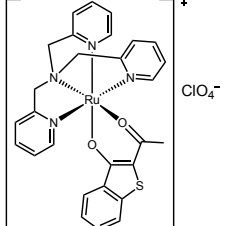
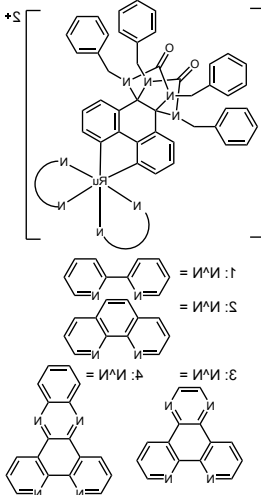
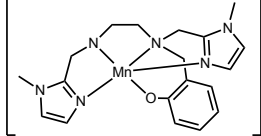
The most promising of the early metal-targeted compounds, PBT2, was developed by Prana and worked as an ionophore translocating Cu(II) and Zn(II) into the cell from the extracellular space in order to prevent the interaction with A β [74]. Despite promising preclinical results where it rescued dendritic spine loss in mouse models of AD and human Phase 1 clinical trials where it lowered CSF A β levels and led to improvement in individual cognitive function tests, PBT2 eventually failed in Phase 2 trials in 2014. Two new Phase 1 trials are currently recruiting participants to reexamine the effects of food and caffeine on PTB2 pharmacokinetics.

In 2008, Barnham et. al. pioneered the first transition metal complex-based approach targeting the N-terminal His residues of A β with a class of Pt(L)Cl₂ complexes where L represents bidentate phenanthroline ligands [78]. By coordinating to the His residues implicated in metal ion binding, these compounds effectively decreased Cu(II)-mediated aggregation and generation of ROS, rescued neuronal viability, and restored disruptions in long-term potentiation [78]. Since 2008, mechanistic work on Pt(L)Cl₂ complexes has revealed that the strong coordination of Pt(II) to A β is able to competitively displace Cu(II) and Zn(II) ions from A β and reverse metal-induced aggregation [79-81]. The efficacy of Pt(L)Cl₂ compounds stimulated the development and characterization of more cyclometallated Pt(II) compounds [81-83]. In addition, transition metal complexes have been expanded to include Ru(II), Ir(III), Rh(III), and V(V) coordination compounds that have shown promise as anti-AD therapeutics *in vitro* [84, 85]. The success of these preliminary compounds validates the use of coordination to kinetically inert metal centers for amyloid inhibition and illustrates the necessity for further development (**Table 1.1**).

Table 1.1: Coordination complexes for amyloid- β inhibition.

Structure	Effects	Ref
 <p>X = H X =  X = </p>	<ul style="list-style-type: none"> • Bind to Aβ_{42} by SELDI-TOF MS and Aβ_{40} by NMR • Alter Aβ_{42} secondary structure by CD • Inhibit Aβ_{42} aggregation by ThT fluorescence • Decrease Aβ_{42}:Cu(II) mediated H₂O₂ production • Increase cell viability following treatment with Aβ_{42} by MTS assay • Rescue Aβ_{42} inhibition of LTP in rodent hippocampal slice 	[78]
	<ul style="list-style-type: none"> • Binds to Aβ_{28} by NMR and ESI-MS • Alters Aβ_{28} secondary structure by CD 	[86]
 <p>Cl₂</p>	<ul style="list-style-type: none"> • Inhibits Aβ_{42} aggregation by ThT fluorescence • Inhibits Aβ_{42} formation of small oligomers by SDS-PAGE • Discovered distinct binding mode compared to Pt(II) complexes by SEC and MALDI-TOF MS 	[87]
 <p>OTf</p> <p>ppy bzq phq</p> <p>1: M = Ir(III), C[∧]N = ppy 2: M = Rh(III), C[∧]N = ppy 3: M = Ir(III), C[∧]N = bzq 4: M = Ir(III), C[∧]N = phq</p>	<ul style="list-style-type: none"> • Bind to Aβ_{40} by ESI-TOF MS • Inhibit Aβ_{40} aggregation by ThT fluorescence • Decrease fibril length and density by TEM • Ir(III) complexes shows switch-on luminescence upon binding to Aβ_{40} 	[88]
	<ul style="list-style-type: none"> • Binds to Aβ_{28} by NMR and ESI-MS • Coordinates to Aβ_{28}:Cu(II) by EPR 	[82]
 <p>PMru20</p>	<ul style="list-style-type: none"> • Decreases Aβ_{42} toxicity in rodent primary cortical neurons by LDH assay • Binds to Aβ_{42} by ESI-MS • Inhibits Aβ_{42} aggregation by ThT fluorescence 	[85]

	<ul style="list-style-type: none"> • Inhibits Aβ_{42} aggregation by ThT fluorescence • Decreases formation of Aβ_{42} dimer by SELDI-TOF MS • Increases cell viability following treatment with Aβ_{42} by MTS assay • Rescues Aβ_{42} inhibition of LTP in rodent hippocampal slice • Reduces Aβ_{42} levels and plaque number in APP/PS1 mouse model of AD 	[83]
	<ul style="list-style-type: none"> • Binds to Aβ_{16} by ESI-MS and NMR • Stabilizes formation of large Aβ_{42} oligomers and reduces small oligomers by SDS-PAGE • Decreases binding of Aβ_{42} oligomers to synapses in mouse primary neurons 	[89]
 <p>KP1019</p>	<ul style="list-style-type: none"> • Inhibits Aβ_{40} and Aβ_{42} aggregation by ThT fluorescence • Coordinates to Aβ_{28} by EPR • Stabilizes high MW oligomers by native gel electrophoresis and Western blotting • Rescues differentiated SH-SY5Y cells from Aβ_{42}-induced toxicity 	[90]
 <p>1: M = Pt, X = Cl 2: M = Ru, X = 3: M = Ir, X =</p>	<ul style="list-style-type: none"> • Compounds 1-3 inhibit Aβ_{42} aggregation by ThT fluorescence • Compound 3 rescues primary cortical neurons from Aβ_{42}-induced toxicity 	[91]
 <p>1: C^N = 2: C^N =</p>	<ul style="list-style-type: none"> • Inhibit Aβ_{40} aggregation by ThT fluorescence • Exhibit enhanced luminescence in the presence of Aβ_{40} monomers or fibrils • Rescue SH-SY5Y cells and mouse primary cortical neurons from Aβ_{40}-induced toxicity 	[92]

	<ul style="list-style-type: none"> • Inhibit Aβ_{42} aggregation by ThT fluorescence • Alter Aβ_{42} secondary structure by CD • Alter Aβ_{42} aggregate morphology by AFM • Reduce Aβ_{42} particle size by DLS • Bind to Aβ_{42} by NMR and ESI-MS • Rescue SH-SY5Y cells from Aβ_{42}-induced toxicity by MTT assay 	[93]
	<ul style="list-style-type: none"> • Inhibits Aβ_{40} aggregation by ThT fluorescence and TEM • Exhibits enhanced luminescence in the presence of Aβ_{40} monomers or fibrils 	[94]
	<ul style="list-style-type: none"> • Inhibits Aβ_{40} aggregation by ThT fluorescence and TEM 	[95]
	<ul style="list-style-type: none"> • Inhibit Aβ_{40} aggregation by ThT fluorescence and TEM • Inhibit acetylcholinesterase activity 	[96]
	<ul style="list-style-type: none"> • Removes Cu(II) from Aβ via metal swapping • Decreases ROS production by ascorbate consumption assay 	[97]

1.2.6 Cobalt (III) Schiff Base Complex

The Meade group has done extensive research developing Co(III)-sb complexes as protein inhibitors [80, 89, 98-111]. The complexes consist of an acetylacetonatoethylenediimine (acacen) Schiff base coordinated to an octahedral Co(III) center in the four equatorial positions ([Co(acacen)(L)₂]⁺, **Figure 1.1**). A variety of labile axial ligands (L) can be incorporated including amines (NH₃), methylamines (MeNH₂), 2-methylimidazoles (2MeIm), and 4-methylimidazoles (4MeIm).[109] . In solution, Co(III)-sb undergoes dissociative ligand exchange of the labile axial ligands allowing coordination to structurally or functionally important histidine (His) residues in proteins (**Figure 1.2**). Previous work has provided extensive characterization of the structural, spectroscopic, and electrochemical properties of Co(III)-sb [98, 109, 110].

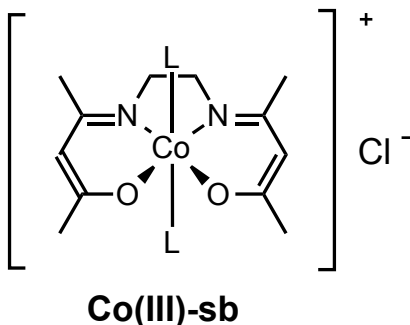


Figure 1.1: Cobalt(III) center stabilized by equatorial acacen Schiff base. Following dissociation of labile axial ligands L (where L= NH₃, MeNH₃, Im, 2MeIm, or 4MeIm), Co(III)-sb coordinates imidazole nitrogens of His residues.

Past work from our group has demonstrated the ability of Co(III)-sb to inhibit diverse proteins including enzymes (α -thrombin, thermolysin, and MMP-2) and transcription factors

(TF).[80] In particular, significant work has developed targeted Co(III)-sb complexes for the inhibition of Cys₂His₂ zinc finger transcription factors (ZFTF) [100, 107, 108]. ZFTFs are metalloproteins containing zinc finger motifs that are structurally stabilized by Zn(II)-binding and crucial for specific DNA recognition. Aberrant signaling by zinc finger transcription factors is implicated in cancer, thus specific inhibitors have potential therapeutic utility [80].

The key roles that ZFTFs play in oncogenesis, tumor proliferation and growth, and metastasis make them highly desirable targets for therapeutic intervention. A lack of hydrophobic binding pockets make these proteins difficult to target with traditional organic molecules, but their coordination chemistry can be exploited for potential therapeutic effect [112]. A large class of ZFTFs contain Cys₂His₂ structural motifs that tetrahedrally coordinate Zn(II) ions through cysteines and histidines. Moreover, Zn(II) coordination is required for sequence-specific DNA recognition and gene regulatory function [113]. Octahedral Co(III)-sb complexes, however, are able to displace Zn(II) and bind in its place, thereby disrupting protein structure and impairing DNA recognition and transcriptional activity (**Figure 1.3**). Since ZFTFs bind their consensus DNA with sequence-specificity, selective targeting can be achieved by conjugating Co(III)-sb to oligonucleotides with high affinity for the protein of interest.

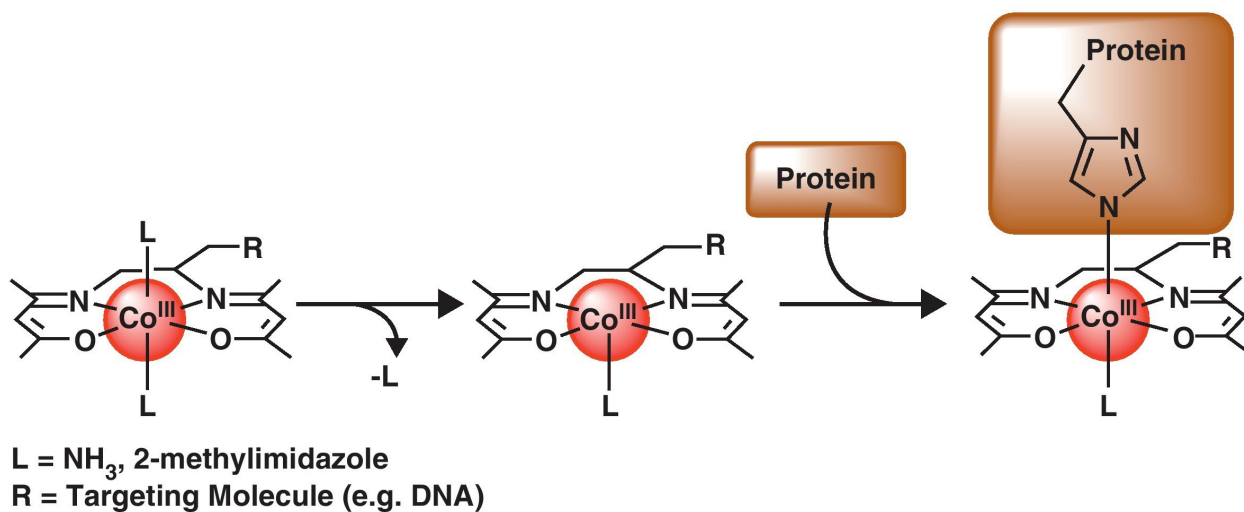


Figure 1.2: Co(III)-sb complexes undergo dissociative ligand exchange of the labile axial ligands to irreversibly bind His residues in biological settings. This mechanism can be exploited for therapeutic use where His residues are structurally or catalytically necessary for protein function. Figure reproduced with permission from [114].

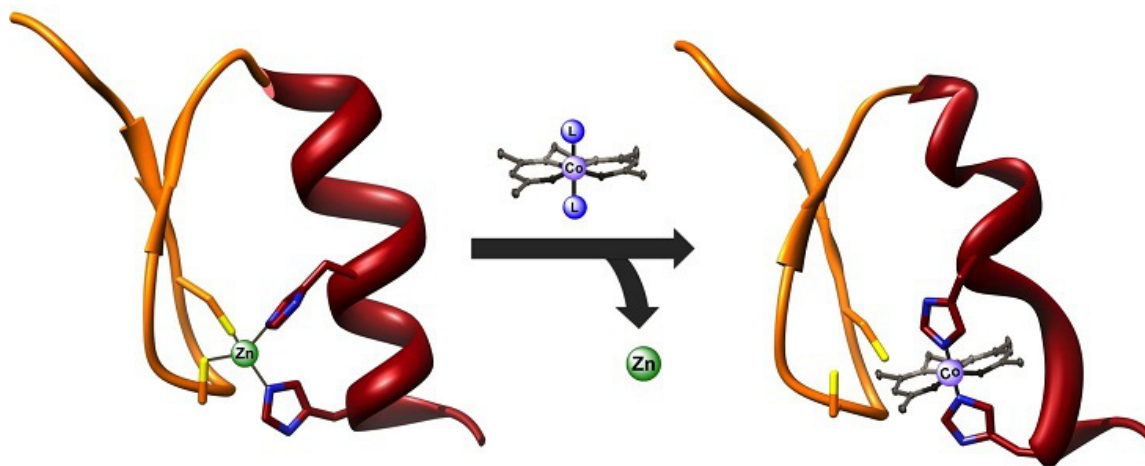


Figure 1.3: Proposed mechanism of inhibition of ZTFs by Co(III)-sb. The complex coordinates to His residues in zinc finger motifs through dissociative ligand exchange of axial ligands, thereby displacing Zn(II) and disrupting protein structure. Figure reproduced with permission from [103].

Specific inhibition of TFs has been achieved by conjugating the consensus DNA sequence of the TF of interest to the Co(III)-sb complex via peptide coupling to a pentanoic acid linker off the acacen backbone (seen as R group in **Figure 1.2**). The conjugated oligonucleotide mimics the native binding partner of the protein [99]. The remarkable effectiveness of these agents has been demonstrated with inhibition of the Snail and Ci transcription factors in *Xenopus* and *Drosophila* embryonic models, respectively [101, 111, 115].

Co(III)-sb targeted with the Ebox sequence (Co(III)-Ebox) binds selectively and irreversibly to Snail ZFTFs [99]. Specificity of binding was investigated using electrophoretic mobility shift assays (EMSA) in *X. laevis* embryo lysates. After overexpressing various control proteins in embryos, the resulting lysates were challenged with ³²P-labeled probes. Co(III)-Ebox bound to the Snail family proteins (Snail1, Snail2, and Sip1), but did not bind a non-Snail family ZFTF, a non-ZFTF that binds Ebox, or a non-ZFTF/non-Ebox binding protein. To investigate the irreversibility of inhibition, ³²P-labeled Co(III)-Ebox was incubated lysates overexpressing Snail2 protein and challenged with unlabeled probe. Co(III)-Ebox remained bound to Snail2 even after being challenged with 100-fold unlabeled Ebox, while the same ³²P-labeled Ebox without Co(III)-sb was displaced after being challenged by 33-fold of unlabeled Ebox [99]. Co(III)-Ebox was subsequently tested *in vivo* with *X. laevis* embryos at varying stages of development to demonstrate its utility in live animals [101]. Co(III)-Ebox successfully inhibited known functions of Snail in the formation and migration of neural crest cells, and specificity was demonstrated by a series of controls as well as retention of normal development of the central nervous system and mesoderm formation [101].

Similarly, a Co(III)-sb complex (Co(III)-Ci) targeted to Ci ZFTF was synthesized and tested *in vitro* and in a *Drosophila* embryo model [115]. The ability of Co(III)-Ci to inhibit Ci

from binding its DNA target was evaluated *in vitro* with protein extracts and *D. melanogaster* cells (S2 cells). As was found in the Co(III)-Ebox studies, Co(III)-Ci demonstrated potent and specific inhibition of its ZFTF target. Moreover, mutating the targeting sequence by one base pair or replacing it with a different sequence altogether precluded inhibition of DNA binding by Ci. Live cell studies demonstrated inhibition as well, wherein a luciferase reporter gene for Ci's target pathway was used. Co(III)-Ci was able to significantly decrease transcriptional activation by Ci [115]. Next, *in vivo* studies in developing *D. melanogaster* embryos were performed. In these embryos, Ci plays a major role in denticle belt formation, and genetically mutated *ci*⁹⁴ null exhibits abnormal fusion of the segments. Treatment of embryos with Co(III)-Gli resulted in localized fusion where the agent was injected, mimicking the *ci*⁹⁴ null phenotype (**Figure 1.4**) [115]. In a complementary experiment in which Ci is truncated into its repressor form but retains its ZF binding domain and sequence-specific DNA recognition, Co(III)-Ci could rescue denticle belt segmentation. This demonstrates that Co(III)-Ci can selectively inhibit Ci in both its activator or repressor form in an *in vivo* embryo model [115].

These biological investigations lay the groundwork for significant advancements in the field of targeted cancer therapeutics. Both ZFTFs for which selective inhibition has been demonstrated, Snail family and Ci, are heavily implicated in cancer-associated pathways. Overactivity of Snail proteins has been linked to epithelial-to-mesenchymal transition in cancer metastasis, while Ci regulates the hedgehog pathway associated in basal cell carcinoma and medulloblastoma. However, the modularity of the Co(III)-sb agent allows for targeting of many proteins of interest, granting the platform much broader applicability.

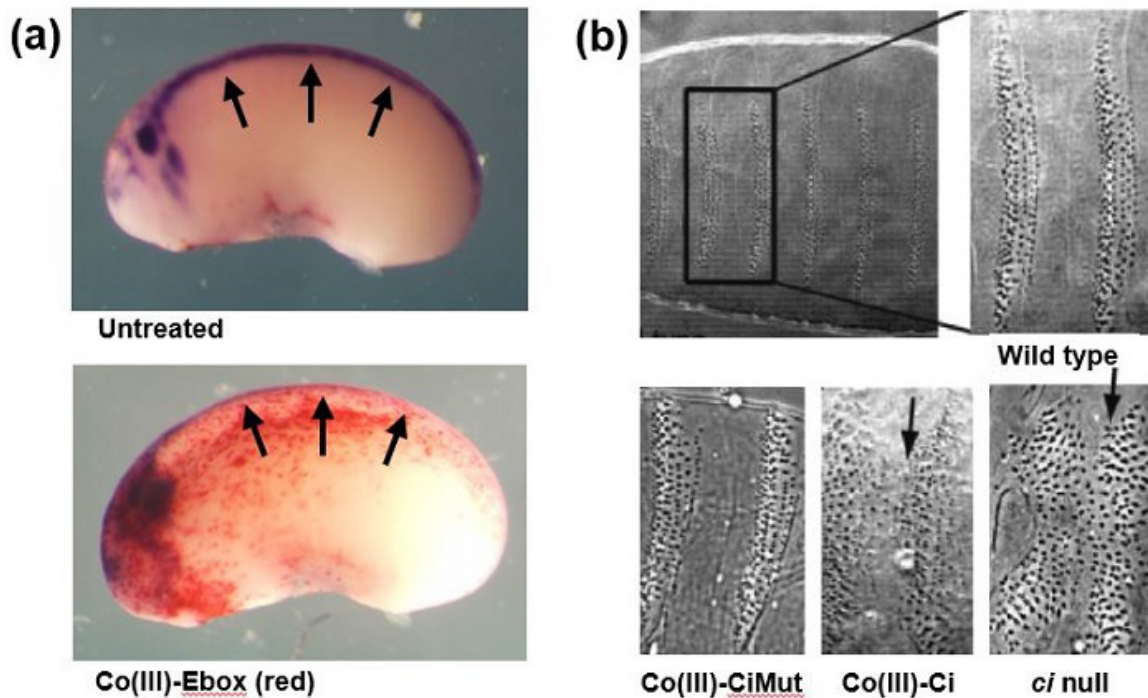


Figure 1.4: (a) *X. laevis* embryos treated with Co(III)-Ebox show dramatically impaired neural crest migration. Red arrows indicate neural crest markers p. Sox and Twist visualized by in situ hybridization. Blue arrows indicate hindbrain control visualized with Krox-20. Co(III)-EboxMut, in which two oligonucleotide base pairs are changed, does not inhibit migration at the same concentrations, indicating specificity of Co(III)-Ebox *in vivo* [101]. (b) Co(III)-Ci inhibits Ci ZFTF function in *D. melanogaster* embryos. Embryos treated with Co(III)-Ci show impaired denticle belt formation relative to the untreated control and Co(III)-CiMut. Co(III)-Ci treatments mimics the phenotype of Ci null embryos, indicating that the conjugate disrupts the associated pathway through inhibiting the Ci ZFTF [115]. Figures reproduced with permission from [101] and [115].

In 2014, the Meade group introduced the first use of a cobalt(III) Schiff base complex as an amyloid inhibitor (**Figure 1.5**) [89]. Like the previously described platinum coordination complexes, Co(III)-sb complexes irreversibly bind His residues via ligand exchange [80]. Early work on the project demonstrated that Co(III)-sb effectively coordinates the His residues of A β ₁₋₁₆, the N-terminal fragment of A β often used in structural studies due to its solubility. Adducts between Co(III)-sb and A β were observed by mass spectrometry and ¹H NMR showed loss of free His protons with increasing equivalents of Co(III)-sb indicating His coordination [89].

In order to assess the effects of Co(III)-sb on aggregation, we measured A β aggregation using SDS-PAGE. Gels were evaluated by silver stain and Western blot analysis using NU-2, an antibody specific for soluble A β oligomers. The data demonstrated that Co(III)-sb binding does alter oligomerization by increasing the formation of large SDS-stable (>30 kDa) oligomeric species and concomitantly decreasing the concentration of small oligomers in a concentration-dependent manner [89]. In order to determine what effect the Co(III)-sb mediated alterations in aggregation might have on cellular A β toxicity, primary hippocampal neurons were treated with oligomers prepared with and without Co(III)-sb and synaptic binding was assessed. Treatment with 100 nM Co(III)-sb decreased synaptic binding to neurons, illustrating the potential for Co(III)-sb to inhibit A β synaptic toxicity (**Figure 1.5**) [89].

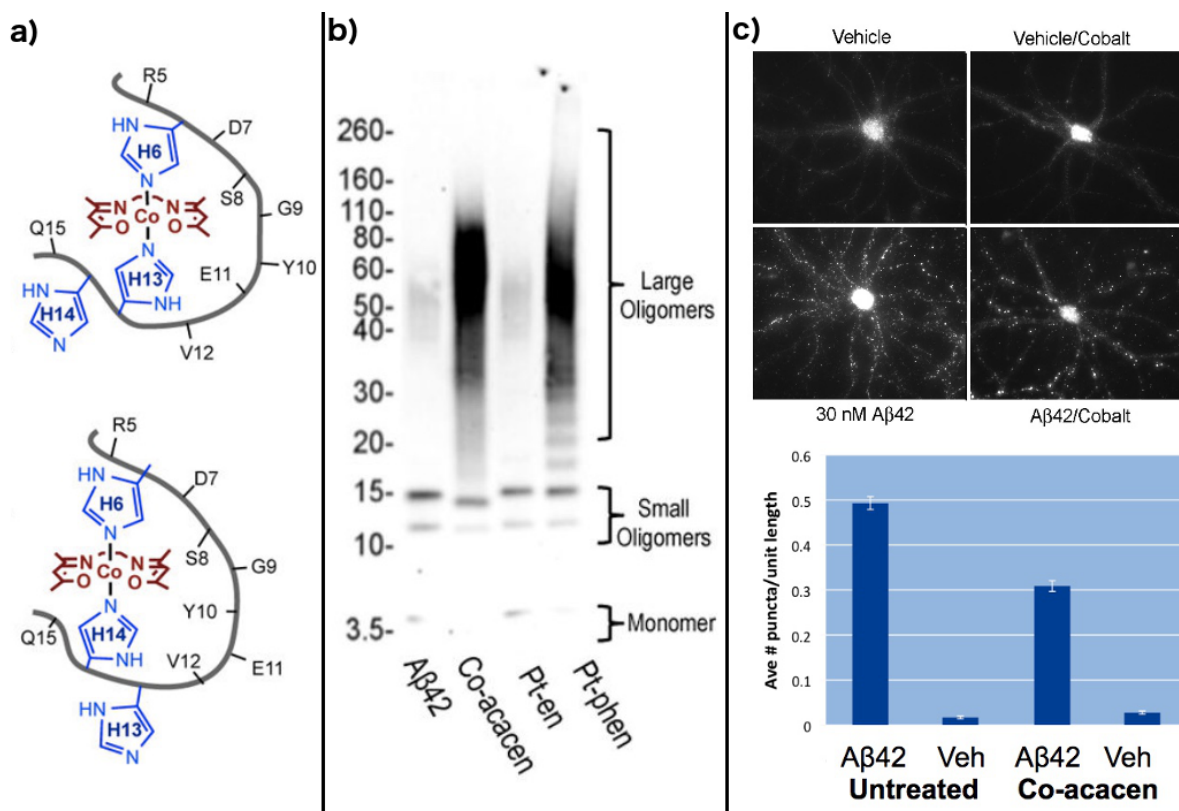


Figure 1.5: Co(III)-sb coordinates to the N-terminal histidine residues of amyloid- β . Bidentate binding to His 6 and His 13/14 was found to be the most energetically favorable binding conformation using DFT calculations (left panel). Treatment of A β ₄₂ with Co(III)-sb during aggregation results in the stabilization of large molecular weight oligomers (>30 kDa) by Western blot with the oligomer specific antibody NU-2 (middle panel). A decrease in small oligomers, which are regarded as the more toxic variant, is also observed upon treatment with Co(III)-sb. This stabilization of large molecular weight oligomers is also observed for the Pt(II) phenanthroline complex developed by the Barnham et al, indicating that the two coordination complexes are likely mechanistically similar [78]. In addition to altering aggregate size, treatment with 100 nM Co(III)-sb also decreases synaptic binding of A β oligomers in primary neuronal culture (right panel). Figure adapted and reproduced with permission from [105].

1.3 Scope of This Work

Taken together, the previous data using Co(III)-sb to inhibit A β aggregation demonstrated great promise for Co(III)-sb in this new application. However, significant work remained. For example, while the effects of Co(III)-sb on oligomeric aggregation were examined using SDS-PAGE, the effects on full *in vitro* aggregation kinetics were not explored. SDS-PAGE is limited to a single time point in the aggregation. In contrast, full aggregation kinetics can be mathematically fit using equation systems describing the underlying physical processes, thereby extracting mechanistic information about aggregation inhibition by Co(III)-sb. Additionally, given the susceptibility of A β aggregation assays to experimental conditions, it was critical to measure aggregation using a variety of complementary assays. This work demonstrates agreement between various modalities for measuring protein aggregation and morphology, each best suited to various phases of aggregation. Remarkable agreement between diverse modalities (including a collaborative computational modeling approach) verifies the described effects. In addition, this work further explores competitive displacement of endogenous metal ions from A β by Co(III)-sb, and how treatment with Co(III)-sb affects ROS generation, cellular dysfunction, and neurotoxicity.

1.4 Publication Information

Sections of this chapter will be published with the following citation information:

E.A. Bajema, **K.F. Roberts**, and T.J. Meade. Cobalt-Schiff Base Complexes: Preclinical Research and Potential Therapeutic Uses. Metal Ions in Life Sciences, Volume 19, Edited by Astrid Sigel, Eva Freisinger, and Roland K. O. Sigel. © Walter de Gruyter GmbH, Berlin, Germany 2019, www.mils-WdG.com

CHAPTER 2

Inhibition of Amyloid- β Aggregation with Cobalt(III) Schiff Base Complexes**2.1 Abstract**

The aggregation of A β underlies the pathogenesis of AD. *In vitro* aggregation kinetics have been shown to correlate to rates of disease progression in AD patients and animal models and represent a useful metric for testing A β -targeted therapeutics. Here we demonstrate evidence of Co(III)-sb inhibition of A β aggregation by a variety of complementary techniques including Thioflavin T (ThT) fluorescence, circular dichroism (CD) spectroscopy, transmission electron microscopy (TEM), and atomic force microscopy (AFM). In addition, we fit our kinetic data using the software AmyloFit to extract mechanistic information about how Co(III)-sb binding alters A β aggregation. This chapter also includes discussion about the role of protein source, A β isoform ratio, and an exploration of negative controls for aggregation studies.

2.2 Introduction

A β is produced extracellularly following the sequential cleavage of the transmembrane protein APP by β - and γ -secretase. The two primary isoforms *in vivo* are A β_{40} and A β_{42} , which are present in an approximately 9:1 ratio in CSF [11]. A β levels are highly variable between individuals and reported absolute numbers vary widely in the literature. For reference, one recent study reported CSF levels of A β_{40} and A β_{42} in 367 people with and without AD that were measured using a commercial ELISA test. A β_{40} was found to be 15,426.6 pg/ml (SD 8,630.6 pg/ml) or approximately 3.6 (\pm 2.0) nM. A β_{42} was found to be 863.6 pg/ml (SD 357.3 pg/ml) or approximately 191.3 (\pm 79.2) pM [116].

Initially monomeric and unstructured, A β pathologically undergoes amyloid aggregation in AD. It is unclear what triggers the aggregation of the soluble innocuous metabolite A β , but evidence implicates oversaturation caused by either overproduction or under-clearance of the peptide from the brain interstitial fluid (ISF) [117]. For example, people with Down's Syndrome or Trisomy 21 inherit three copies of APP and thus have higher production of A β , developing AD at a young age [118]. Similarly, many of the mutations known to cause autosomal dominant early onset AD result in either an increase in A β or an increase in the ratio of A β_{42} :A β_{40} [119]. Disruptions in clearance of A β have been implicated in the sporadic form of AD, with AD patients exhibiting a 30% impairment in clearance of A β compared to normal controls [117]. Further work in animal models has suggested that the mechanism for this impairment may be due to age-related disruptions in CSF flow during sleep leading to reduced glymphatic clearing of toxic brain metabolites like A β [120]. These disruptions in A β metabolism lead to aggregation of the peptide slowly over time, with amyloid pathology often predating cognitive decline by up to a decade [121].

Amyloid aggregation follows a nucleation-dependent polymerization reaction wherein monomers associate into small oligomers which then act as nuclei for further polymerization. The formation of nuclei is slow and termed the lag phase of aggregation. Once a critical nucleus is formed the proteins rapidly aggregate into larger order aggregates and eventually fibrils rapidly during the polymerization phase. Eventually equilibrium is reached between the various aggregate species. In addition to this primary nucleation process, various secondary nucleation mechanisms have been identified and mathematically described [122]. Significant work by the Knowles group has resulted in a system of master equations which model kinetic aggregation data and relate the curves to underlying microscopic processes (**Figure 2.1**) [122-125].

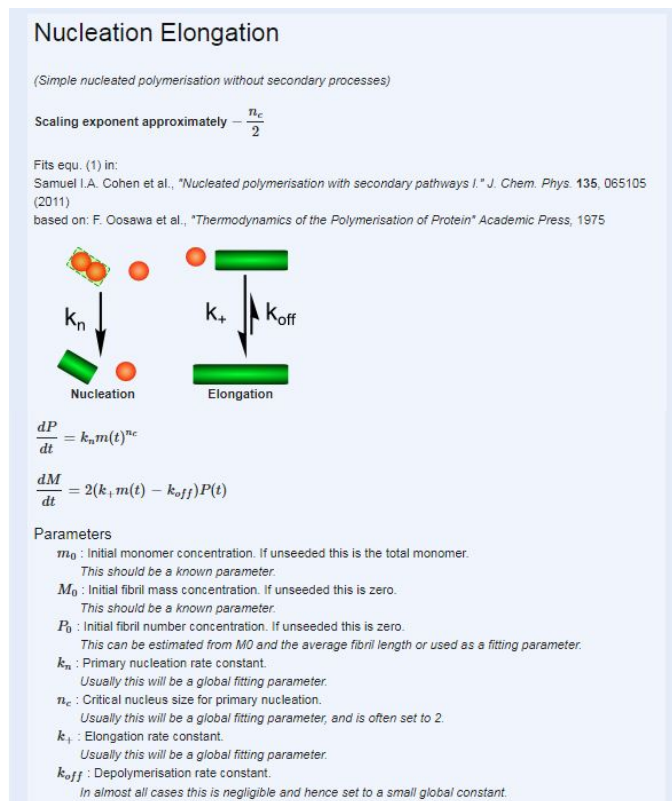


Figure 2.1: A β aggregation can be mathematically described using a nucleation elongation model.

This is the simplest model for describing aggregation and is a system of two differential equations: one describing the formation of primary nuclei and one describing fibril polymerization as a function of primary nuclei over time. Figure from AmyloFit software interface.

As A β aggregates it adopts a β -sheet conformation, which can be followed to measure aggregation kinetics. Many techniques for measuring A β aggregation kinetics utilize this transition to β -sheet secondary structure for quantification. The most widely used of these techniques is Thioflavin T (ThT) fluorescence. ThT is a benzothiazole dye for amyloid assessment *in vitro* and *in vivo* that shifts and increases its fluorescence upon binding to cross- β sheet

structures within amyloid fibrils [126]. When in solution ThT undergoes free rotation around the C-C single bond connecting the benzylamine and benzathiole ring systems. This rotation rapidly quenches excited states leading to minimal fluorescence.

Amyloid aggregates display a cross- β sheet architecture with side chains of amino acids forming a cross strand ladder arrangement parallel to the long axis of the fibrils. Significant evidence has demonstrated that ThT binds to the surface of the cross- β sheets, parallel to the long axis of the fibrils, in grooves formed by the cross strand ladder arrangement of the side chains. This binding locks the ThT molecule into a single conformation, thus preserving the excited states and leading to enhanced fluorescence. Upon binding to amyloid fibrils, ThT undergoes a dramatic shift in its excitation maximum from 385 to 450 nm. Additionally, its fluorescence intensity increases by several orders of magnitude making it a very sensitive reporter [127].

Another widely used technique for measuring A β aggregation kinetics is circular dichroism (CD) spectroscopy, which uses differential absorption of circularly polarized light in the far UV region (190 to 250 nm) to distinguish changes in protein secondary structure over time. Like ThT fluorescence, this technique capitalizes on the shift from initial random coil structure to β -sheet structure in the aggregates. Each type of secondary structure has a characteristic waveform of CD absorption (**Figure 2.2**). The transition from random coil to β -sheet is often followed by the decrease in molar ellipticity at 218 nm, since this is the wavelength where the two curves differ the most. CD has the advantage of not using an exogenous agent (which might alter the aggregation environment) for measurement, however it does require a higher concentration of protein for measurement (on the order of 1 mg protein per read).

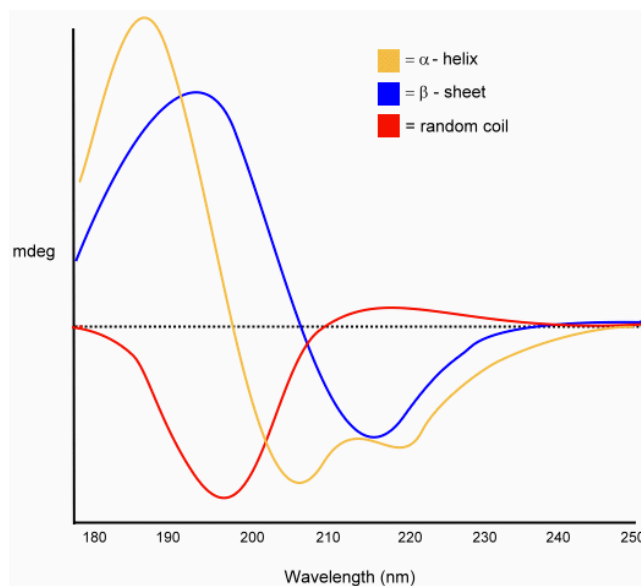


Figure 2.2: CD spectra of ‘pure’ secondary structures of proteins. Monomeric A β is initially unstructured and has a CD spectra similar to random coil (red). As the peptide aggregates, it adopts increasing β -sheet content, which is observed as a transition in the CD spectra over time to a waveform similar to a β -sheet (blue). This transition is often followed by the decrease in molar ellipticity at 218 nm, since this is the wavelength where the two curves differ the most. Figure available online at proteinchemist.com.

In addition to monitoring changes in aggregation kinetics following treatment with Co(III)-sb, we also sought to investigate changes in aggregate morphology. Transmission electron microscopy (TEM) allows direct visualization of amyloid fibrils and large aggregates. Another advantage of TEM is that small sample volumes are required. However, TEM is much better for the visualization of higher order aggregates than small oligomers, making it blind to changes in early aggregate species. In addition, proteins themselves do not have enough electron density to provide adequate contrast for imaging by TEM. As such, TEM imaging of amyloids requires

negative staining with heavy metals such as uranyl acetate, which can introduce additional artifacts. Atomic force microscopy (AFM) is a compatible technique that is also useful for characterizing aggregate morphology, but in contrast to TEM, is better suited for smaller oligomeric aggregate species and does not require any outside agent for staining [28].

While the utility of *in vitro* amyloid aggregation has been broadly demonstrated, assays measuring protein aggregation are subject to a host of confounding variables. For example, aggregation is highly dependent on protein concentration, with higher concentration leading to increased aggregation. Because most assays for measuring aggregation require protein concentration much higher (mid μM) than the endogenous CSF levels of $\text{A}\beta$ (low nM), the aggregation processes measured *in vitro* might not well recapitulate the *in vivo* aggregation conditions [116]. In addition to peptide concentration, environmental factors such as pH, ionic strength, temperature, agitation conditions, and molecular crowding have all been demonstrated to alter aggregation [27, 28]. With so many potential confounding variables, it is not unexpected that there is staggering variability in published aggregation data.

In addition to the wide variability in published aggregation kinetics, there also exists wide variability in the different aggregate species produced [17, 128]. This is amplified by the vague language used to describe various aggregates. Because the aggregation mixtures are highly heterogeneous and transient, it is difficult to compare *in vitro* and *in vivo* aggregate populations, and nearly impossible to isolate individual morphological species. For example, the umbrella term oligomer is used to refer to a wide range of species from dimers to 24mers. This can be further divided into low and high molecular weight oligomers with a cut off around the 8mer stage, but not standardized in the literature. Additional classification can be made utilizing oligomer shape with subclassifications including globular oligomers, annular oligomers, and amylospheroids.

While these distinctions are often encountered in the literature, the precise definitions of these different populations remain unclear and their biological relevance is questionable [129].

Although studies measuring *in vitro* amyloid aggregation have significant limitations, it is generally accepted that to overcome the limitations of individual assays, it is best to confirm results using a variety of complementary assays. For example, selecting assays that are best suited for a variety of phases of aggregation allows insight into each step. Additionally, comparing results from assays with and without known confounders can help identify any outside influence on the aggregation kinetics. The best way to confirm effects on A β aggregation is to consistently demonstrate the effects across a wide range of modalities.

2.3 Materials and Methods

2.3.1 Thioflavin T Fluorescence

Aggresure A β_{40} and A β_{42} were purchased from Anaspec. This peptide was pretreated to ensure monomerization and came with a sample aggregation curve for estimation of aggregation kinetics. Peptide was resuspended, sonicated for 30 seconds in a bath sonicator, and diluted in 20 mM HEPES, 100 mM NaCl to a final concentration of 50 μ M A β_{42} . A fresh solution of ThT was prepared for each assay and syringe filtered before use. ThT was added to the peptide mixture at a final concentration of 200 μ M. Co(III)-sb and unmetallated acacen ligand (negative control) were synthesized and purified according to literature protocols and were added to the samples at concentrations ranging from 5 to 25 μ M (0.1, 0.3, and 0.5 equivalents) [104]. Negative controls consisting of ThT and Co(III)-sb were run to ensure that Co(III)-sb does not alter ThT fluorescence. Samples were plated in quadruplicate on 384 well black, clear flat bottom polystyrene non-binding surface plates (Corning 3544). All peptide manipulation was performed

as quickly as possible to ensure that early time points during the lag phase were not missed since aggregation proceeded very quickly. Typical preparations from resuspension to plating took 10 minutes.

Plates were sealed with aluminum plate seals to prevent sample evaporation. All peptide manipulation was performed using non-binding tips to avoid protein loss. Fluorescence was measured through the plate bottom every 5 minutes for 2 hours at excitation 440 nm and emission 484 nm on a Synergy H1M plate reader. Samples were kept at 37 °C under orbital agitation (252 rpm) in the plate reader between reads. Kinetic data from two separate plates was pooled and plotted using Graphpad Prism. Error bars represent standard error of the mean (SEM). Area under the curve was calculated for each replicate and data is presented as mean \pm SEM.

2.3.2 Circular Dichroism Spectroscopy

For circular dichroism studies synthetic lyophilized A β ₄₀ and A β ₄₂ were purchased from Genscript. This peptide was not guaranteed monomeric, so underwent a monomerization protocol before use. The lyophilized peptide was resuspended in 1,1,1,3,3,3 hexafluoroisopropanol for monomerization. Peptide mixtures of A β ₄₀ and A β ₄₂ were made by combining the appropriate amounts of each monomeric isoform in HFIP so that all aliquots contained 0.1 mg/tube. In order to test the effect of peptide isoform, four types of aliquots were produced: 100% A β ₄₀, 90% A β ₄₀ 10% A β ₄₂, 50% A β ₄₀ 50% A β ₄₂, and 100% A β ₄₂. The monomeric peptide was aliquoted into non-binding surface Eppendorf tubes at 0.1 mg/tube and allowed to dry under nitrogen for 24 hours, followed by 2 hours under vacuum to ensure removal of residual solvent. Following formation of dry peptide films, the aliquots were stored in a -80 °C freezer until use. All solutions

used for experiments were syringe filtered through a 0.2 μm filter to remove particulates that could trigger aggregation.

For resuspension, dried peptide films were brought to room temperature and 50 μL of 20 mM NaOH was added to 0.1 mg of the peptide film. This solution was then probe sonicated for 6 x 1 second pulses at 20% amplitude. Following sonication the peptide was diluted into PBS containing 200 μM EDTA for chelation of residual metal ions and 0.02% sodium azide to inhibit bacterial growth. Aggregation was measured using peptide at a final concentration of 68 μM with Co(III)-sb at 0.5 eq with respect to protein (34 μM). All peptide manipulation was performed using non-binding tips to avoid protein loss.

Samples were read in a 1 mm quartz cuvette on a Jasco J-815 CD spectrometer. Reads were accumulations of 3 scans between 200 nm and 400 nm. Data pitch was set to 1.0 nm, bandwidth was 1 nm, and scan speed was 10 nm/min. Between reads the peptide was kept on an incubator shaker at 37 $^{\circ}\text{C}$ and agitated at 100 rpm. Molar ellipticity at 218 nm was be used to monitor aggregation kinetics over time. Data was analyzed using Jasco SpectraAnalysis software. Processing was completed using CDProAnalysis software. Secondary structure assignments were made using the CONTIN method using the CLSTR library.

2.3.3 Transmission Electron Microscopy

Aggregated A β was characterized morphologically using transmission electron microscopy (TEM). Aggregated solutions were diluted to 10 μM and 10 μl was spotted onto formvar/carbon coated nickel grids (Electron Microscopy Sciences) for 5 minutes. Excess solution was wicked off using filter paper. Grids were washed with deionized water twice for 1 minute before being stained with 10 μl 1% uranyl acetate for 5 minutes. Grids were dried overnight and imaged on a

Hitachi HD-2300 Dual EDS Cryo STEM operated at 120 kV. Structures formed in the presence and absence of Co(III)-sb were qualitatively assessed for differences. Images were processed using ImageJ.

2.3.4 Atomic Force Microscopy

Samples for Atomic Force Microscopy (AFM) were prepared by diluting 10 μ l of the aggregation mixtures in 1 ml of double distilled water. 15 μ l of each sample was then drop cast onto freshly cleaved mica plates (Ted Pella, Highest grade mica) functionalized with (3-aminopropyl)triethoxysilane (APTES). The samples were incubated at ambient temperature for 10 minutes, washed once with 1 ml of double distilled water, then allowed to dry protected from dust for at least 6 hours. APTES functionalized mica plates were produced by adding 10 μ l of a 0.1 (v/v) aqueous solution of APTES to freshly cleaved mica and incubating at ambient temperature for 2 minutes. The plates were rinsed with 3 x 1 ml of double distilled water and allowed to dry, protected from dust, for at least 12 hours.

The samples were imaged using a Bruker Dimension FastScan system equipped with a silicon tip (nominal radius 10 nm). Initial image flattening and preparation of publication quality images were conducted in the NanoScope Analysis software package (v1.9). Equivalent disc radius and maximum bounding dimensions were calculated using Gwyddion analysis software (v. 2.50). The distributions of these values were calculated using an image mask with a minimum z-value of 0.5 nm. Data were plotted in Graphpad Prism and represent mean \pm SEM.

2.3.5 Kinetic Fitting using AmyloFit

Data obtained from ThT aggregation experiments was uploaded to the free online platform AmyloFit for processing and analysis of protein aggregation kinetic data [130]. AmyloFit is a free platform that can be accessed at <http://www.amylofit.ch.cam.ac.uk/login>. Mathematical fitting to protein aggregation models allowed determination of which microscopic processes were dominant and how treatment with Co(III)-sb affected these processes. Experiments were carried out as described above in Section 2.3.1, with the exception that multiple dilutions of final A β monomer concentration were used (40 μ M, 20 μ M, 10 μ M, and 5 μ M). These dilutions were made by serially diluting the starting peptide concentrations down in buffer containing 200 μ M ThT. Co(III)-sb dosing was always maintained at the aforementioned equivalencies compared to peptide concentration. ThT concentration was 200 μ M for all monomer concentrations.

Raw data was reformatted to .txt files containing time and raw fluorescence measurements for each condition. Data was uploaded, normalized to 0% and 100%, and replicates were grouped. Fitting was attempted for untreated, 0.1 eq Co(III)-sb, 0.3 eq Co(III)-sb, and 0.5 eq Co(III)-sb treated conditions. Only untreated A β and A β + 0.1 eq Co(III)-sb were able to be fit by the program. The half time plotter tool was used to confirm the most appropriate model to fit the data. Next, the data was fit to the Nucleation Elongation model. The variables P_0 and M_0 were set to a Global Constant of 0. The variable m_0 was set to a Constant for each data set and was equal to the starting monomer concentration for each aggregation. The parameters k_n , n_c , k_+ , and k_{off} were set to Global Fit with initial guesses of 1, 2, 1×10^8 , and 1×10^{-15} respectively. Basin hops was set to 50 and the data was fit with errors to yield the model parameters described below.

2.3.6 Negative Control Preparation

A variety of negative controls were tested in ThT aggregation assays. Co(III)-sb complexes with stable axial ligands (L= Im, 4MeIm) were used in aggregations as described above in Section 2.3.1. These complexes were synthesized and purified according to literature protocols [104]. CoDiIm is a double Co(III)-sb complex consisting of two 1,10-diimidazolyldecane bridging axial ligands (**Figure 2.17**) [104]. This complex was dosed with equivalency to Co(III) maintained compared to single Co(III)-sb complexes. All Co(III)-sb solutions were prepared, checked for Co concentration using ICP-MS (methods described in detail in **Section 4.3.5**), and aliquoted into single use aliquots which were stored at -80 °C until use. Solutions did not undergo repeat freeze thaws.

2.4 Results

2.4.1 Co(III)-sb Alters Aggregation Kinetics by ThT Fluorescence

ThT fluorescence remains the most widely used method for measuring *in vitro* amyloid aggregation kinetics. To explore the effects of treatment with Co(III)-sb, monomeric A β was treated with 0.1, 0.3, and 0.5 equivalents of Co(III)-sb. Because each monomer of A β has three N-terminal His residues, the highest number of bound Co(III)-sb possible would be 3 equivalents assuming one to one binding with each His residue. As such, all doses used in these aggregation studies were substoichiometric for Co(III)-sb compared to A β . Co(III)-sb treated A β was compared to untreated control aggregation, as well as A β treated with the highest dose (0.5 equivalents) of the unmetallated ligand acacen.

Treatment with Co(III)-sb showed dose-dependent reduction in the aggregation by ThT fluorescence (**Figure 2.3**). For A β_{42} , this was reflected in a decrease in the equilibrium plateau

height, as well as a decrease in the slope of the curve during the polymerization phase, which manifests as an increase in the half time of aggregation (time to reach half max fluorescence). Explicit effects on the lag phase (initial period of baseline signal) were obscured by the rapid kinetics of aggregation. Based on the sample aggregation curve sent with the protein samples, the lag phase of aggregation was between 5 and 10 minutes. Due to sample prep, the first read was not until 10 minutes after resuspension, by which time the conditions had already entered into the polymerization phase of aggregation.

Area under the curve analysis combines the effects on lag time and equilibrium height into a single metric (**Figure 2.4**). This demonstrates that 0.1, 0.3, and 0.5 equivalents Co(III)-sb decreases the area under the aggregation curve by 25%, 60%, and 68% respectively compared to untreated control. In contrast, treatment with 0.5 equivalents of the unmetallated ligand does not significantly alter the area under the aggregation curve.

$\text{A}\beta_{42}$ Aggregation Kinetics by ThT Fluorescence

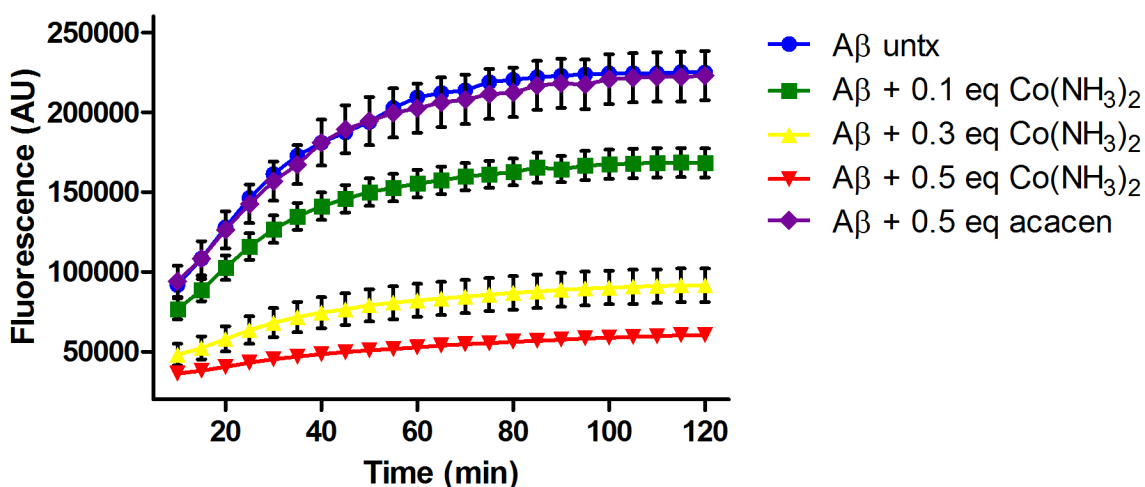


Figure 2.3: Inhibition of $A\beta_{42}$ aggregation by Co(III)-sb by ThT fluorescence. Untreated $A\beta_{42}$ is in blue, $A\beta_{42} + 0.1$ eq Co(III)-sb is in green, $A\beta_{42} + 0.3$ eq Co(III)-sb is in yellow, $A\beta_{42} + 0.5$ eq Co(III)-sb is in red, and $A\beta_{42} + 0.5$ eq acacen is in purple. Data are presented as mean \pm SEM. Co(III)-sb demonstrates dose-dependent inhibition, while acacen (negative control) does not alter aggregation.

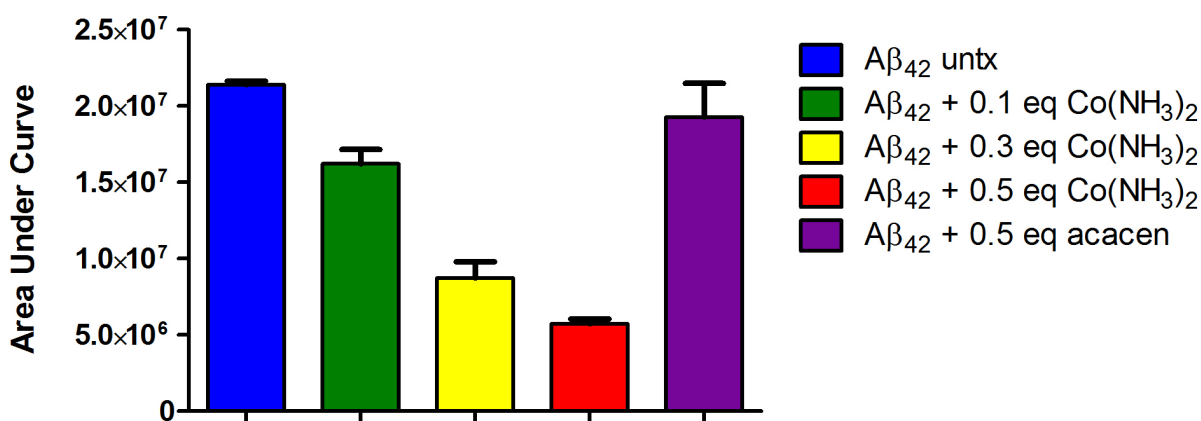


Figure 2.4: AUC analysis of $A\beta_{42}$ aggregation by ThT fluorescence. Untreated $A\beta_{42}$ is in blue, $A\beta_{42} + 0.1$ eq Co(III)-sb is in green, $A\beta_{42} + 0.3$ eq Co(III)-sb is in yellow, $A\beta_{42} + 0.5$ eq Co(III)-sb is in red, and $A\beta_{42} + 0.5$ eq acacen is in purple. Data are presented as mean \pm SEM. Co(III)-sb demonstrates dose-dependent inhibition, while acacen (negative control) does not alter aggregation.

Repeating the same aggregation studies using $A\beta_{40}$ instead of $A\beta_{42}$ demonstrates similar results (**Figure 2.5**). Co(III)-sb exhibits dose-dependent inhibition of aggregation with a reduction in both equilibrium height and polymerization rate. Additionally, 0.5 equivalents of Co(III)-sb is enough to completely inhibit aggregation of the peptide. With $A\beta_{40}$, the aggregation kinetics are

slower than previously described for $A\beta_{42}$, but are still one of the faster ends of kinetics reported in the literature. In addition, the negative control (0.5 equivalents acacen) appears to have a small inhibitory effect on the $A\beta_{40}$ aggregation, which was not the case for $A\beta_{42}$.

$A\beta_{40}$ Aggregation Kinetics by ThT Fluorescence

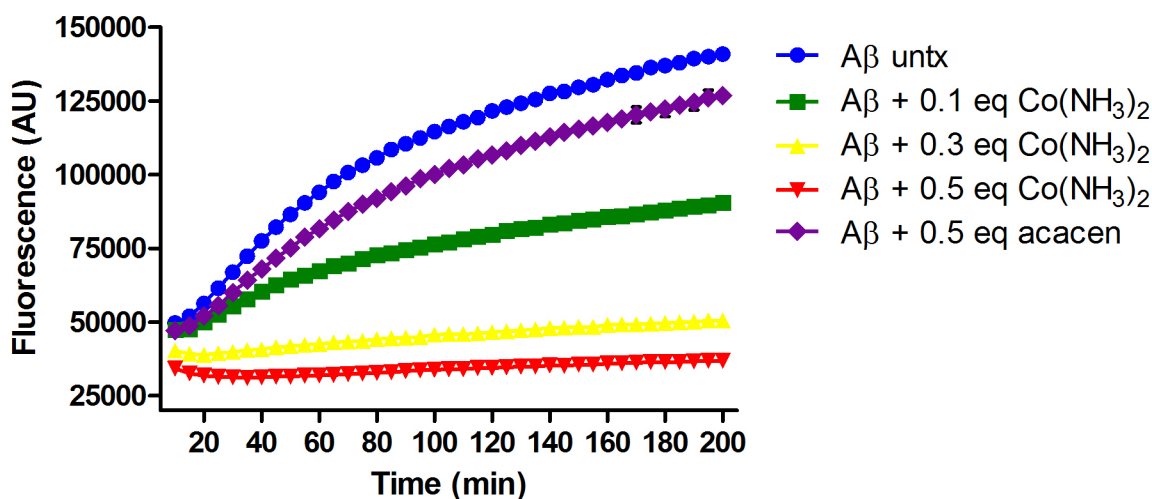


Figure 2.5: Inhibition of $A\beta_{40}$ aggregation by Co(III)-sb by ThT fluorescence. Untreated $A\beta_{40}$ is in blue, $A\beta_{40}$ + 0.1 eq Co(III)-sb is in green, $A\beta_{40}$ + 0.3 eq Co(III)-sb is in yellow, $A\beta_{40}$ + 0.5 eq Co(III)-sb is in red, and $A\beta_{40}$ + 0.5 eq acacen is in purple. Data are presented as mean \pm SEM. Co(III)-sb demonstrates dose-dependent inhibition, while acacen (negative control) does not alter aggregation.

AUC analysis for $A\beta_{40}$ is very similar to that for $A\beta_{42}$, with 0.1, 0.3, and 0.5 equivalents of Co(III)-sb inhibiting the aggregation by 31%, 57%, and 67% respectively (**Figure 2.6**). Treatment with 0.5 equivalents of acacen decreased aggregation by only 12%, indicating that although the

negative control demonstrated some inhibition, it was to a much smaller degree than even one fifth the dose of the metallated active compound.

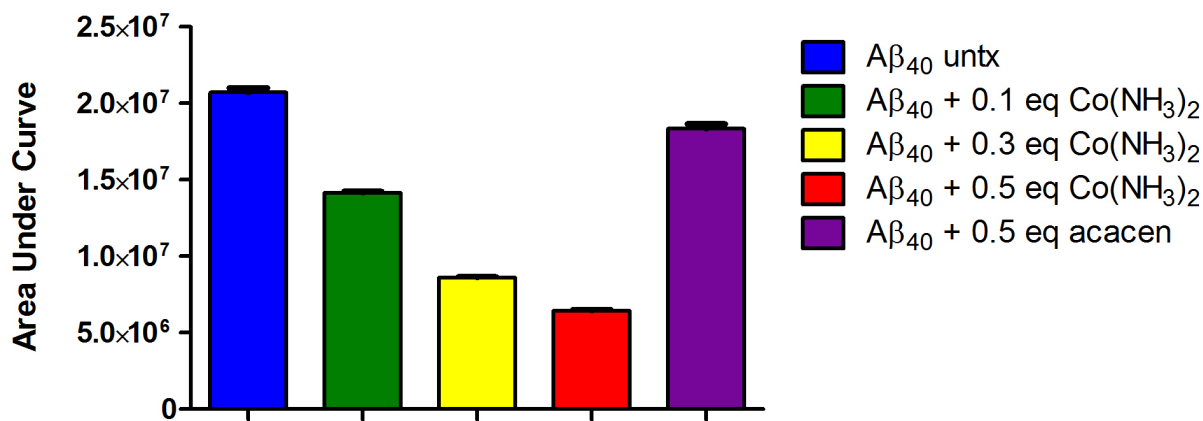


Figure 2.6: AUC analysis of Aβ₄₀ aggregation by ThT fluorescence. Untreated Aβ₄₀ is in blue, Aβ₄₀ + 0.1 eq Co(III)-sb is in green, Aβ₄₀ + 0.3 eq Co(III)-sb is in yellow, Aβ₄₀ + 0.5 eq Co(III)-sb is in red, and Aβ₄₀ + 0.5 eq acacen is in purple. Data are presented as mean ± SEM. Co(III)-sb demonstrates dose-dependent inhibition, while acacen (negative control) does not alter aggregation.

2.4.2 Co(III)-sb Mechanistic Insight from Kinetic Fitting

After significant optimization effort, a robust protocol for measuring Aβ aggregation by ThT fluorescence was produced that yielded high-quality reproducible kinetic curves. A major advantage for measuring full aggregation kinetics (in contrast to aggregation end point assays such as SDS-PAGE, AFM, or TEM) is that mathematical modeling can be used to extract mechanistic details about the mode of inhibition. Traditionally, aggregation curves have been fit using sigmoidal equations suited to mathematically describe the shape of the curve [131]. While useful for comparing the effects of treatments on the shape of the overall curve, these equations were not

rooted in the underlying microscopic processes of aggregation. More recently, the Knowles group at Cambridge has developed a system of equations describing amyloid aggregation that directly physically relates to the underlying protein association phenomena [122]. In addition to publishing this system of equations, the Knowles group has also developed an online tool called AmyloFit (available at <http://www.amylofit.ch.cam.ac.uk/login>), for facile fitting of outside generated aggregation data using their system [130].

In order to fit aggregation data using AmyloFit, aggregation kinetics must be generated at a variety of different initial monomer concentrations. The previously described ThT assay protocol was adapted to serially diluted protein monomer concentrations (40 μM , 20 μM , 10 μM , and 5 μM) while keeping ThT constant. Co(III)-sb dosing was always kept in equivalents compared to monomeric A β . Because the AmyloFit system was designed based on data from A β_{42} , we used only kinetic data from A β_{42} aggregations. Although we attempted to model the results from all three tested doses of Co(III)-sb, 0.3 and 0.5 equivalents inhibited so strongly as to render the curves non-sigmoidal upon normalization. As such, the kinetic fitting failed to accurately model these datasets, and the results presented are limited to the comparison of the untreated A β_{42} to that treated with 0.1 equivalent of Co(III)-sb.

AmyloFit has the capability for modeling a variety of different aggregation mechanisms. The simplest of these is the nucleation elongation model. This model assumes that primary nucleation (ie. association of monomers into oligomeric nuclei) is the dominant method for formation of aggregation nuclei. This is in contrast to other models emphasizing the role of secondary nucleation (wherein larger aggregates can act as nuclei for the formation of new fibrils). The appropriateness of the model is determined by plotting the log of the initial monomer

concentration (m_0) vs the log of the aggregation half time (τ). Prior normalization of the data is critical for this step.[130]

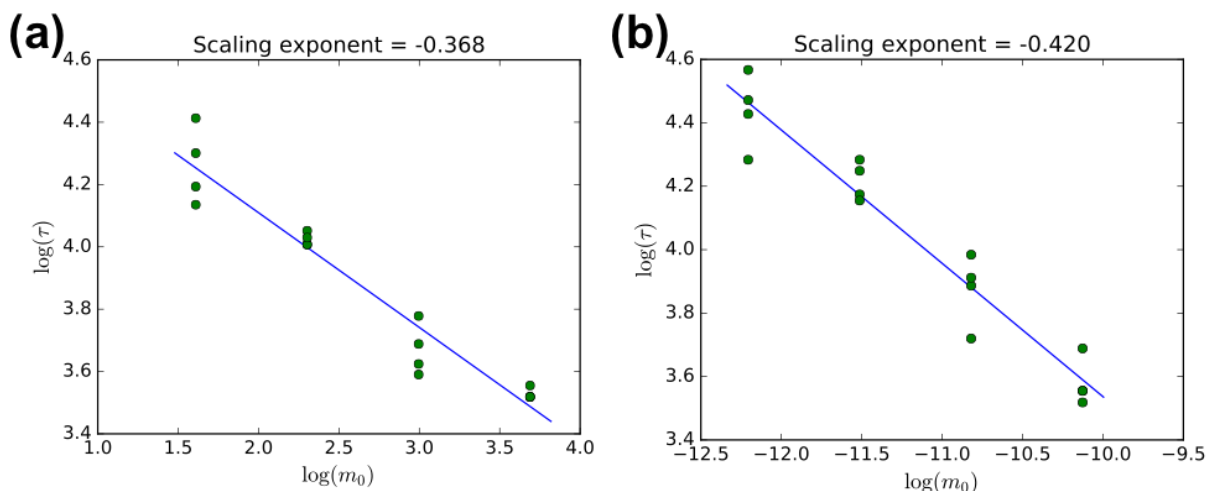


Figure 2.7: Half time log plots for kinetic fitting of (a) untreated $A\beta_{42}$ and (b) $A\beta_{42} + 0.1$ eq Co(III)-sb. The log of the initial monomer concentration is plotted against the log of the aggregation half time. The slope of this line gives the scaling exponent. If this line is linear, nucleation elongation is a suitable model for the kinetic data.

The half time log plots demonstrate a linear relationship between the log of the initial monomer concentration and the log of the half time (**Figure 2.7**). The slope of this graph is termed the scaling exponent and contains information about the dominant mechanism of fibril multiplication. In addition, the shape of the curve offers insight into how the dominant mechanism changes with monomer concentration. A linear graph indicates that the dominant mechanism is the same for all monomer concentrations. As positive curvature in the graph indicates competition between two processes in series or a saturation process. A negative curvature indicates

competition between two processes in parallel (for example both secondary nucleation and fibril fragmentation) [130].

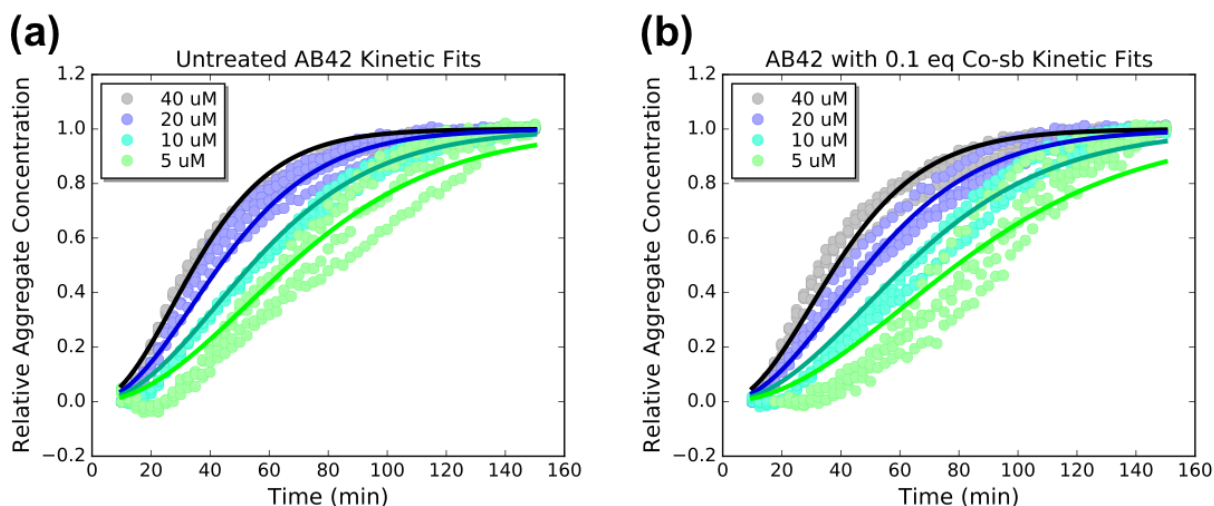


Figure 2.8: AmyloFit normalized aggregation curve data (points) and model fits (lines) for (a) untreated $A\beta_{42}$ and (b) $A\beta_{42} + 0.1$ equivalent $Co(III)\text{-sb}$. Normalization of the data involves identifying the maximum and minimum of the aggregation and presenting the data normalized from 0.0 to 1.0 relative aggregate concentration in order to emphasize changes in the polymerization parameters.

The raw fluorescence data was uploaded to AmyloFit, the y values normalized between 0.0 and 1.0 relative aggregate concentration, and plotted vs time. Replicates were grouped together. Initial parameters were chosen in the software as described in Section 2.3.5. Unknown parameters were set to Global Parameter. Following fitting of the data with error, the parameters listed in **Table 2.2** were identified by the model. The error described by the model is a measure

of how much one can vary the parameters without changing the goodness of the fit. A large error indicates that the parameter is poorly constrained by the data.

The most notable changes between the untreated $A\beta_{42}$ and the $A\beta_{42} + 0.1$ equivalent Co(III)-sb were a 10 order of magnitude increase in the nucleation rate (k_n) and a 9 order of magnitude decrease in the polymerization rate (k_+) with Co(III)-sb treatment. All other parameters were either constants or did not vary significantly between the aggregation fits with and without Co(III)-sb. The variable k_{off} was very small for both data sets indicating that fibrils depolymerization played a very minor role in the aggregation kinetics and this was unchanged by Co(III)-sb.

Table 2.1: Global parameters from AmyloFit kinetic fitting of untreated $A\beta_{42}$ aggregation and $A\beta_{42} + 0.1$ equivalent Co(III)-sb.

Parameter	Untreated $A\beta_{42}$	$A\beta_{42} + 0.1$ eq Co(III)-sb
P_0 (conc)	0.00	0.00
M_0 (conc)	0.00	0.00
k_n (conc ^{-n_c+1} time ⁻¹)	5.72 E -8 (+1.7 E -8 / -1.5 E -9)	230 (+16 / -22)
n_c (unitless)	0.614 (+1.1 E -2 / -4.0 E -3)	0.693 (+2.5 E -4 / -7.8 E -3)
k_+ (conc ⁻¹ time ⁻¹)	5.28 E 6 (+0.0 / -1.7 E 6)	2.45 E -3 (+2.5 E -4 / -1.6 E -4)
k_{off} (time ⁻¹)	6.94 E -15 (+3.1 E -16 / -1.4 E -15)	2.29 E -15 (+0.0 / -9.3 E -16)

2.4.3 Co(III)-sb Aggregation Inhibition by CD Spectroscopy

CD spectroscopy is a complementary technique to ThT fluorescence that also follows aggregation kinetics by measuring β -sheet content in the protein as it aggregates. Aggregation mixtures were prepared as previously described for the ThT assay, but without the addition of

exogenous fluorophore. Higher protein concentration was required for adequate signal, so dosing equivalency was maintained between assays. In order to obtain slow aggregation kinetics, A β ₄₀ was chosen as the isoform for these experiments.

A β ₄₀ was allowed to aggregate in a nonbinding Eppendorf tube and periodically transferred to a quartz 1 mm cuvette for measurement of ellipticity. When compared to the standard CD waveforms for various secondary structures (**Figure 2.2**), it is apparent that untreated A β ₄₀ initially existed in primarily a random coil structure (**Figure 2.9a**), which was maintained throughout the first three timepoints (until hour 41). Between hours 41 and 68, the peptide underwent aggregation, shifting from a random coil waveform to a β -sheet waveform. Subsequent time points showed a stable β -sheet waveform that decreased in amplitude over time. This loss in signal was a result of protein precipitation to the cuvette, as well as loss of soluble protein aggregates.

Like the untreated A β ₄₀ aggregation, the 0.5 equivalent Co(III)-sb treated condition also initially exhibited a random coil waveform at hour 1 (**Figure 2.9b**). However, while the random coil waveform was stable until hour 41 in the untreated, the Co(III)-sb treated A β ₄₀ quickly stabilized into an alternate conformation, not representing a random coil or β -sheet. This change was particularly interesting because it preceded the measured lag phase of aggregation for this A β ₄₀ prep (~50 hours) and thus likely reflected a structural change during the nucleation phase of aggregation, which is difficult to measure using ThT fluorescence.

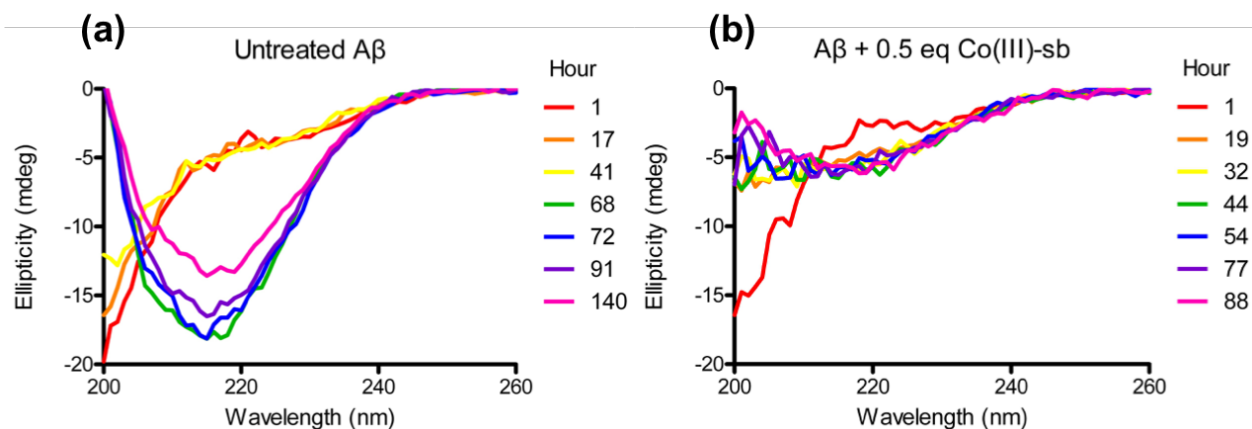


Figure 2.9: (a) Untreated Aβ₄₀ aggregation by CD demonstrates a shift from random coil at early time points (red, orange, yellow) to β-sheet (green) after aggregation. (b) Aβ₄₀ treated with 0.5 equivalents Co(III)-sb is initially random coil, but very early stabilizes into an alternative conformation. Representations of standard CD spectra of pure secondary structures can be found in Figure 2.2.

Because Aβ aggregation represents a transition between two of the basic secondary structure waveforms (random coil to β-sheet), one simplistic way of quantifying this change to generate sigmoidal aggregation kinetics is to follow the ellipticity at 218 nm (the wavelength where the two curves differ the most). Aggregation is measured as a decrease in the signal at 218 nm indicating conversion to primarily β-sheet secondary structure. Like ThT aggregation, this method typically demonstrates a lag phase, a rapid polymerization phase, and an equilibrium plateau. **Figure 2.10** illustrates sample kinetics for the previous data. Here it is obvious that the untreated Aβ₄₀ undergoes a structural transition, while the Co(III)-sb treated Aβ₄₀ does not.

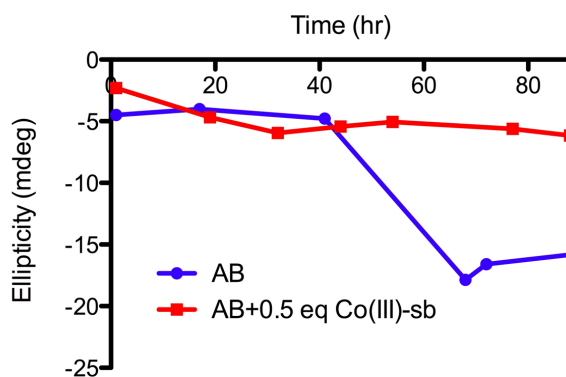


Figure 2.10: Transition from random coil to β -sheet as measured by ellipticity at 218 nm. Untreated $A\beta_{40}$ aggregates at around 50 hrs, while Co(III)-sb treated $A\beta_{40}$ does not.

Another option for interpretation of CD data, is to use libraries of known protein structures to fit the CD waveforms and determine the overall composition of the protein as broken down into percent content of the various common secondary structures. While this method is widely used in structural studies of proteins, it is not popular for amyloids given that the fitting is based on proteins with known structures. Amyloids in general are structurally distinct, lack solved structures, and are not well represented by the available fitting libraries.

The measured CD waveforms were imported into the fitting software and normalized. The CLSTR library was selected as the fitting library and structural content estimations calculated. **Table 2.2** depicts the fitting results for both untreated and Co(III)-sb treated at the initial time point and a later aggregation point. At time 1 hr, both conditions fit primarily to an α -helix with a small amount of β -sheet content. At the later time point, both conditions have increased their β -sheet percentage. Co(III)-sb shows a very minor decrease in β -sheet content, however the magnitude of the change is negligible.

Table 2.2: CD secondary structure percent estimation based on CLSTR library.

	Untx A β		A β + 0.5 eq Co(III)-sb	
	Hr 1	Hr 68	Hr 1	Hr 77
α helix	71.0%	33.2%	81.8%	33.1%
β sheet	13.5%	66.8%	18.2%	64.6%
unordered	0%	0%	0%	0%
other	15.5%	0%	0%	2.3%

Additional CD experiments testing the other isoform ratios were conducted. Similar to ThT kinetics, it was observed that increasing the percentage of A β_{42} decreased the half time of aggregation. In addition, mixtures that had a high proportion of A β_{42} also crashed out of solution at a higher rate. This led to low ellipticity signal, despite keeping protein concentrations constant. The signal for A β_{42} aggregation by CD was so low that the protein concentration required to see adequate signal was considered excessive. The trends described above for A β_{40} were additionally observed for the 9:1 mixture of A $\beta_{40}:_{42}$, but the absolute signal was lower (data not shown).

2.4.4 Co(III)-sb Alters Aggregate Morphology by TEM

Structural changes in aggregate morphology were assessed via TEM. Grids spotted with the A β aggregation mixtures were negatively stained with uranyl acetate and imaged. **Figure 2.11a** demonstrates the formation of standard amyloid fibrils by untreated A β_{40} . These fibrils are approximately 10 nm in diameter and up to μm in length. The fibrils form a dense meshwork and

are negatively stained light on a dark background. In contrast, **Figure 2.11b** demonstrates the aggregates present following treatment with 0.5 equivalents Co(III)-sb. The aggregates are smaller than full fibrils and likely represent protofibrils or high molecular weight oligomers. Although not included in this figure, occasional fibrils were observed.

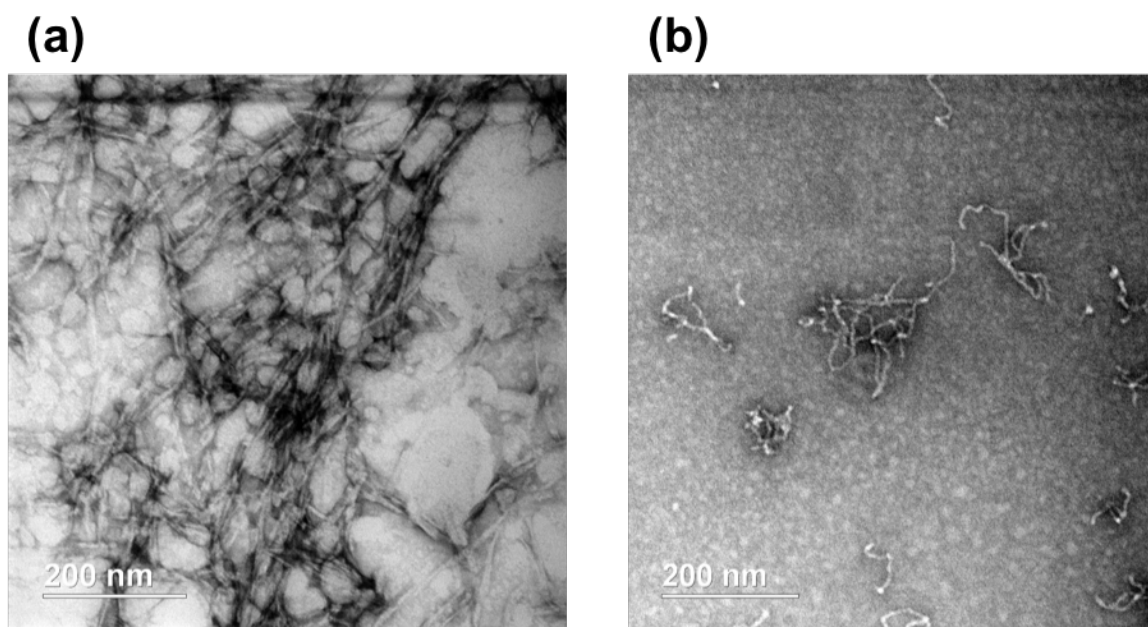


Figure 2.11: TEM images of (a) untreated A β_{40} demonstrating typical amyloid fibrils and (b) A β_{40} treated with 0.5 equivalents Co(III)-sb showing stabilization of smaller aggregate species morphologically consistent with protofibrils or high molecular weight oligomers.

TEM images were also taken of A β_{42} aggregates with and without Co(III)-sb. Again the untreated protein demonstrated formation of typical amyloid fibrils (**Figure 2.12a**) which were shorter in length than those observed for A β_{40} . This variation could be due to changes in grid preparation or agitation conditions of the aggregate mixture (ie. higher agitation can cause more sheering of fibrils). The Co(III)-sb treated peptide showed a lack of fibrils (**Figure 2.12b**). Several

small aggregate clusters were identified, but none of the spiral shaped winding protofibrils seen in the $A\beta_{40}$ aggregations were evident in the $A\beta_{42}$ samples.

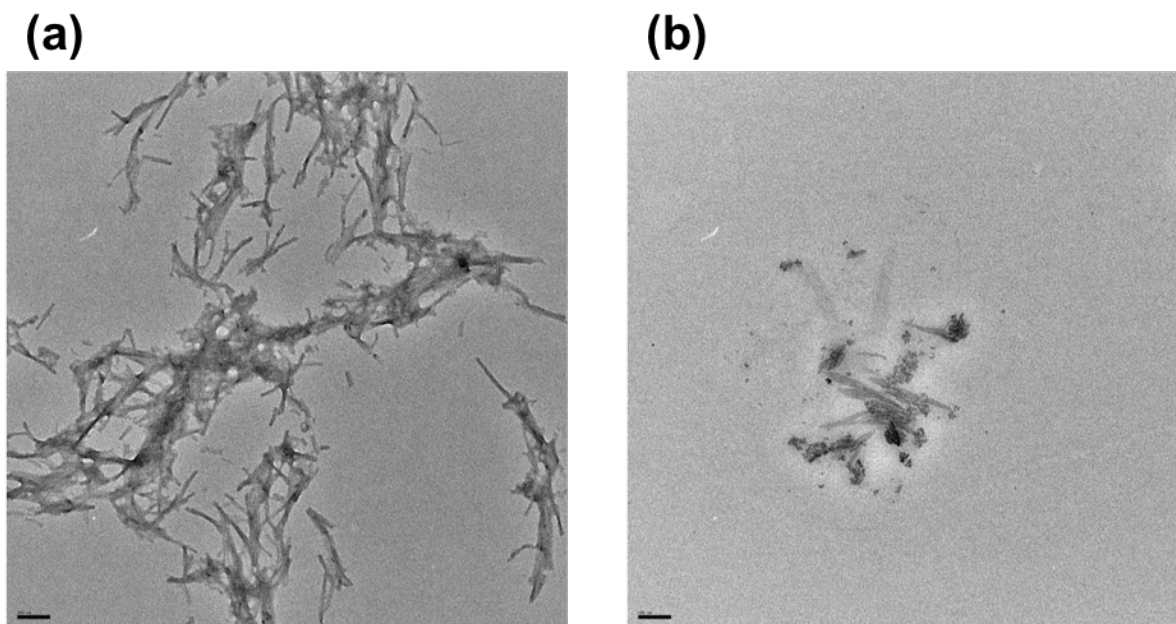


Figure 2.12: TEM images of (a) untreated $A\beta_{42}$ demonstrating typical amyloid fibrils and (b) $A\beta_{42}$ treated with 0.5 equivalents $Co(III)-sb$ showing stabilization of smaller aggregate species.

2.4.5 $Co(III)-sb$ Alters Size Distribution by AFM

AFM is an additional technique for morphological characterization of amyloid aggregates. It has higher resolution than TEM and is thus better suited to capturing effects on smaller aggregates and oligomers. Equilibrium aggregation mixtures were diluted, spotted onto mica grids, and imaged. Comparison of particle sizes between untreated $A\beta_{42}$ (**Figure 2.13a**), $A\beta_{42} + 0.5$ equivalents $Co(III)-sb$ (**Figure 2.13b**), and $A\beta_{42} + 0.5$ equivalents acacen (**Figure 2.13c**) show that $Co(III)-sb$ reduces the aggregate size, while acacen is not different from untreated.

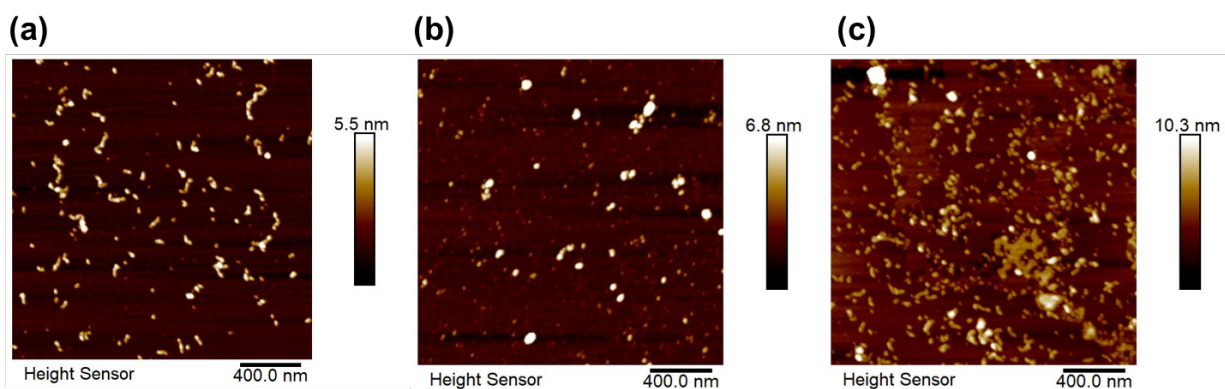


Figure 2.13: AFM images of equilibrium aggregate distributions for (a) untreated Aβ₄₂, (b) Aβ₄₂ + 0.5 equivalents Co(III)-sb, and (c) Aβ₄₂ + 0.5 equivalents acacen.

Quantitation of these particle size distributions is demonstrated in **Figure 2.14**. The variable $r\text{-eq}$ represents the radius of a circle with the same average area as the particles, while the variable D_{max} gives the average length of the largest dimension of the aggregates. In both area and length metrics, treatment with Co(III)-sb reduces the size of the aggregates, while treatment with the negative control acacen does not change the size.

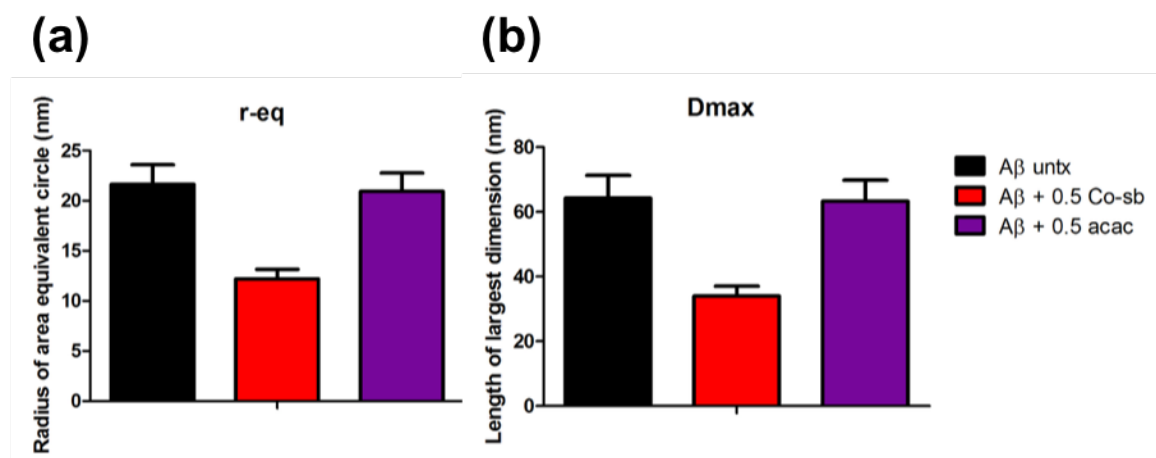


Figure 2.14: Quantitation of AFM size distributions. (a) Treatment of A β ₄₂ with Co(III)-sb decreases r-eq (the radius of the circle with equivalent area to aggregate size), while acacen does not differ from untreated A β ₄₂. (b) Treatment of A β ₄₂ with Co(III)-sb decreases Dmax (the largest dimension of aggregate size), while acacen does not differ from untreated A β ₄₂.

2.4.6 Comparison of Negative Controls

Early optimization work for development of the ThT assay for measuring aggregation kinetics used the protein source and preparation method detailed in Section 2.3.2. For these experiments we purchased Genscript A β , which is delivered as the 26-O-acyl isoA β click peptide precursor. As such, it must be resuspended at pH > 7.4 to undergo O-to-N acyl migration and generate the native peptide. This reaction proceeds efficiently and without byproducts by resuspending the peptide in 20 mM NaOH. Additionally, because this peptide was not guaranteed monomeric, it required a separate monomerization protocol before use. This allowed for the preparation of frozen peptide films with various ratios of A β ₄₀ and A β ₄₂. Four combinations of peptide were produced: 100% A β ₄₀, 90% A β ₄₀ + 10% A β ₄₂ (9:1 A β ₄₀:A β ₄₂), 50% A β ₄₀ + 50% A β ₄₂ (5:5 A β ₄₀:A β ₄₂), and 100% A β ₄₂.

For these assays, the protein was prepped as described above for the ThT assay with the following changes: ThT concentration was 25 μ M, A β peptide concentration was 25 μ M, aggregation buffer was PBS containing 200 μ M EDTA for chelation of residual metal ions and 0.02% sodium azide for inhibition of microbial growth, peptide was initially resuspended in 25 mM NaOH and probe sonicated 6 x 1 second pulses at 20% amplitude for resuspension and conversion to native A β , and reads were taken every 6 hours on a Biotek Synergy 4 multimode

plate reader with covered plates being stored in an incubator shaker at 37 °C and shaken in orbital mode at 100 rpm between reads.

Comparison of the four $A\beta_{40}:A\beta_{42}$ ratios shows that increasing the fraction of $A\beta_{40}$ in the peptide mixture increases the lag time of aggregation. Pure $A\beta_{42}$ aggregated fastest with a lag time on the order of several hours, next 5:5 $A\beta_{40}:A\beta_{42}$ aggregated with a half time around 20 hrs, followed by 9:1 $A\beta_{40}:A\beta_{42}$ at 50 hrs, and pure $A\beta_{40}$ after 150 hrs (**Figure 2.14**, black curves). For each peptide ratio, Co(III)-sb showed dose dependent inhibition of aggregation with 0.5 equivalents of Co(III)-sb completely inhibiting aggregation in all peptide ratios studied (**Figure 2.15**).

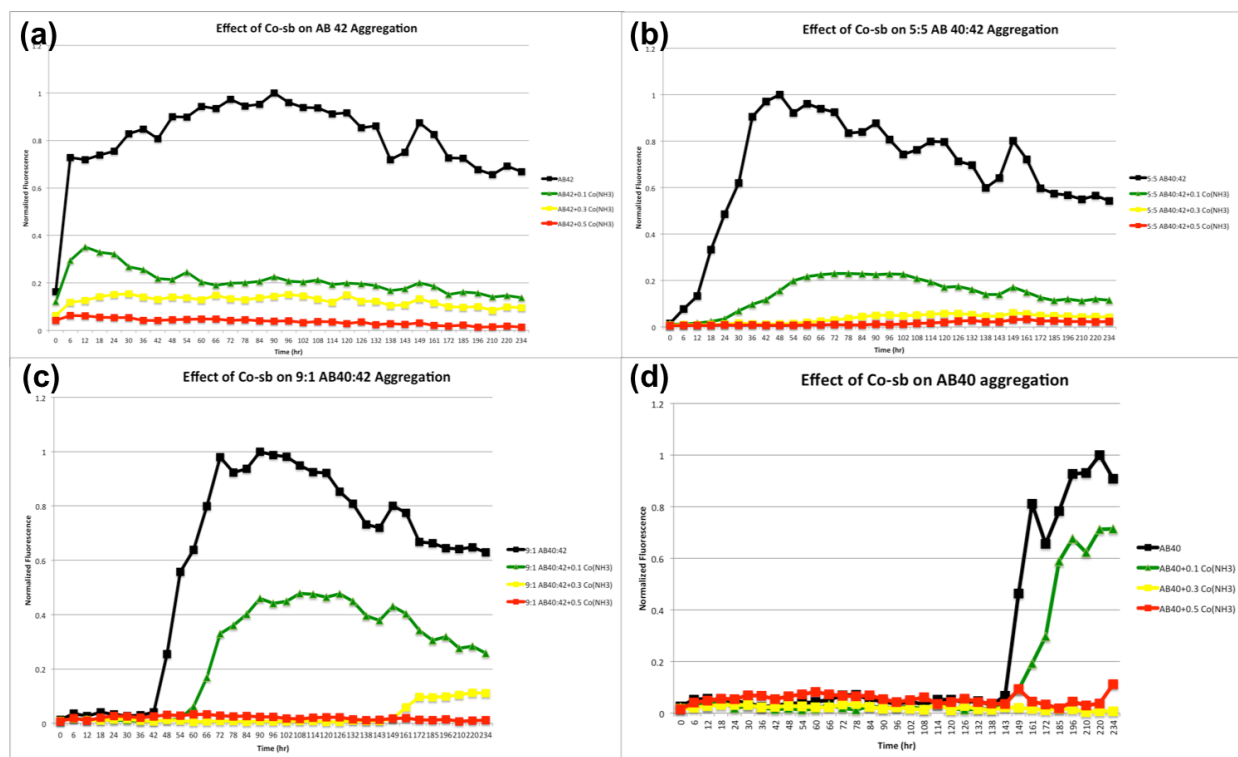


Figure 2.15: ThT fluorescence aggregation curves demonstrating Co(III)-sb inhibition of aggregation for (a) $A\beta_{42}$, (b) 5:5 $A\beta_{40}:A\beta_{42}$, (c) 9:1 $A\beta_{40}:A\beta_{42}$, and (d) $A\beta_{40}$. Untreated $A\beta$ is

represented in black, $A\beta + 0.1$ eq Co(III)-sb is in green, $A\beta + 0.3$ eq Co(III)-sb is in yellow, and $A\beta + 0.5$ eq Co(III)-sb is in red. Data presented are sample kinetic curves from each condition.

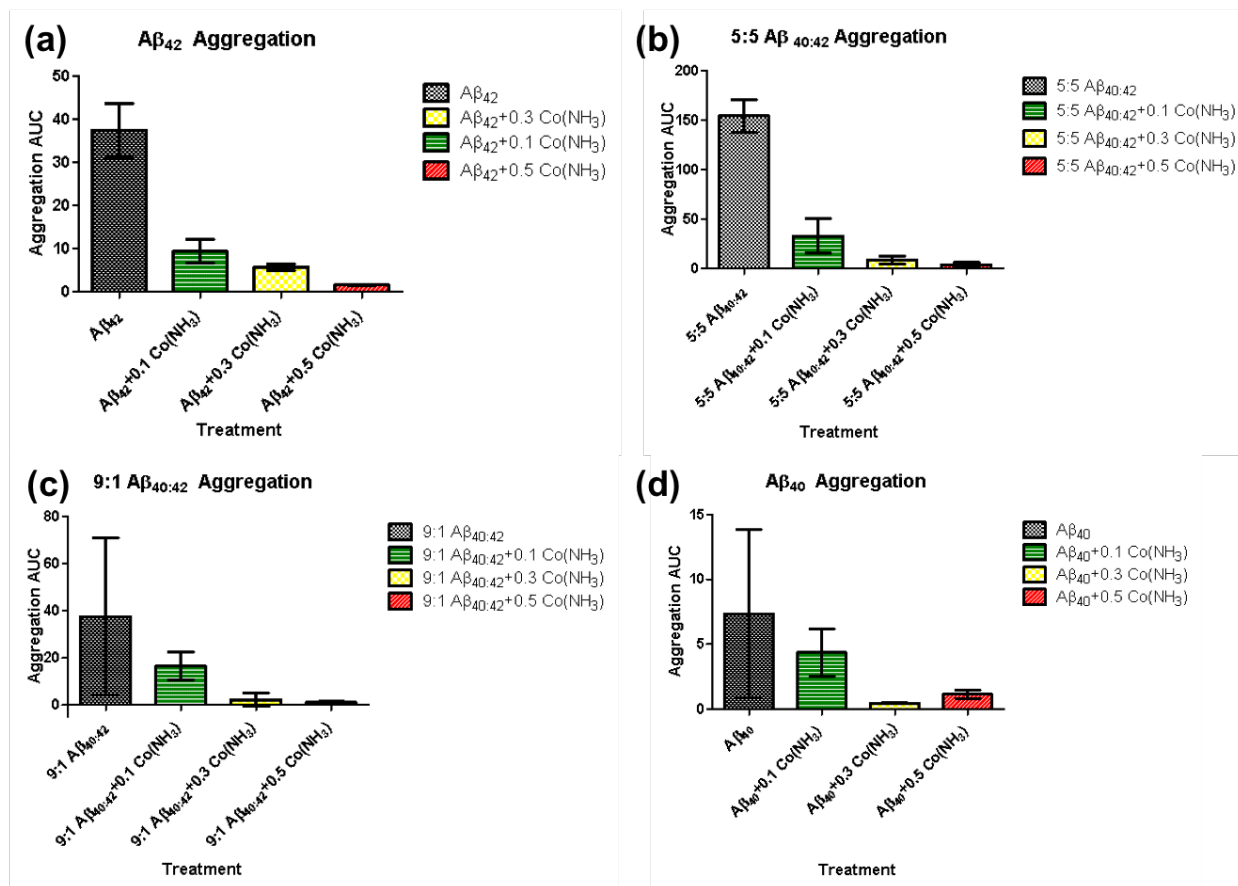


Figure 2.16: AUC analysis from ThT aggregation curves for (a) $A\beta_{42}$, (b) 5:5 $A\beta_{40}:A\beta_{42}$, (c) 9:1 $A\beta_{40}:A\beta_{42}$, and (d) $A\beta_{40}$. Untreated $A\beta$ is represented in black, $A\beta + 0.1$ eq Co(III)-sb is in green, $A\beta + 0.3$ eq Co(III)-sb is in yellow, and $A\beta + 0.5$ eq Co(III)-sb is in red. Data presented are mean AUC for kinetic curve replicates plotted as mean \pm SEM.

In order to confirm that the observed aggregation inhibition was due to coordination to Co(III)-sb, stable axial ligand negative controls (CoIm and CoDiIm) were tested by ThT

fluorescence (**Figure 2.16**). AUC data in **Figure 2.17** demonstrates that CoIm and CoDiIm are not effective negative controls, inhibiting A β aggregation in a dose-dependent manner at approximately that same level as the active complex (CoNH₃).

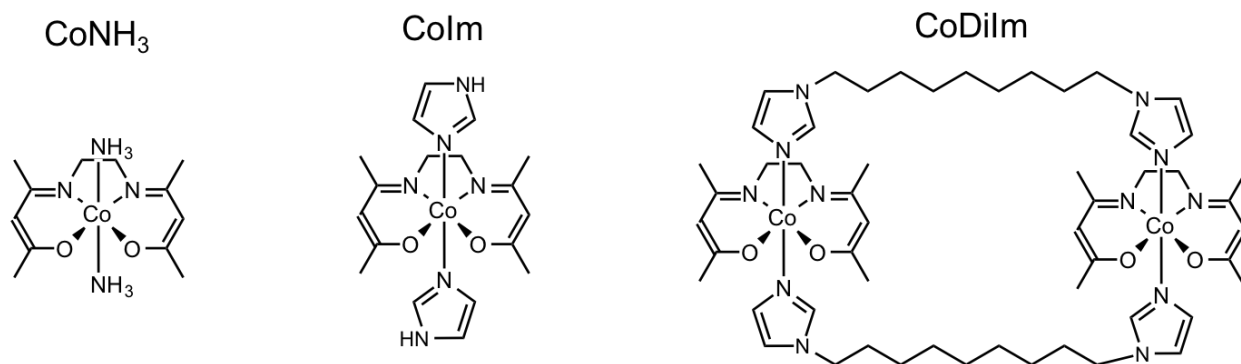


Figure 2.17: Structures of Co(III)-sb complexes used in ThT aggregation studies. CoNH₃ represents the active complex, while CoIm and CoDiIm were tested as negative controls. Direct comparison of Co(III)-sb complexes with various axial ligands L, demonstrated that CoNH₃ with bisammine ligands (L= NH₃) dissociate most readily, while CoDiIm (L= 1,10-diimidazoldecane bridging ligands) is most stable, followed by CoIm (L= imidazole).

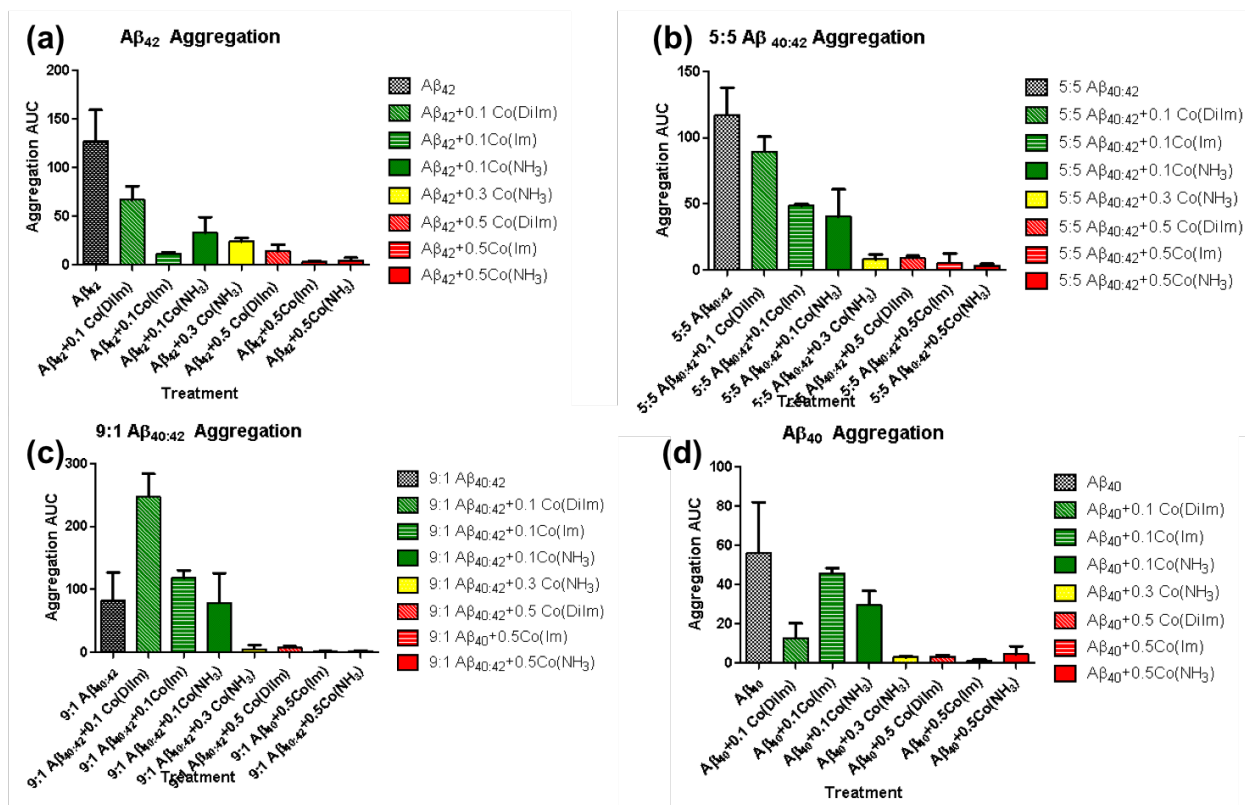


Figure 2.18: AUC analysis from ThT aggregation curves for (a) $A\beta_{42}$, (b) 5:5 $A\beta_{40}:A\beta_{42}$, (c) 9:1 $A\beta_{40}:A\beta_{42}$, and (d) $A\beta_{40}$. Untreated $A\beta$ is represented in black, $A\beta + 0.1$ eq Co(III)-sb is in green, $A\beta + 0.3$ eq Co(III)-sb is in yellow, and $A\beta + 0.5$ eq Co(III)-sb is in red. Data presented are mean AUC for kinetic curve replicates plotted as mean \pm SEM. CoIm and CoDiIm are not effective negative controls, inhibiting $A\beta$ aggregation in a dose-dependent manner at approximately that same level as the active complex ($CoNH_3$).

2.5 Discussion

ThT fluorescence assays showed robust dose-dependent inhibition of $A\beta_{40}$ and $A\beta_{42}$ aggregation. Further, this effect was specific to coordination by Co(III)-sb since the unmetallated negative control acacen did not inhibit aggregation. This inhibition was observed over a relatively

narrow dosing window with 0.1 equivalent demonstrating moderate inhibition (~30%) and 0.5 equivalents nearly completely inhibiting aggregation. Taken together, these data demonstrate potent inhibition of A β aggregation by Co(III)-sb.

Having demonstrated inhibition of A β aggregation by ThT fluorescence, we sought to confirm this effect with another kinetic assay. While most agree that ThT does not significantly alter aggregation kinetics and is therefore an excellent tool for measuring amyloid aggregation, there are some reports that suggest that the fluorophore's presence could alter the aggregation.[132] As such, it was important to choose a verification method that did not rely on exogenous agents for measurement of β -sheet content. CD spectroscopy uses differential absorption of circularly polarized light to monitor transitions in secondary structure as A β aggregates. CD experiments confirmed the trends observed in the ThT assays and additionally identified that the structural changes caused by Co(III)-sb coordination happen early in the aggregation process during the lag phase. This implies that the mechanism of Co(III)-sb likely alters the oligomeric distribution.

Fitting the ThT fluorescence data to mathematical models of A β aggregation further reinforced the idea that Co(III)-sb causes early oligomeric changes. According to the model parameters, treatment with Co(III) drastically increased the nucleation rate and drastically decreased the polymerization rate. Physically this corresponds to Co(III)-sb coordination resulting in very rapid formation of oligomers that cannot further polymerize into large aggregates. This effectively sinks the monomeric pool into Co(III)-sb-bound off-pathway aggregates.

In addition to these kinetic assays, several morphological assays were employed to further investigate the effects of Co(III)-sb on aggregation. TEM and AFM both showed stabilization of

smaller aggregates by Co(III)-sb compared to untreated A β and A β treated with the unmetallated ligand negative control.

Significant effort was spent optimizing the aggregation assay protocols and exploring the relationship between A β isoform and Co(III)-sb inhibition. The effects of lower doses of Co(III)-sb seem to be more prominent in peptide mixtures containing more of the A β_{42} isoform indicating that the effect of Co(III)-sb might be more pronounced for A β_{42} than A β_{40} . However, given the extremely long time courses of aggregation in solutions with a high ratio of A β_{40} and the tendency for increased error in the data at later time points, it may be that this effect is only due to increased error at later timepoints. For example, effects of evaporation are mitigated by sealing the plates with aluminum adhesive covers, but some evaporation is still observed after weeks at 37 °C. This could result in altered peptide and fluorophore concentrations, both of which would manifest as artificially elevated signal. Additionally, after hundreds of hours in solution, it is possible that the ThT fluorophore may experience some photobleaching, which would manifest as artificially decreased fluorescent signal.

Because these effects of extremely long assay times were particular to peptide ratios containing high amounts of A β_{40} , the data for these ratios has much higher error and is less reliable. This problem was overcome by switching to the Anaspec Aggresure A β , which demonstrates much faster aggregation times for both A β_{40} and A β_{42} isoforms. This wide variability in aggregation times based on peptide source is frustrating, but frequently reported in the literature.

In order to confirm that the observed effects on A β aggregation were due to coordination of Co(III)-sb, significant effort was spent searching for an appropriate negative control. In previous studies using Co(III)-sb to inhibit ZFTFs, Co(III)-sb complexes with highly stable axial

ligands (L= Im, 4MeIm) have been used as negative controls. Unlike the bisammine (L= NH₃) Co(III)-sb, these axial ligands do not readily dissociate in solution, thus the complex is not able to coordinate to His residues.

Previous work by our group used a fluorescently labeled imidazole (C3Im) to quantify ligand exchange dynamics for various Co(III)-sb complexes. Competition between the fluorescent imidazole and the native axial ligand leads to quenching of C3Im as it binds to Co(III)-sb. Thus the dissociation of the original axial ligand is proportional to the decrease in fluorescence of C3Im. Direct comparison of Co(III)-sb complexes with various axial ligands L, demonstrated that CoNH₃ with bisammine ligands (L= NH₃) dissociate most readily, while CoDiIm (L= 1,10-diimidazolyldecane bridging ligands) is most stable, followed by CoIm (L= imidazole).[104] However, it is important to note that none of the stable axial ligands were completely without dissociation.

Because even the stable complexes do show axial ligand exchange, we hypothesized that enough of axial ligand was dissociating to allow coordination of Co(III)-sb to the His residues of A β at a level sufficient to inhibit aggregation. In addition, factors such as heat and length of the assay, both would contribute to more axial ligand dissociation and thus greater interaction with A β . Because bulk changes in amyloid aggregation can be the result of conformational changes in a small fraction of the total peptide population (in a prion like manner), the effects of Co(III)-sb binding to a fraction of the A β monomers likely has a strong effect on the bulk aggregation. This is evident in that a substoichiometric dose of Co(III)-sb (0.5 equivalents compared to peptide monomer) demonstrates complete inhibition. While the stable axial ligand complexes CoIm and CoDiIm have been previously effective negative controls, they are unsuitable in the application of Co(III)-sb as an amyloid inhibitor.

In order to find an appropriate alternative negative control, several approaches were investigated. For example, a Ga(III) Schiff base complex was synthesized by Laura Lilley and tested for aggregation inhibition (data not shown). While this complex did show reduced inhibition of aggregation compared to the stable axial ligand Co(III)-sb complexes, it still had a small inhibitory effect. Because this complex was also an ineffective negative control and it would be impossible to discern whether the effects were from ligand effects or from changing the metal center, this approach was abandoned.

A review of the literature of coordination complexes for amyloid inhibition particularly emphasizing appropriate negative controls was conducted. From this search we concluded that literature standard often did not include any negative control since it is often impossible to generate a nonbinding control without significantly altering the chemical properties of the complex. We found one report which used the unmetallated ligand as a negative control, however the data was unreported in the manuscript [83].

2.6 Acknowledgements

We thank Sara Fernandez from Northwestern University's High Throughput Analysis Laboratory for assistance with ThT fluorescence assays, Eric Roth from Northwestern's Electron Probe Instrumentation Center (EPIC) for help with TEM imaging, and Myrick Davis and Ron Soriano from Northwestern University's Keck Biophysics Facility for their assistance with CD experiments.

This work was supported by the Northwestern University Keck Biophysics Facility and a Cancer Center Support Grant (NCI CA060553). This work made use of the EPIC facility of Northwestern University's *NUANCE* Center, which has received support from the Soft and Hybrid

Nanotechnology Experimental (SHyNE) Resource (NSF ECCS-1542205); the MRSEC program (NSF DMR-1720139) at the Materials Research Center; the International Institute for Nanotechnology (IIN); the Keck Foundation; and the State of Illinois, through the IIN. This work made use of the SPID facility of Northwestern University's NUANCE Center, which has received support from the Soft and Hybrid Nanotechnology Experimental (SHyNE) Resource (NSF ECCS-1542205); the MRSEC program (NSF DMR-1720139) at the Materials Research Center; the International Institute for Nanotechnology (IIN); the Keck Foundation; and the State of Illinois, through the IIN.

2.7 Publication Information

Sections of this chapter will be published with the following citation information:

Roberts K.F., Brue C.R., Preston A.G., Baxter, D.N., Hertzog E., Varelas E., Heffern M.C., Roth E., Meade T.J. Inhibition of amyloid- β aggregation and toxicity by Cobalt(III) Schiff base. (In preparation)

CHAPTER 3

Computational Modeling of Cobalt(III) Schiff Base Inhibition of Amyloid- β Aggregation**3.1 Abstract**

Coordination complexes have emerged as prominent modulators of amyloid aggregation via their interaction with the N-terminal histidine residues of amyloid- β (A β). Herein we report both computational and experimental data demonstrating reduction of β -sheet formation by cobalt(III) Schiff base complexes. Additionally, we report the synthesis and characterization of a novel cobalt(III) Schiff base complex with methylamine axial ligands. MD simulations of both monomeric and pentameric A β demonstrate decreased formation of β -sheet structures and destabilization of preformed β -sheets respectively. These effects exhibit a dose dependence mirrored in experimental bulk aggregation data using thioflavin T fluorescence.

3.2 Introduction

Alzheimer's disease (AD) is a progressive, neurodegenerative disorder associated with memory loss and cognitive decline [133, 134]. Pathologically AD is characterized by aggregation of the amyloid beta (A β) peptide into extracellular amyloid plaques and the formation of intracellular tau tangles. The aggregation of the soluble peptide A β into oligomers and ultimately fibrils is widely believed to be the key pathogenic mechanism for neurotoxicity [135]. *In vivo*, A β exists in two primary isoforms: A β ₄₀ which is more abundant (9:1 ratio in CSF), and A β ₄₂ which is far more prone to aggregation and thought to be more relevant to the disease process [136].

While initially unstructured when released extracellularly, A β adopts a β -sheet conformation as it aggregates [137]. *In vitro*, A β aggregation follows sigmoidal nucleation-

elongation aggregation kinetics typical of amyloidogenic peptides. Monomeric A β slowly forms small oligomeric nucleation seeds during the lag phase. Upon sufficient seed density, high molecular weight oligomers, protofibrils, and fibrils are rapidly formed during the polymerization phase until equilibrium between the various aggregates is reached. Additionally, many off-pathway aggregate species can be formed yielding a heterogeneous mixture of aggregates [27]. A variety of *in vitro* techniques have been used to measure amyloid aggregation and yielded critical insights into understanding the peptide's self-association [28].

Significant evidence implicates A β oligomers as the primary neurotoxic agent in AD [16]. Although the exact mechanism of A β -induced neuron dysfunction is unclear, there is significant evidence that endogenous metal binding affects both the aggregation *and* toxicity of the peptide [3, 4, 35-37, 138]. Specifically, A β has been shown to bind Cu(II) and Zn(II) via the N-terminal histidine residues at positions 6, 13, and 14 (His6, His13, and His14, respectively) [44, 66, 139, 140]. Previous work has used chelates (to bind metals directly) and metal coordination complexes (to bind His residues and prevent interaction). Both approaches have demonstrated successful inhibition of A β aggregation, the reduction of reactive oxygen species (ROS) generation by Cu(II)-A β , and rescue of A β toxicity to cells [63, 78, 141].

Cobalt(III) Schiff base (Co(III)-sb) complexes inhibit metalloproteins by binding to His residues via dissociative ligand exchange of labile axial ligands (Figure 1) [80, 109, 142]. Previous studies in our laboratory have demonstrated that Co(III)-sb preferentially coordinates to His residues that target specific proteins by attaching a targeting moiety coupled to the acacen equatorial ligand [100, 102, 107, 110]. For example, this strategy has been shown to selectively inhibit zinc finger transcription factors *in vivo* when conjugated to the consensus DNA sequence of the protein of interest [100, 102, 107]. Further, a Co(III)-sb complex has been shown to

coordinate the His residues of A β and disrupt aggregation resulting in the formation of large (>30 kDa) oligomers *and* reducing small toxic oligomer populations [106]. Additionally, the Co(III)-sb complex decreased synaptic binding of A β oligomers [106]. However, the mechanistic details of this Co(III)-sb inhibition of A β aggregation have not been explored.

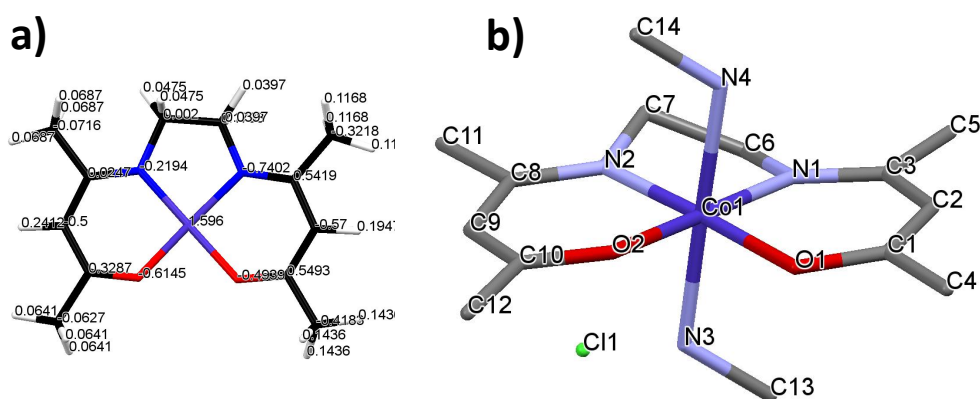


Figure 3.1: DFT optimized geometry of Co(III)-sb structure with partial charges calculated with RESP (A) X-ray crystal structure of Co(III)-sb with methylamine axial ligands (B). See Supplementary Tables 1-3 for DFT results and XRD refinement data.

Computational studies are widely used to provide atomic insight into the structural dynamics of a system. In particular, molecular dynamics (MD) simulations have been used to study the conformational changes of the A β peptide with inhibitors [143-148]. While *in vitro* methods can be used to track β -sheet formation during aggregation, these methods are limited to higher order aggregates and do not give insight into monomers and small oligomers. Since the timescale

of fibril formation is on the order of hours, classical MD cannot simulate the formation of fibrils from a solution of peptide monomers since all-atom MD is limited to aggregation processes that occur over nanoseconds.

However, there have been various attempts to simulate this self-assembly process using coarse-grained methods [149, 150]. In contrast to *in vitro* experimental methods, computational studies are well-suited for studying the early time scales of aggregation and the dynamics of monomeric and small oligomeric A β . Finally, MD simulations are useful for studying the conformations of proteins and understanding the intermolecular and intermolecular interactions that result in secondary structure formation.

Here, we describe both computational and experimental methods to investigate the effect of Co(III)-sb complexes on observed β -sheet content. We have synthesized and characterized a new Co(III)-sb complex with axial methylamine ligands that was used for parameterization of the MD simulations. The all-atom MD simulations were designed to investigate the behavior of A β_{42} peptides in the presence of Co(III)-sb complexes. Further, we describe the results from explicit-solvent MD simulations on monomers and pentamers of A β_{42} to understand the effect of Co(III)-sb complexes on structure and stability of these derivatives.

3.3 Materials and Methods

3.3.1 Parameterization of the Co(III)-sb Complex

The chemical structure of Co(III)-sb was prepared using Avogadro, and in aqueous solution at pH = 7 the Co(III)-sb complex has a +1 charge [151]. The geometry was optimized by density functional theory (DFT) using GAMESS [152]. The B3LYP density functional with a basis set of 6-31+G(d) Pople was employed for all atoms [106, 153-155]. The atomic point charges of the

optimized Co(III)-sb were calculated using the restrained electrostatic potential (RESP) method implemented in Amber16 software [156, 157]. We used the general AMBER force field (GAFF) to model Co(III)-sb (partial charge values and Amber GAFF atom types are shown in **Table 3.1**) [158].

Figure 3.1a shows the optimized geometry from the DFT calculation along with the partial charges. The nonbonded constants for cobalt (atom type CO) were taken from Cheatham et. al. 1997 [159]. The mass and nonbonded constants for “nr” and “nl” were taken from the atom type “na” in GAFF. The constants for “ox” and “oy” were taken from the atom type “os” in GAFF. Bond lengths, bond angles, and dihedral angles were determined using the crystal structure solved in this paper. The parameters used to model Co(III)-sb are provided in **Tables 3.1-3**.

Table 3.1: Crystal data and structure refinement for [Co(acacen)(CH₃NH₂)₂]Cl

Empirical formula	C ₁₄ H ₃₄ ClCoN ₄ O ₅
Formula weight	432.83
Temperature / K	100.01
Crystal system	monoclinic
Space group	Pn
a / Å, b / Å, c / Å	9.2260(3), 7.2438(3), 15.2785(5)
α /°, β /°, γ /°	90, 90.349(3), 90
Volume / Å ³	1021.06(6)
Z	2
ρ_{calc} / mg mm ⁻³	1.408
μ / mm ⁻¹	8.057

F(000)	460
Crystal size / mm ³	0.119 × 0.065 × 0.004
2 Θ range for data collection	11.172 to 127.658°
Index ranges	-10 ≤ h ≤ 10, -8 ≤ k ≤ 8, -13 ≤ l ≤ 17

Table 3.2: RESP Partial charges and GAFF atom types for Co(III)-sb calculated from DFT minimized structure.

Atom	GAFF	Charge
Name	Atom	
	Type	
C1	ce	0.5419
C2	ce	-0.5700
C3	cf	0.5493
O4	ox*	-0.4939
N5	nr*	-0.7402
CO6	CO*	1.5960
N7	nl*	-0.2194
O8	oy*	-0.6145
C9	ce	0.0247
C10	ce	-0.5000
C11	cf	0.3287
C23	c3	0.0020

C24	c3	0.1793
H25	h1	0.0475
H26	h1	0.0475
H27	h1	0.0397
H28	h1	0.0397
H30	ha	0.2412
H31	ha	0.1947
C32	c3	-0.3218
H33	hc	0.1168
H34	hc	0.1168
H35	hc	0.1168
C36	c3	-0.0716
H37	hc	0.0687
H38	hc	0.0687
H39	hc	0.0687
C40	c3	-0.4183
H41	hc	0.1436
H42	hc	0.1436
H43	hc	0.1436
C44	c3	-0.0627
H45	hc	0.0641
H46	hc	0.0641

H47 hc 0.0641

*Additional atom types not found in GAFF that were used to describe the atoms in the Co(III)-sb

Table 3.3: Bonded (bonds, angles, dihedrals) and nonbonded parameters for additional atom types (CO, nr, nl, ox,oy) used in Co(III)-sb from DFT geometry optimization

Atom type	Mass (g)		
CO	58.9332		
nr	14.01		
nl	14.01		
ox	16		
oy	16		
BONDS	harmonic force constant (kcal/mol/ Å²)	length (Å)	
ce-nr	299.00	1.312	
cf-ox	300.00	1.289	
CO-ox	300.00	1.898	
CO-nr	300.00	1.905	
c3-nr	283.30	1.462	
CO-nl	300.00	1.891	
CO-oy	300.00	1.908	
ce-nl	299.00	1.322	
c3-nl	283.30	1.465	

cf-oy	300.00	1.292
NB-CO	500.00	1.947
ANGLES	harmonic force constant	angle
	(kcal/mol/rad²)	(deg)
CO-nr-ce	70.000	126.7
c3-nr-ce	70.000	121.9
ce-ce-nr	70.000	120.5
ce-cf-ox	70.000	125.1
CO-ox-cf	70.000	124.8
c3-cf-ox	70.000	114.6
nr-CO-ox	70.000	94.5
nl-CO-ox	70.000	177.3
ox-CO-oy	70.000	83.5
c3-ce-nr	35.000	120
nr-CO-nl	70.000	86.6
nr-CO-oy	70.000	177.2
c3-c3-nr	35.000	109.6
h1-c3-nr	49.830	108.8
CO-nr-c3	70.000	111.7
CO-nl-ce	70.000	125.9
CO-nl-c3	70.000	110.7
CO-oy-cf	70.000	123.2

nl-CO-oy	70.000	95.5
ce-ce-nl	35.000	121.3
c3-ce-nl	70.000	120.5
c3-c3-nl	70.000	109.1
h1-c3-nl	49.830	108.8
ce-cf-oy	70.000	126.1
c3-cf-oy	35.000	114.5
c3-nl-ce	35.000	111.6
CV-NB-CO	70.000	130.6
NB-CO-ox	70.000	90.8
NB-CO-nr	70.000	89.6
NB-CO-oy	70.000	88.4
NB-CO-nl	70.000	91.7
NB-CO-NB	70.000	178.9
CR-NB-CO	70.000	124.6

DIHEDRALS	factor for torsional barrier	barrier height/2	phase shift angle (deg)	periodicity
ox-CO-nr-ce	1	1	0.000	2.000
nl-CO-nr-ce	1	1	180.000	2.000
oy-CO-nr-ce	1	1	0.000	2.000

c3-c3-nr-ce	9	1.4	180.000	3.000
h1-c3-nr-ce	9	1.4	180.000	-3.000
h1-c3-nr-ce	9	1.4	0.000	1.000
ce-ce-nr-CO	6	0	0.000	3.000
ce-ce-nr-c3	6	0	180.000	3.000
hc-c3-ce-ce	1	0.38	180.000	-3.000
hc-c3-ce-ce	1	0	0.000	-2.000
hc-c3-ce-ce	1	1.15	0.000	1.000
ce-cf-ox-CO	1	1	0.000	2.000
hc-c3-cf-ce	1	0.38	180.000	-3.000
hc-c3-cf-ce	1	0	0.000	-2.000
hc-c3-cf-ce	1	1.15	0.000	1.000
nr-CO-ox-cf	1	1	0.000	2.000
nl-CO-ox-cf	1	1	0.000	2.000
oy-CO-ox-cf	1	1	180.000	2.000
hc-c3-cf-ox	6	0	0.000	3.000
ox-CO-nr-c3	1	1	180.000	2.000
ox-CO-nl-ce	1	1	180.000	2.000
ox-CO-nl-c3	1	1	0.000	2.000
ox-CO-oy-cf	1	1	180.000	2.000
hc-c3-ce-nr	1	0.38	180.000	-3.000
hc-c3-ce-nr	1	0	0.000	-2.000

hc-c3-ce-nr	1	1.15	0.000	1.000
nr-CO-nl-ce	1	1	180.000	2.000
nr-CO-nl-c3	1	1	0.000	2.000
nr-CO-oy-cf	1	1	180.000	2.000
c3-cf-ox-CO	1	1	180.000	2.000
c3-ce-nr-CO	6	0	180.000	3.000
c3-c3-nr-CO	9	1.4	0.000	3.000
h1-c3-nr-CO	9	1.4	180.000	-3.000
h1-c3-nr-CO	9	1.4	0.000	1.000
ce-ce-nl-CO	6	0	0.000	3.000
c3-ce-nl-CO	6	0	180.000	3.000
c3-c3-nl-CO	9	1.4	0.000	3.000
h1-c3-nl-CO	9	1.4	180.000	-3.000
h1-c3-nl-CO	9	1.4	0.000	1.000
ce-cf-oy-CO	1	1	0.000	2.000
c3-cf-oy-CO	1	1	180.000	2.000
nl-CO-nr-c3	1	1	0.000	2.000
nl-CO-oy-cf	1	1	180.000	2.000
hc-c3-ce-nl	1	0.38	180.000	-3.000
hc-c3-ce-nl	1	0	0.000	-2.000
hc-c3-ce-nl	1	1.15	0.000	1.000
oy-CO-nr-c3	1	1	180.000	2.000

oy-CO-nl-ce	1	1	180.000	2.000
oy-CO-nl-c3	1	1	0.000	2.000
hc-c3-cf-oy	6	0	0.000	3.000
c3-c3-nl-ce	9	1.4	180.000	3.000
h1-c3-nl-ce	9	1.4	180.000	-3.000
h1-c3-nl-ce	9	1.4	0.000	1.000
ce-ce-nl-c3	6	0	180.000	3.000
c3-ce-nl-c3	6	0	0.000	3.000
c3-ce-nr-c3	6	0	0.000	3.000
CV-NB-CO-ox	1	1	0.000	2.000
CV-NB-CO-nr	1	1	0.000	2.000
CV-NB-CO-oy	1	1	180.000	2.000
CV-NB-CO-nl	1	1	180.000	2.00
CV-NB-CO-NB	1	1	180.000	2.000
NB-CO-ox-cf	1	1	180.000	2.000
NB-CO-nr-ce	1	1	180.000	2.000
NB-CO-nr-c3	1	1	0.000	2.000
NB-CO-oy-cf	1	1	0.000	2.000
NB-CO-nl-ce	1	1	0.000	2.000
NB-CO-nl-c3	1	1	0.000	2.000
CR-NB-CO-ox	1	1	180.000	2.000
CR-NB-CO-nr	1	1	180.000	2.000

CR-NB-CO-oy	1	1	0.000	2.000
CR-NB-CO-nl	1	1	0.000	2.000
CR-NB-CO-NB	1	1	0.000	2.000

NONBONDED	Van der Waals shift radius	6-12
PARAMETERS	(Å)	potential well depth (kcal/mol)
CO	0.5000	0.01
nr	1.8240	0.17
nl	1.8240	0.17
ox	1.6837	0.17
oy	1.6837	0.17

3.3.2 Molecular Dynamics Simulations

All simulations were performed using the GROMACS 5.0.3 package with the AMBER99SB-ILDN force field [160-162]. The coordinates of A β ₄₂ monomer were taken from PDB entry 1IYT [163]. Previously, it was reported that the most energetically favorable coordination of Co(III)-sb is bidentate at His6 and either His13 or His14 [106]. Therefore, we placed Co(III)-sb in the space between His 6 and His 13 residues and created bonds between the imidazole nitrogen of His6 and the cobalt of Co(III)-sb, as well as imidazole nitrogen of His13 and the cobalt of Co(III)-sb. His13 was chosen over His14 based on the geometry of the initial A β ₄₂

structure. A β_{42} monomer with Co(III)-sb was placed in the center of a cubic box of dimensions 20 Å x 20 Å x 20 Å and periodic boundary conditions in all directions were applied. The box was solvated with the TIP3P water model and 2 Na⁺ counter ions were added to balance the net charge of A β_{42} (-3 at pH7) and Co(III)-sb (+1 at pH 7) [164]. In addition, 42 ions of Na⁺ and 42 ions of Cl⁻ were also added to mimic 150 mM NaCl concentration from the experimental study.

All bond lengths with hydrogen were constrained with the LINCS algorithm [165]. The system was minimized for 50,000 steps using the steepest descent method. The system was then equilibrated for 200 ps with 2 fs time step under isochoric-isothermal (NVT) ensemble using V-rescale coupling method to maintain a temperature of 310 °K [166]. We further equilibrated the system under isothermal-isobaric (NPT) for 800 ps using the V-rescale thermostat and Parrinello-Rahman barostat to maintain temperature (310 °K) and pressure (1 bar), respectively [166-168]. The A β_{42} peptide and Co(III)-sb were position restrained up to this point in the equilibration.

In the final equilibration, the system was simulated using NPT with no position restraints for 2 ns. Finally, a NPT production run was performed for 250 ns, which was used to collect all the data presented in this paper. For NPT simulations, isotropic pressure coupling with a time constant of 2 ps was used. Verlet cutoff scheme was used for neighbor searching [169]. Long-range electrostatics were determined with the smooth particle mesh Ewald (PME) method using cubic interpolation and Fourier grid spacing of 0.16 nm [170, 171]. A cut-off of 1 nm was used for evaluation of all non-bonded interactions. Atomic coordinates were saved every 100 ps for the trajectory analysis.

The coordinates of the A β_{42} pentamer were taken from PDB entry 5OQV [15]. This published atomistic structure is of a heterodimer protofibril consisting of a pentamer and tetramer. We only used the pentamer unit of the dimer in our simulations in order to reduce the

computational cost, while still demonstrating the effect Co(III)-sb effect on preformed fibril structure. Co(III)-sb complexes were coordinated to the imidazole nitrogen of His 6 and His 13 of each of the five A β ₄₂ peptide chains in the pentamer. The pentamer was then placed in box of dimensions 25 Å x 25 Å x 25 Å and periodic boundary conditions in all directions were applied.

The box was solvated with the TIP3P water model and 10 Na⁺ counter ions were added to balance the net charge of five A β ₄₂ peptides (-15 at pH 7) and five Co(III)-sb complexes (+5 at pH 7).[164] We also added 81 ions of Na⁺ and 81 ions of Cl⁻ to mimic 150 mM NaCl concentration from the experimental study. The same settings for the minimization, equilibrations, and production simulations were used as for the monomer. The pentamer NPT production simulations were run for 100 ns and were used to collect all the data presented in this paper. Atomic coordinates were saved every 100 ps for the trajectory analysis.

The auxiliary programs provided with GROMACS 5.0.3 package were used to analyze simulation trajectories. For secondary structure analysis, the DSSP algorithm was used [172]. Contact maps were calculated using gmx mdmat and selecting the protein for analysis. Block averaging method was used to calculate averages over simulation trajectory. Hydrogen bonds between peptide chains were computed using gmx h-bond between each neighboring peptide chain in the pentamer over the simulation time. We used this data to calculate an average number of hydrogen bonds between the chains at each time.

Distance between the center of mass of peptide chains in the pentamer were calculated using VMD. Snapshots of the simulation trajectories were visualized using visual molecular dynamics (VMD) [173].

For the pentamer MD simulations conducted at different equivalencies of Co(III)-sb the system was constructed and equilibrated using the same methodology as for the initial pentamer

simulation conducted with a Co(III)-sb bound to each monomer unit within the structure. For the lower equivalency simulations, only the appropriate number of Co(III)-sb were added to the starting structure to establish the desired equivalency with respect to the five monomer units. (i.e. 1 Co(III)-sb/5 monomer units in the pentamer structure is an equivalency of 0.2 eq Co(III)-sb). Secondary structure content was determined by DSSP algorithm in GROMACS as before. The average number of residues found in a β -sheet structure from the DSSP analysis was divided by the total number of protein residues (210) to determine percentage. Error bars are standard deviation of the number of residues found.

3.3.3 Synthesis of [Co(acacen)(CH₃NH₂)₂]Cl

[Co(acacen)(CH₃NH₂)₂]Cl (1) was synthesized according to modified literature procedures (Manus 2013) [109]. H₂(acacen) ligand was synthesized as described in [109]. H₂(acacen) (150 mg, 660 μ mol, 1.0 eq) was dissolved in 10 mL methanol under N₂ and stirred for 10 min. CoCl₂ (175 mg, 735 μ mole, 1.1 eq) was dissolved in 5 mL under N₂ and stirred for 10 min. The pink CoCl₂ solution was transferred to the H₂(acacen) solution along with 5 mg of activated carbon (DARCO®, 20-40 mesh, granular). O₂ gas was bubbled through the solution and it was stirred for 12 hours. CH₃NH₃Cl (50 mg, 735 μ mole, 1.1 eq), and NaOH (40 mg, 1 mmol, 1.51 eq) were dissolved in 10 mL methanol and stirred for 30 min.

The resulting solution was transferred to the brown solution, affixed with a reflux condenser, and heated to 55 °C for 2 hr. The reaction mixture was cooled to room temperature and the solvent was removed by rotary evaporation. The crude product was redissolved in minimal methanol and precipitated in diethyl ether. The product was collected to yield a dark brown powder

(61% yield)(1). ^1H NMR (500 MHz CDCl_3) 1.01 (s, 6H) 2.07 (s, 6H) 2.29 (s, 6H), 3.41 (t, 4H), 4.98 (s, 2H). ESI MS calc. 343.15 m/z, [obs. 343.18 m/z].

3.3.4 X-ray Crystallography

Single crystals of 1 were obtained by vapor diffusion of ether into ethanol. A suitable crystal was mounted on a MITIGEN holder in Paratone oil on a Bruker Kapp APEX CCD area detector diffractometer. Crystals were maintained at 100.1 K during data collection and the structure was solved using Olex2. The ShelXT structure solution program employed intrinsic phasing and was refined with the ShelXL refinement package using least squares minimization.

Table 3.4: Crystal Structure Fractional Atomic Coordinates ($\times 10^4$) and Equivalent Isotropic Displacement Parameters ($\text{\AA}^2 \times 10^3$) for cx1210a. U_{eq} is defined as 1/3 of of the trace of the orthogonalised U_{IJ} tensor.

Atom	x	y	z	U_{eq}
Co1	5039.2(12)	2443.8(14)	5041.9(9)	11.4(2)
O1	5578(5)	2015(6)	3854(3)	16.1(10)
O2	3196(5)	3009(6)	4535(3)	15.1(10)
N1	6871(6)	1823(7)	5525(4)	15.7(12)
N2	4457(6)	2942(7)	6205(3)	14.6(12)
N3	5563(6)	5060(7)	4914(3)	14.4(12)
N4	4537(6)	-209(7)	5158(4)	15.1(12)
C1	6757(7)	1160(8)	3633(4)	17.1(15)
C2	7850(7)	632(8)	4190(4)	17.6(15)

C3	7922(7)	1009(8)	5104(5)	18.0(15)
C4	6852(8)	751(9)	2665(4)	23.7(16)
C5	9273(8)	411(10)	5582(5)	25.6(16)
C6	6991(7)	2366(8)	6443(5)	18.4(13)
C7	5525(7)	2319(7)	6861(4)	17.0(13)
C8	3252(7)	3771(8)	6437(4)	16.5(15)
C9	2190(7)	4321(8)	5818(4)	17.2(14)
C10	2194(7)	3943(8)	4933(4)	17.2(15)
C11	2978(7)	4201(9)	7390(4)	22.6(16)
C12	985(7)	4579(10)	4349(5)	24.7(16)
C13	7059(7)	5540(8)	4639(4)	18.3(15)
C14	3029(7)	-726(9)	5401(5)	21.1(15)
O4	4195(7)	7434(6)	3480(4)	30.9(15)
O3	2187(6)	310(6)	3337(3)	30.7(11)
O5	4178(5)	4155(6)	2499(3)	26.5(10)
Cl1	6102(2)	7347.3(19)	6735.3(12)	22.8(4)

Table 3.5: Crystal Structure Bond Lengths for $[\text{Co}(\text{acacen})(\text{CH}_3\text{NH}_2)_2]\text{Cl}$

Atom	Atom	Length/Å	Atom	Atom	Length/Å
Co1	O1	1.910(5)	N3	C13	1.486(8)
Co1	O2	1.909(5)	N4	C14	1.490(8)
Co1	N1	1.894(6)	C1	C2	1.370(10)
Co1	N2	1.895(5)	C1	C4	1.511(9)

Co1	N3	1.966(5)		C2	C3	1.424(9)
Co1	N4	1.985(5)		C3	C5	1.506(10)
O1	C1	1.297(8)		C6	C7	1.500(8)
O2	C10	1.300(8)		C8	C9	1.416(10)
N1	C3	1.308(8)		C8	C11	1.511(9)
N1	C6	1.461(9)		C9	C10	1.379(9)
N2	C7	1.472(8)		C10	C12	1.497(9)
N2	C8	1.314(8)				

Table 3.6: Crystal Structure Bond Angles for $[\text{Co}(\text{acacen})(\text{CH}_3\text{NH}_2)_2]\text{Cl}$

Atom	Atom	Atom	Angle/°	Atom	Atom	Atom	Angle/°
O1	Co1	N3	89.8(2)	C8	N2	Co1	125.8(5)
O1	Co1	N4	89.4(2)	C8	N2	C7	121.3(5)
O2	Co1	O1	83.46(19)	C13	N3	Co1	118.9(4)
O2	Co1	N3	88.4(2)	C14	N4	Co1	119.0(4)
O2	Co1	N4	92.0(2)	O1	C1	C2	125.9(6)
N1	Co1	O1	95.4(2)	O1	C1	C4	113.7(6)
N1	Co1	O2	178.4(3)	C2	C1	C4	120.4(6)
N1	Co1	N2	86.4(2)	C1	C2	C3	125.8(6)
N1	Co1	N3	92.8(2)	N1	C3	C2	122.7(6)
N1	Co1	N4	86.8(2)	N1	C3	C5	120.3(6)
N2	Co1	O1	177.8(3)	C2	C3	C5	117.0(6)
N2	Co1	O2	94.7(2)	N1	C6	C7	109.8(5)

N2	Co1	N3	88.9(2)	N2	C7	C6	107.8(5)
N2	Co1	N4	91.9(2)	N2	C8	C9	122.1(6)
N3	Co1	N4	179.1(3)	N2	C8	C11	120.0(6)
C1	O1	Co1	123.2(4)	C9	C8	C11	117.8(6)
C10	O2	Co1	123.8(4)	C10	C9	C8	126.4(6)
C3	N1	Co1	125.3(5)	O2	C10	C9	124.6(6)
C3	N1	C6	122.8(6)	O2	C10	C12	114.2(6)
C6	N1	Co1	111.9(4)	C9	C10	C12	121.2(6)
C7	N2	Co1	112.8(4)				

3.3.5 Amyloid- β Preparation and Thioflavin T Assay

A β_{42} was purchased from Anaspec. Peptide was resuspended and diluted in 20 mM HEPES, 150 mM NaCl to a final concentration of 50 μ M A β_{42} . A fresh solution of Thioflavin T was prepared for each assay and syringe filtered before use. Thioflavin T was added to the peptide mixture at a final concentration of 200 μ M. Co(III)-sb and unmetallated acacen ligand (negative control) were added to the samples at concentrations ranging from 5 to 25 μ M. Negative controls consisting of ThT and Co(III)-sb were run to ensure that Co(III)-sb does not alter ThT fluorescence. Samples were plated in quadruplicate on 384 well black, clear flat bottom polystyrene non-binding surface plates (Corning 3544).

Plates were sealed with aluminum plate seals to prevent sample evaporation. All peptide manipulation was performed using non-binding tips to avoid protein loss. Fluorescence was measured through the plate bottom every 5 minutes for 2 hours at excitation 440 nm and emission 484 nm on a Synergy H1M plate reader. Samples were kept at 37 °C under orbital agitation (252

rpm) in the plate reader between reads. Kinetic data from two separate plates was pooled and plotted using Graphpad Prism. Error bars represent standard error of the mean (SEM). Area under the curve was calculated for each replicate and data is presented as mean \pm SEM.

3.4 Results

3.4.1 Monomeric Amyloid- β Simulations

In order to understand the role of Co(III)-sb as an aggregation inhibitor, we performed MD simulations of the monomer and pentamer systems of A β ₄₂. Simulations consisting of monomeric A β ₄₂ with and without bound Co(III)-sb in water were used to gain insight into how Co(III)-sb affects the conformation of the peptide as it unfolds in solution. From these simulations, we describe how different regions of the A β ₄₂ peptide sequence interact in the presence of Co(III)-sb. We performed simulations in which we tested the stability of preformed A β ₄₂ pentamers in the presence and absence of Co(III)-sb complex. The initial model used for the pentamer simulations was a portion of published protofibril structure (PDB 5OQV) solved using cryo-electron microscopy [15]. The atomic resolution model published was a heterodimer consisting of pentameric and tetrameric units. We only used the pentamer unit of the dimer in our simulations in order to reduce the computational cost, while still demonstrating the effect Co(III)-sb effect on preformed A β ₄₂ β -sheet structure.

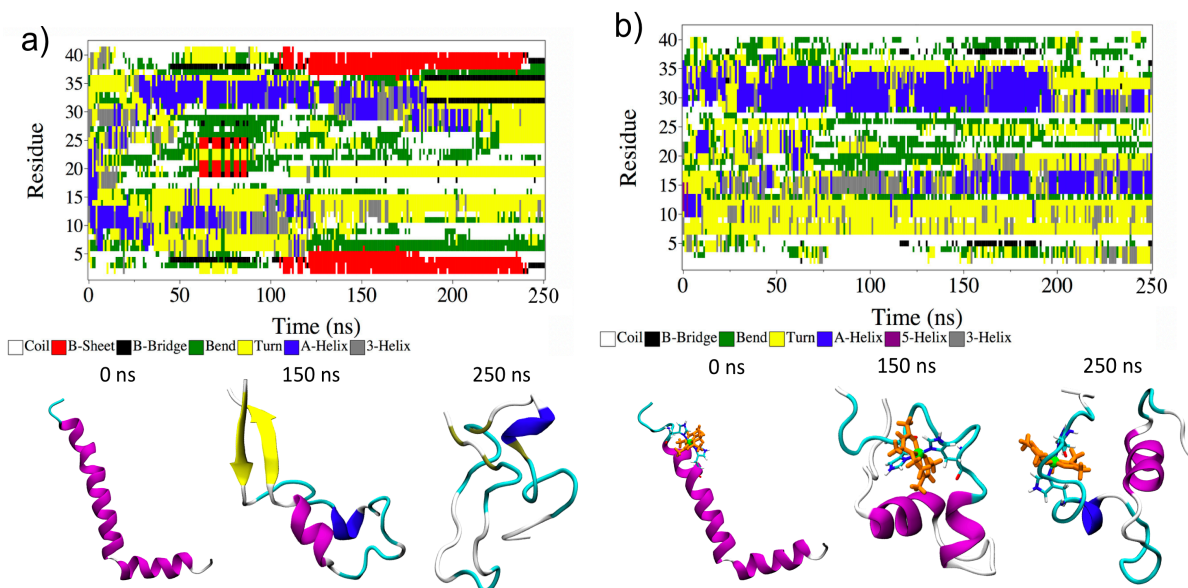


Figure 3.2: Secondary structure information (DSSP) and conformations over 250 ns simulation time (a) of the Aβ₄₂ monomer only and (b) of the Aβ₄₂ monomer with bound Co(III)-sb. In the snapshots, the secondary structures of Aβ₄₂ are colored as follows: α-helix: purple, 3₁₀-helix: blue, extended-β: yellow, bridge-β: tan, turn: cyan, random coil: white. Co(III)-sb is shown in orange, and the Co(III) center is green. We also show the His6 and His13 residues bonded to Co(III)-sb. The side chains of the Aβ₄₂, hydrogens, water, and ions are omitted for clarity.

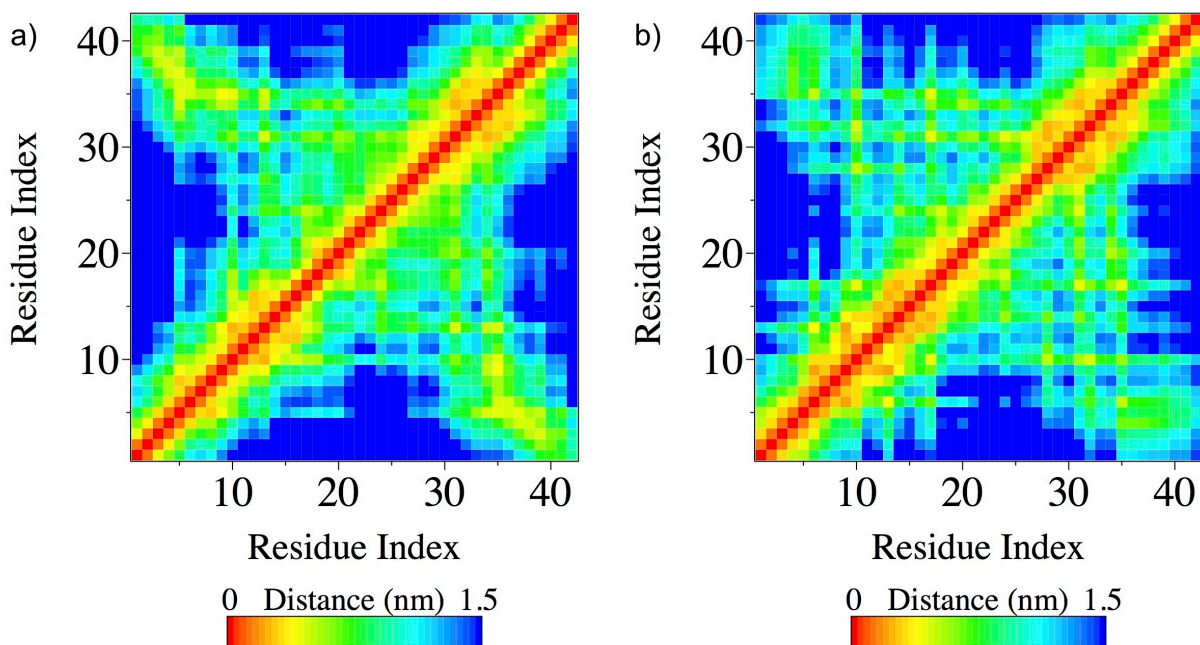


Figure 3.3: Contact maps for monomer simulations of (a) $A\beta_{42}$ only and (b) $A\beta_{42}$ with bound Co(III)-sb.

We calculated the contact maps for the two systems studied. A contact map shows which residues are in close proximity to each other. This data was calculated from 250 ns of simulation trajectory using a block averaging method. When Co(III)-sb is not present, the N- (residues 1-5) and C-termini (residues 35-42) are in close proximity (**Figure 3.3a**). The hydrogen bonding interactions between the N- and C-termini are not as pronounced in the system with Co(III)-sb (**Figure 3.3b**). Also, we can observe that overall the $A\beta_{42}$ residues are not as close to each other when Co(III)-sb is bound compared to the system with only the $A\beta_{42}$ monomer.

3.4.2 Pentameric Amyloid- β Simulations

The pentamer simulations were performed for 100 ns to determine the effect of Co(III)-sb on stability of pre-formed $A\beta_{42}$ aggregates. Because chains closer to the surface of the pentamer

will be less stable as they are more exposed to water, we report the secondary structure information for the middle chain in **Figure 3.7**. In the $A\beta_{42}$ pentamer only system, the β -sheets are stable throughout the simulation time as a result of the peptide's ability to maintain the hydrogen bonds formed between protein monomers (**Figure 3.4a**). As shown in **Figure 3.4b**, the presence of Co(III)-sb causes the β -sheets to become less continuous. Particularly for residues 6 through 13, where the Co(III)-sb is bound, there is a complete break-up of the β -sheets. Further destabilization of β -sheets can be seen in residues 27-30 in the system with Co(III)-sb. The average number of residues in a β -sheet structure over the simulation time was 136.832 for the $A\beta_{42}$ pentamer only system and 97.753 for the $A\beta_{42}$ pentamer with bound Co(III)-sb. This indicates a 28.56% decrease in β -sheet content with bound Co(III)-sb.

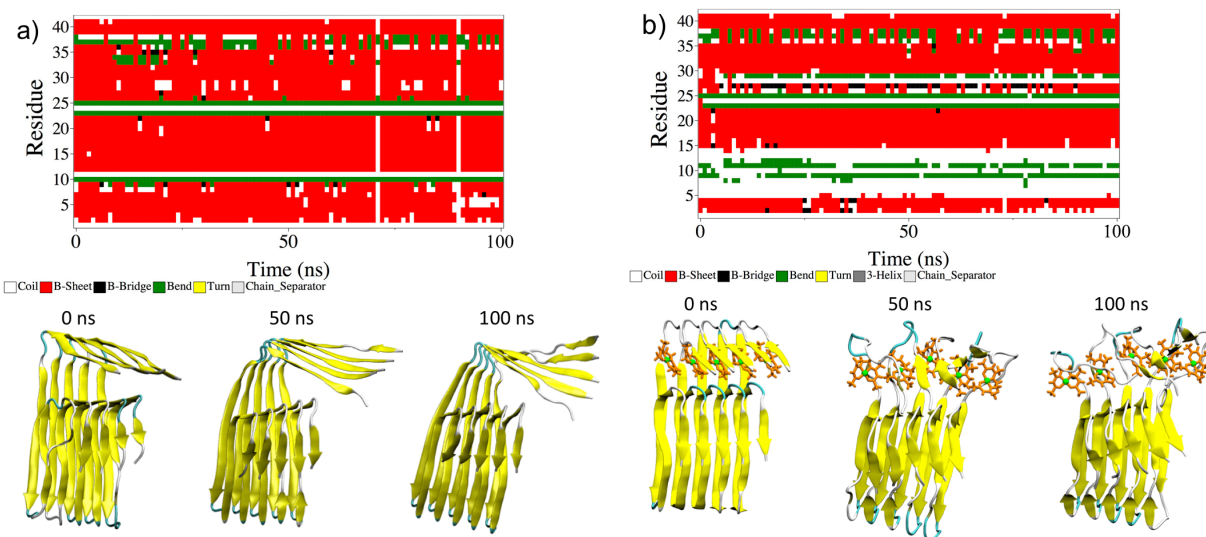


Figure 3.4: Secondary structure information (DSSP) and conformations over 100 ns simulation time (a) of the $A\beta_{42}$ pentamer only and (b) of the $A\beta_{42}$ pentamer with bound Co(III)-sb. In the snapshots, the secondary structures of $A\beta_{42}$ are colored as follows: α -helix: purple, 3_{10} -helix: blue, extended- β : yellow, bridge- β : tan, turn: cyan, random coil: white. Co(III)-sb is shown in orange,

and the Co(III) center is green. The side chains of A β ₄₂, hydrogens, water, and ions are omitted for clarity.

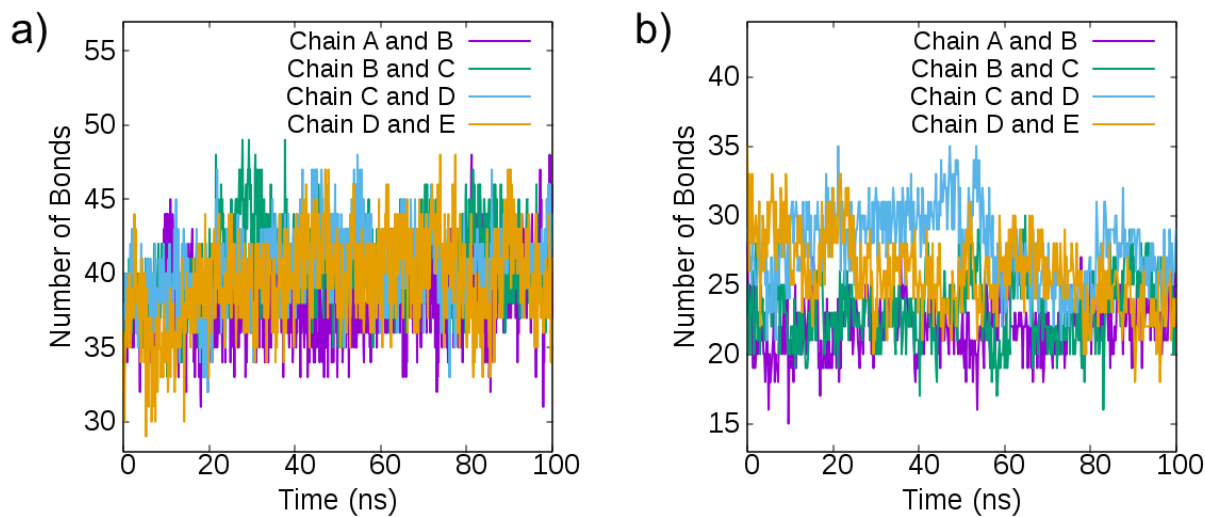


Figure 3.5: Number of hydrogen bonds between neighboring chains in the pentamer for (a) A β ₄₂ only and (b) A β ₄₂ with Co(III)-sb.

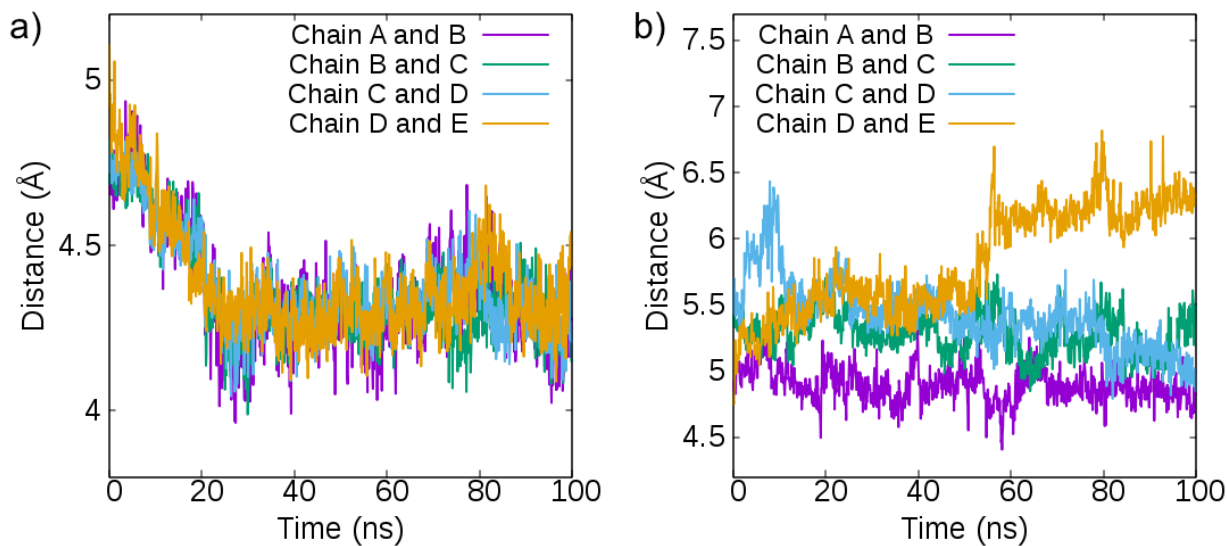


Figure 3.6. Distance between neighboring chains in the pentamer for (a) $A\beta_{42}$ only and (b) $A\beta_{42}$ with Co(III)-sb.

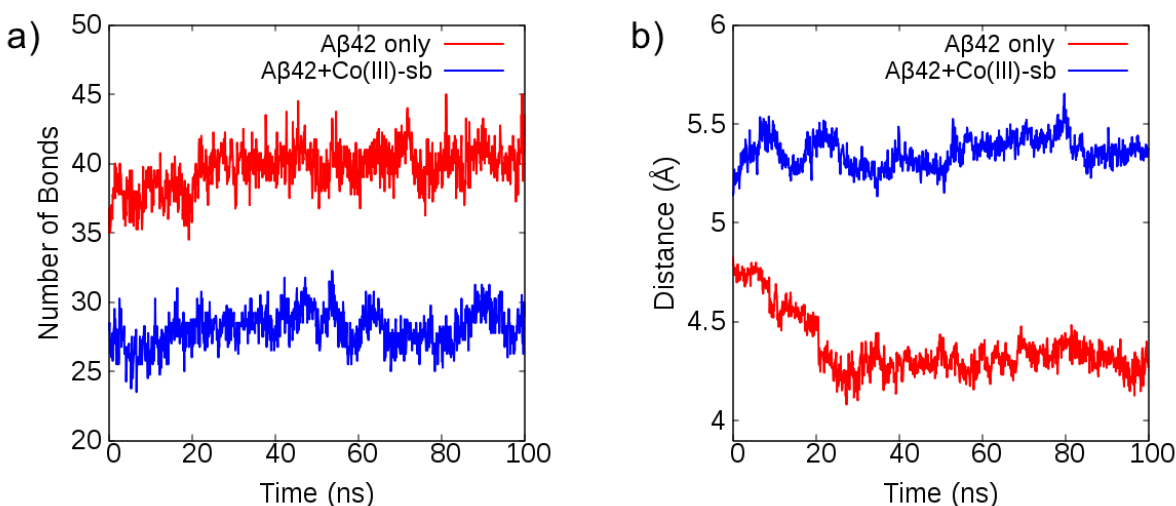


Figure 3.7: (a) The average hydrogen bond number between neighboring peptide chains for $A\beta_{42}$ pentamer only and $A\beta_{42}$ pentamer with bound Co(III)-sb. (b) The average distance between neighboring chains for $A\beta_{42}$ pentamer only and $A\beta_{42}$ pentamer with bound Co(III)-sb.

We performed hydrogen bond analysis to explore the change in number of hydrogen bonds over the simulation time. The number of hydrogen bonds between neighboring chains for both simulated systems was calculated (**Figure 3.5**). The average of these values is shown in Figure 3.7a. A decrease in hydrogen bonding is observed when Co(III)-sb is bound to the $A\beta_{42}$ pentamer system compared to the protein only system. The average number of hydrogen bonds over the simulation time when with and without Co(III)-sb are 39.679 and 28.080 respectively. Fewer hydrogen bonds indicates less β -sheet content.

From the conformations of peptide chains in **Figure 3.4**, we observe that the chains are more spread apart in presence of Co(III)-sb. To quantify this observation, the distance between the center of mass of adjacent chains was calculated (**Figure 3.6**). The average of these values is shown in **Figure 3.7b**. There is an increase in distance when Co(III)-sb is bound compared to when Co(III)-sb is absent. The average distance between the peptide chains over the simulation time is 5.357 Å when Co(III)-sb is bound to A β ₄₂, while it is 4.369 Å when Co(III)-sb is absent. This could indicate that the Co(III)-sb sterically hinders interchain hydrogen bonding, forcing the chains to be farther apart, and resulting in a decrease in β -sheet content.

In addition to the initial pentamer simulation with a single Co(III)-sb complex bound bidentate at His6 and His13 of each A β ₄₂ monomer within the pentamer, we also explored the effect of various equivalents of Co(III)-sb to A β ₄₂. The average number of residues in a β -sheet over the simulation time was calculated for 0.2, 0.4, 0.6, and 0.8 equivalents of Co(III)-sb corresponding to Co(III)-sb bound bidentate to 1, 2, 3, and 4 of the 5 chains in the pentamer respectively. The percent β -sheet for each equivalency was calculated and plotted in **Figure 3.8**. The data demonstrate sigmoidal dose dependence with low equivalents of Co(III)-sb having minimal effect on β -sheet content and high equivalents demonstrating saturation in reduction of β -sheet content. The largest drop in β -sheet content is achieved at doses between 0.4 and 0.8 equivalents Co(III)-sb.

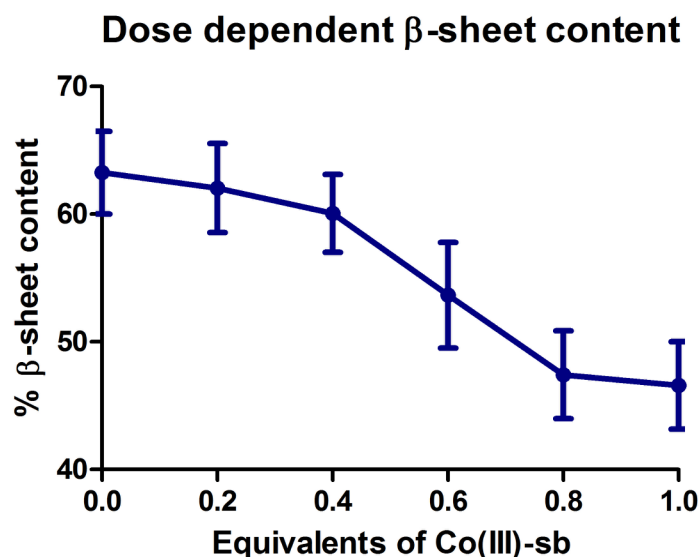


Figure 3.8: Percent β -sheet content over 100 ns simulation times for various equivalents of Co(III)-sb to $A\beta_{42}$ chains within the pentamer. Low equivalencies of Co(III)-sb have minimal effect, while at high equivalencies the reduction in β -sheet content by Co(III)-sb is saturated.

3.4.3 Experimental Aggregation Study

In order to compare the results of our monomeric and pentameric $A\beta_{42}$ simulations with experimental aggregation kinetics, we synthesized the Co(III)-sb with methylamine axial ligands, which was the structure used for parameterization of Co(III)-sb in the model. Following purification and characterization of this novel Co(III)-sb complex, we obtained a crystal structure. We then measured $A\beta_{42}$ aggregation kinetics using ThT fluorescence to follow the formation of β -sheet content over the course of aggregation. We treated monomerized $A\beta_{42}$ with three doses of Co(III)-sb (0.1, 0.3, and 0.5 equivalents) and observed dose-dependent inhibition of aggregation. 0.1 equivalent Co(III)-sb showed a modest decrease in aggregation, while 0.5 equivalents Co(III)-

sb showed almost complete inhibition of aggregation. In contrast, 0.5 equivalents of unmetallated acacen ligand did not inhibit aggregation compared to untreated $A\beta_{42}$.

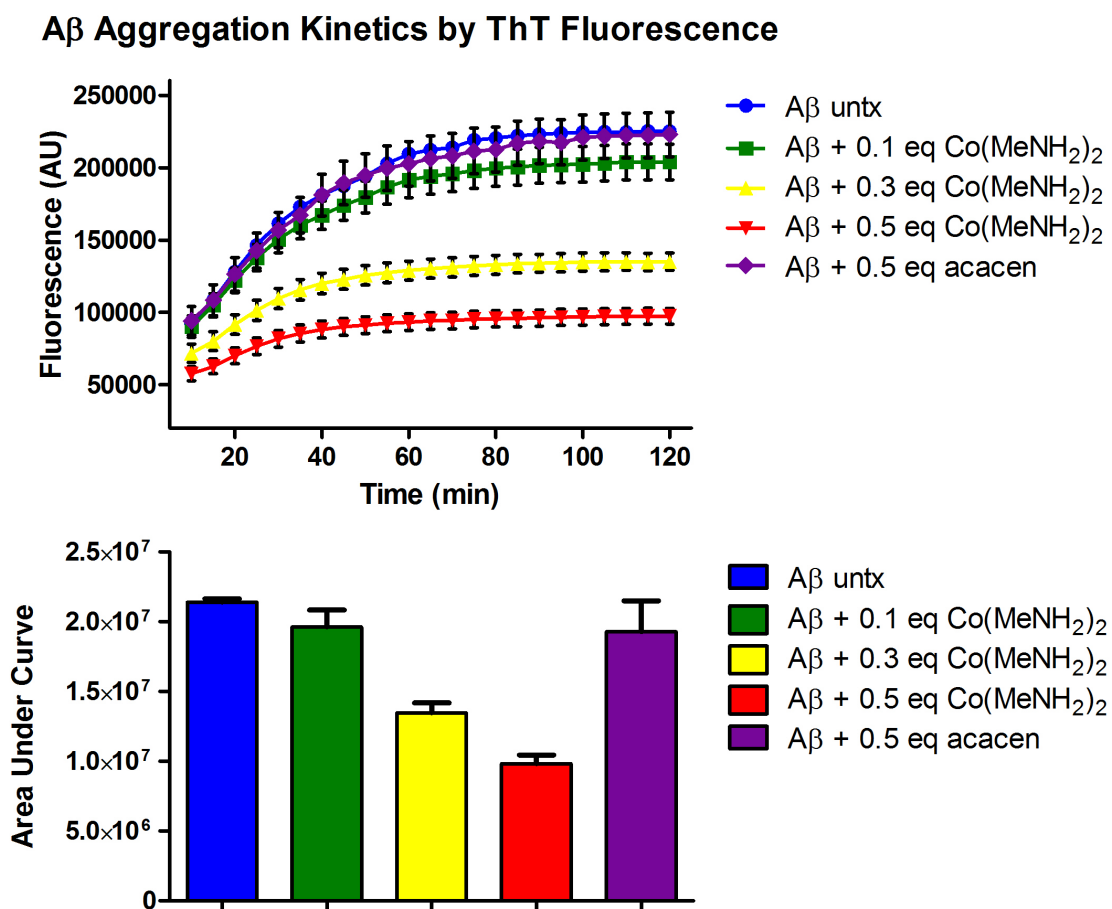


Figure 3.9: $A\beta_{42}$ aggregation inhibition as measured by Thioflavin T fluorescence. $Co(III)$ -sb demonstrates dose dependent inhibition of $A\beta_{42}$ aggregation, while unmetallated ligand acacen does not alter aggregation kinetics. Kinetic curves and AUC analysis are displayed as mean \pm SEM.

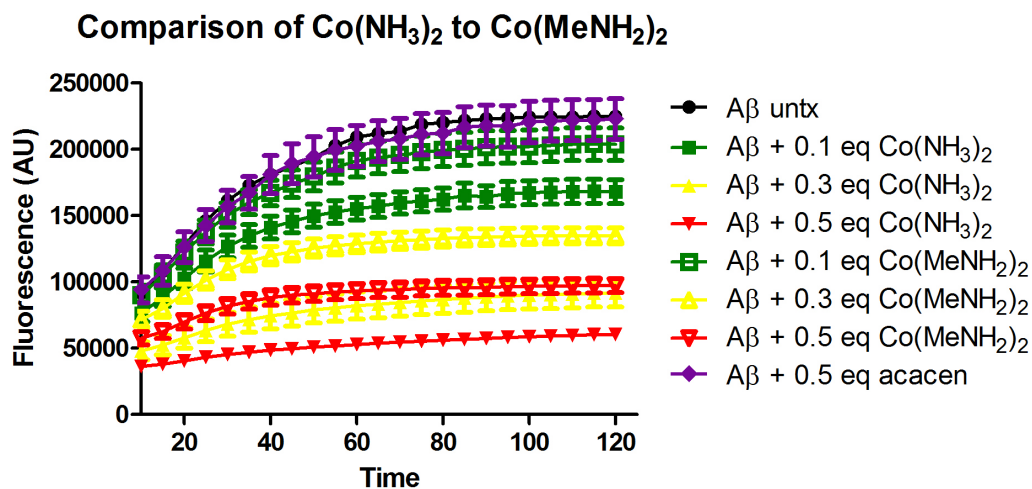


Figure 3.10: ThT fluorescence assay comparing the effects of equivalent doses of $\text{Co}(\text{MeNH}_2)_2$ (Chapter 3) vs. $\text{Co}(\text{NH}_3)_2$ (Chapter 2). $\text{Co}(\text{MeNH}_2)_2$ is a slightly worse amyloid aggregation inhibitor than $\text{Co}(\text{NH}_3)_2$ at each dose. This is likely due to electron donating character of the methylamine group compared to the bisamine ligands stabilizing the axial ligands.

3.5 Discussion

This study combined computational and experimental methods to explore the mechanism of $\text{Co}(\text{III})$ -sb inhibition of $\text{A}\beta$ aggregation. MD simulation of the effects of bound $\text{Co}(\text{III})$ -sb on monomeric $\text{A}\beta$ folding demonstrated reduction in β -sheet formation, decreased intermolecular hydrogen bonding between the N- and C-termini, and increased distance between residues. These effects are primarily due to the placement of $\text{Co}(\text{III})$ -sb bound bidentate between His6 and His13. The strong bond between the histidine residues and cobalt prevents $\text{A}\beta_{42}$ from freely interacting with itself and water. $\text{Co}(\text{III})$ -sb sterically hinders the $\text{A}\beta_{42}$ side chains from moving closer and making hydrogen bonds that would eventually result in β -sheets.

We should note here that β -sheet formation in the monomer is not necessarily indicative of β -sheet formation in fibrils and higher order aggregates. The β -sheets that hold the fibrils together form between individual $A\beta_{42}$ peptides that aggregate in solution. However, in order for a monomer to form aggregates, the monomer must have favorable interactions with other peptides in solution. In our simulation of $A\beta_{42}$ monomer only, we observe that the peptide adopts a folded conformation similar to that of the typical hairpin structure expected for $A\beta$ aggregates. Presence of β -hairpins in the monomer play a critical role in the growth of fibrils as monomers aggregate in solution to form β -sheets [174]. This β -hairpin conformation is stable in solution for ~ 140 ns. Therefore, we predict that this peptide can easily form aggregates under the correct conditions. On the other hand, when $Co(III)$ -sb is bound, $A\beta_{42}$ never adopts this folded conformation. The residues in this system are farther away from each other and the interaction is low. This causes the $A\beta_{42}$ to form stable helix structures. In this state, we expect the $A\beta_{42}$ to be less likely to aggregate and form fibrils.

The simulations of pentameric $A\beta$ oligomers demonstrate the ability of $Co(III)$ -sb to destabilize the hydrogen bonding required for amyloid aggregation. This is reflected in decreased hydrogen bonding, as well as increased distance between chains in the pentamer. The destabilization of β -sheets is primarily centered on residues 6 to 13 where the $Co(III)$ -sb complex is directly bound, with additional disruption seen between residues 27-30. When the equivalency of $Co(III)$ -sb to $A\beta$ within the pentamer is varied, we observed dose dependent inhibition with a maximal change in the percent β -sheets between 0.4 and 0.8 equivalents. Mechanistically this reveals that the destabilization caused by $Co(III)$ -sb coordination is sufficient to affect neighboring monomers within a larger aggregate.

Experimentally, we observe parallel dose-dependent β -sheet inhibition by ThT fluorescence at a much larger aggregation scale. Co(III)-sb has minimal effects at the lowest dose tested and near complete aggregation inhibition at the highest dose of 0.5 equivalents. Importantly, the negative control unmetallated ligand has no effect on aggregation, confirming the role of Co(III)-sb coordination for aggregation inhibition. The results of the pentamer simulation describe destabilization of preformed aggregates by Co(III)-sb coordination, while the results from the ThT aggregation assay demonstrate that Co(III)-sb binding can inhibit fibril formation. It is important to note that the simulation and experimental data target separate properties of the aggregates at disparate size scales. Neither technique is compatible with the aggregation timescale or size range of the other and so cannot provide experimental confirmation of the modeling results. However, the parallel equivalency measurements support an underlying property of Co(III)-sb coordination that is relevant at both scales and reinforces the validity of the simulation results. Employing both computational MD simulations and experimental aggregation data, this work illuminates the mechanisms for Co(III)-sb inhibition of β -sheet formation at the monomer, oligomer, and fibril scales, and demonstrates the potential utility of Co(III)-sb complexes as amyloid aggregation inhibitors.

3.6 Acknowledgements

This research was supported in part through the computational resources and staff contributions provided for the Quest high performance computing facility at Northwestern University which is jointly supported by the Office of the Provost, the Office for Research, and Northwestern University Information Technology. X-ray, MS, NMR work made use of the IMSERC at Northwestern University, which has received support from the Soft and Hybrid

Nanotechnology Experimental (SHyNE) Resource (NSF ECCS-1542205); the State of Illinois and International Institute for Nanotechnology (IIN).

3.7 Publication Information

Sections of this chapter are published with the following citation information:

Iscen A.*, Brue C.R.*, Roberts K.F.*, Kim J., Schatz G., Meade T.J. Inhibition of Amyloid-B Aggregation by Cobalt(III) Schiff Base Complexes: A Computational and Experimental Approach. *J. Am. Chem. Soc.* 2019, 141, 42, 16685 – 16695.

CHAPTER 4

Inhibition of Metal-Mediated Amyloid- β Toxicity with Cobalt(III) Schiff Base Complexes**4.1 Abstract**

The interaction of A β and endogenous metal ions has been widely implicated in ROS-mediated toxicity. Specifically, binding to redox active Cu(II) has been shown to increase neurotoxicity, while binding to redox inactive Zn(II) decreases neurotoxicity [39]. Because Co(III)-sb binds to A β at the same N-terminal His residues that form the endogenous metal binding site, we hypothesized that Co(III)-sb binding could displace endogenous metals, leading to reductions in ROS and toxicity. This chapter outlines a multimethodological approach to studying the effects of Co(III)-sb on metal binding and ROS production. Despite limited success identifying a specific ROS pathway that Co(III)-sb interacts with or ameliorates, we effectively demonstrated rescue of A β toxicity in culture by treatment with Co(III)-sb.

4.2 Introduction

Disruptions in metal binding are a common feature of many neurodegenerative proteinopathies. While significant evidence of metal disruption in AD has been demonstrated, direct observation of metal-A β interactions *in vivo* remains elusive [39]. Because the affinity of endogenous metals for A β is relatively low compared to other metal-binding proteins and the concentrations of free metals are tightly regulated and low, they would not be expected to interact under normal conditions in the cytosol or extracellular space. However, transient elevations in synaptic labile metal pools during signaling, as well as disrupted physiology with age or disease, could contribute to the aberrant association of endogenous metals with A β .

Because the affinity of metals for A β is relatively low and their binding alters the protein aggregation landscape, it has been difficult to measure accurate binding affinities. For example Cu(II) bound to A β can act both as a structural element favoring specific peptide conformations or as a catalytic center inducing the production of ROS [39]. As such, coordination to Cu(II) can change both aggregation and toxicity. The complexity of these effects often makes deciphering the role of Cu(II) binding to A β difficult.

Variations in methodology have led to published binding constants for Cu(II) to A β ranging across order of magnitude. Recent experiments using more robust methodologies suggest that the affinity is probably on the order of low nanomolar [51]. Zn(II) binding affinities for ZFTFs have also been reported in the low to mid nanomolar range [175]. While Co(III)-sb has been demonstrated to be able to displace Zn(II) from ZFTFs, no direct evidence of metal displacement from A β has yet been published.

Characterization of the interaction between A β and Cu(II) is especially important since it is believed to underlie the generation of ROS which contributes to the peptide's neurotoxicity [176]. By redox cycling in the presence of biological reducing agents such as ascorbate, Cu(II)-A β has been shown to produce ROS via Fenton and Haber-Weiss chemistry [4]. Coordination complexes targeting the N-terminal His residues have shown efficacy at decreasing the formation of ROS by Cu(II)-A β adducts [78].

While Cu(II)-binding is not thought to be exclusively responsible for A β cytotoxicity, it can be linked to many of the other pathologic mechanisms [57]. One of the primary proposed mechanisms for A β toxicity is via disruption of the lipid membrane [177, 178]. For example, it has been demonstrated that A β treatment *in vitro* increases membrane permeability and induces

pore formation [179, 180]. ROS are a major source of membrane damage due to lipid peroxidation [180].

Lipid peroxidation is generated by free radical capture of hydrogen from unsaturated carbons such as those found in unsaturated fatty acids within the lipid membrane. The unpaired electron on the fatty acid then captures oxygen, forming a peroxy radical. Peroxy radicals are unstable and decompose into a variety of compounds including reactive aldehydes 4-hydroxy-2-nonenal (HNE) and malondialdehyde (MDA), [181] which are elevated in AD brain [182, 183]. These aldehydes can diffuse away from their site of origin and propagate further oxidation by reacting with cellular nucleophiles such as DNA, proteins, and other lipids [184].

In addition to direct measurement of reactive oxygen species such as hydrogen peroxide or superoxide, redox environment can also be measured using cellular markers of oxidative stress. Assays measuring the presence of oxidized lipids or proteins in response to oxidative stress are often easier to perform and more robust than assays targeting ROS themselves. This chapter outlines the use of multiple assays to measure changes in ROS production by Cu(II)-A β .

4.3 Materials and Methods

4.3.1 A β Oligomer Preparation

A protocol for A β O formation was adapted from the Klein lab protocol [185]. Briefly, oligomers were prepared from premonomerized peptide film aliquots of Anaspec A β ₄₂ stored at -80 °C. 50 μ l of 20 mM NaOH was added to 0.1 mg of the peptide film in a sterile environment. Additionally, 10 μ l of dimethyl sulfoxide (DMSO) was added to facilitate solubilization. The sample was then sonicated for 10 seconds. The peptide was then diluted in to a final concentration

of 100 μ M in Ham's F12 and mixed for 10 seconds. This final solution was stored at 4 °C for 24 hours before use.

4.3.2 Cell Culture

Cell culture experiments utilized three cell lines: HT22 mouse hippocampal neurons (Millipore Sigma SCC129), HeLa human adenocarcinoma cells (ATCC® CCL-2™), and U87-MG human glioblastoma cells (ATCC® HTB-14™). HT22 cells were grown in DMEM media and U87-MG and HeLa cells were grown in EMEM media. In both cases, 500 ml base media was supplemented with 10% fetal bovine serum (FBS), 5 ml non-essential amino acids, 5 ml L-glutamine, and 5 ml sodium pyruvate. Cells were passaged at approximately 70% confluence using trypsin.

4.3.3 Peptide Synthesis

A β fragments and mutant fragments were synthesized for use in various binding assays using SPPS. These peptides were purified by HPLC and characterized by MS before use. A β ₁₆, as well as the triple His to Ala mutant were generated to better explore the binding of Co(III)-sb to A β .

4.3.4 Competitive Binding Studies

4.3.4.1 Dialysis

Dialysis was employed as a method of peptide sequestration for measurement of metal binding. For these assays, two 0.1 to 0.5 ml 3.5 kDa dialysis cassettes were rehydrated in a large beaker of 100 nM Co(III)-sb solution in PBS. 500 μ l of 100 nM A β was injected through the

cassette port into the inner dialysis chamber of one cassette. PBS was injected into the other cassette as a negative control. Both cassettes were suspended from floaties and allowed to dialyze in 100 nM Co(III)-sb covered in parafilm for 72 hours. Samples were withdrawn from each cassette and the outer fluid every 24 hours. Metal content of Cu, Zn, and Co was analyzed by ICP-MS.

4.3.4.2 Bead Binding Studies

Metal binding competition was also assessed using a bead-based protein sequestration approach. WT A β ₁₆ and the triple His > Ala mutant A β ₁₆ (A β _{16AAA}) were both conjugated to Pierce NHS-activated agarose beads. These were then used in a metal pull-down assay, where a change in the supernatant levels of Cu, Zn, and Co by ICP-MS was correlated to binding to A β . Briefly, the protein coated beads were added to solutions containing various concentrations of the metals and allowed to equilibrate. The samples were then centrifuged to pellet the beads and samples of the supernatant were collected for analysis.

4.3.5 ICP-MS

ICP-MS was broadly used to confirm metal concentrations in a variety of applications. Samples were prepped by combining 50 μ l sample with 100 μ l trace nitric acid for digestion. The final sample volume was diluted to 3 ml total with Millipore water. Samples were run for Cu, Zn, and Co on a Thermo iCAP Q ICP-MS with an injection volume of 2.5 ml.

4.3.6 CCA Fluorescence

The CCA assay is used to measure formation of hydroxyl radical [186]. This has often been applied to quantifying ROS production by A β -Cu(II). In this assay, 10 mM CCA is combined

with 10 μM $\text{A}\beta_{16}$, 10 μM Cu(II) from CuCl_2 , 300 μM ascorbate, and 20 μM Co(III)-sb in HEPES buffer with 1 μM EDTA. The components are mixed then plated in replicates on a microplate. Fluorescence was measured every 2 minutes at excitation 395 nm and emission 450 nm for 90 minutes on a Synergy H1M multimodal plate reader.

4.3.7 DCFDA Fluorescence

. Cells were plated in 48-well plates at 80,000 cells/well. DCFDA was prepared at 5 mM in DMSO and dosed into wells at a final concentration of 25 μM . Cells were incubated for 3 hours at 37 °C. Media containing DCFDA was removed and cells were dosed with oxidant at the desired concentrations. Hydrogen peroxide was used as a positive control. Media containing the dosing agents was removed after the desired time. For plate-based fluorescence, plates were imaged in brightfield mode and by fluorescence microscopy at excitation at 495 nm and emission at 529 nm.

For flow cytometry, all media was removed and the cells were trypsinized, transferred to Eppendorf tubes, pelleted, and resuspended in 0.5 ml 2% BSA solution. Flow cytometry was performed using a BD LSRII. DCFDA fluorescence was followed using the Alexafluor488 channel. Gating was set up as follows: P1 whole cells: FSC-A was plotted vs SSC-A, all cells were kept excluding the lower right corner. P2 singlets: FSC-H was plotted vs FSC-A, all cells on a linear slope were kept. P3 measure DCFDA fluorescence in the population of whole, singlet cells.

4.3.8 CellROX Flow Cytometry

This kit was purchased for measurement of ROS in cell culture by flow cytometry. Cells were plated in 48-well plates at 80,000 cells/well. After 24 hours cells were dosed at the desired

concentrations. TBHP was used as a positive control, and NAC was used as a negative control. Media containing the dosing agents was removed after the desired time. CellROX was diluted 2 μ l into 18 μ l DMSO and dosed into wells at 1 μ l / 500 μ l media. Cells were incubated for 15 minutes at 37 °C. 0.5 μ l SYTOX agent was added to the wells and the cells were incubated for an additional 15 minutes at 37 °C. All media was removed and the cells were trypsinized, transferred to Eppendorf tubes, pelleted, and resuspended in 0.5 ml 2% BSA solution. Flow cytometry was performed using a BD LSRII. CellROX fluorescence was followed using the Alexafluor488 channel and SYTOX fluorescence was followed using the APC channel.

Gating was set up as follows:

P1 whole cells: FSC-A was plotted vs SSC-A, all cells were kept excluding the lower right corner.

P2 singlets: FSC-H was plotted vs FSC-A, all cells on a linear slope were kept. P3 live cells: plot distribution over SYTOX channel: low signal is dead cells, keep all cells above a certain threshold.

P4 measure CellROX fluorescence in the population of whole, singlet, live cells.

4.3.9 MDA Assay

This assay was conducted using both U87-MG and HT22 cell lines according to the kit instructions. Briefly, cells were plated in a 6-well plate at a seeding density of 300,000 cells/well. 24 hours after plating, cells were dosed. After the desired dosage time, media was aspirated off and the cells were lifted by trypsinization. Cell suspensions were transferred to labeled Eppendorf tubes. The tubes were then centrifuged at 300 x g for 3 minutes for cell pelleting. The media was aspirated from each of the tubes and 300 μ l of MDA Lysis Buffer and 3 μ l BHT solution was added to each of the tubes. The tubes were then centrifuged at 13,000 x g for 10 minutes for cell lysis. 100 μ l of the lysate was collected into a separate tube.

MDA standards were prepared from a 0.1 M MDA starting solution. Standards for absorbance measurements were prepared at 0, 4, 8, 12, 16, and 20 nmoles/tube. Standards for fluorescence were diluted 10-fold and prepared at 0, 0.8, 1.2, 1.6, and 2.0 nmoles/tube. 300 μ l of 10 mg/ml TBA solution in 30% glacial acetic acid in water was added to each of the samples and standards. The solutions were heated in a water bath at 95 °C for one hour. Samples were then cooled to room temperature, plated in a 96 well plate at 60 μ l per well in triplicates. Fluorescence was measured at excitation 532 nm and emission 553 nm, and absorbance was measured at 532 nm on a Synergy H1M multimodal plate reader.

4.3.10 MTS Toxicity

Cellular viability was assessed using the CellTiter 96 AQueous One Solution Cell Proliferation Assay (Promega). Cells were plated in 96-well tissue culture treated plates at a density of 5,000 cells/well. Once cells had adhered, agents were dosed in replicate into the media at the desired concentrations. Viability was generally measure at 24 hours unless specified otherwise. After 24 hours, the media containing the agent was aspirated and replaced with 100 μ l fresh media. 20 μ l of 50% CellTiter solution in PBS was added to each well. Cells were incubated with the MTS reagent until signal was in the linear range (0.1 to 1 absorbance). 75 μ l of the media containing the MTS reagent was then transferred to a new plate (to avoid absorbance error caused by cells on the bottom of the plate). Absorbance was measured at 490 nm on a Synergy H1M plate reader.

4.4 Results

4.4.1 Studies of Competitive Metal Displacement

A primary assumption of our hypothesis about how Co(III)-sb alters the aggregation and toxicity of A β is its ability to competitively displace endogenous metals from the N-terminal His binding site. While this has been directly observed in other peptide systems such as ZFTFs, the evidence for this system is limited. ThT aggregation experiments demonstrated that the addition of 1 equivalent of Cu(II) to the aggregation mixture resulted in a 50% decrease in aggregation (Figure 4.1). This was accompanied by a drastic increase in the noise associated with the fluorescence measurements. Addition of 0.5 equivalents of Co(III)-sb resulted in complete inhibition of aggregation, indicating that although the Cu(II) was present in excess, the Co(III)-sb was able to interact sufficiently to alter the aggregation kinetics.

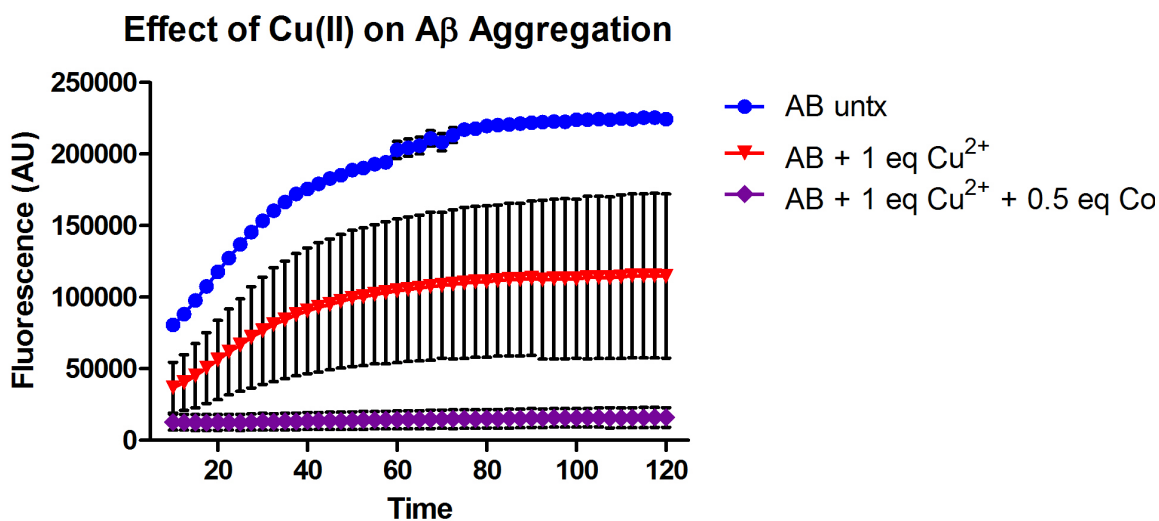


Figure 4.1: Effect of Cu(II) and Co(III)-sb on A β_{42} aggregation by ThT fluorescence.

In order to more directly investigate the ability of Co(III)-sb to displace metals from A β , we designed several experiments attempting to measure competition for His binding between Co(III)-sb and endogenous metal ions Cu(II) and Zn(II). This type of assay consisted of two components: 1) a method of isolating the protein-bound metals and 2) a method of accurately measuring the metal concentration. The second component was easily achieved using ICP-MS, which has several key advantages for measuring metal ion concentrations over other commonly used methods. The most important consideration is that the presence of these outside agents for measurement (such as fluorophores or chelators) often disrupts the binding equilibrium being measured. This is an especially relevant factor when attempting to measure competition between things with low binding affinity [187]. ICP-MS in contrast directly measures the metal content without an extraneous agent.

Several different strategies were employed for isolation of protein-bound metal. First a dialysis method was attempted, where A β_{42} was injected into the internal compartment of a dialysis cassette with a molecular weight cutoff that would not allow the protein to diffuse out of the cassette, but would allow free diffusion of metal ions and Co(III)-sb. A control cassette was injected with buffer only. Binding of the metals in solution to A β would have manifested as a concentration of metal ions in the inner compartment containing A β compared to the negative control.

No trends indicating preferential metal binding in the A β cassette over the negative control were observed (**Figure 4.2**). Differences between conditions were very small with the primary observation being that Co(III)-sb concentration increased steadily over time in all fractions due to evaporation of the dialysis liquid (**Figure 4.2a**). In addition, it was obvious from the high initial

readings at hour 0 and slow decline over time that the A β peptide was preloaded with relatively high levels of both Cu(II) and Zn(II) (**Figure 4.2b and c**).

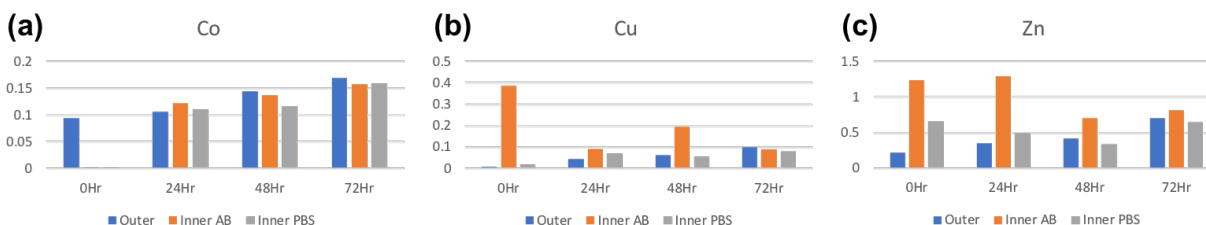


Figure 4.2: Metal binding by dialysis with ICP quantitation. (a) Co concentration, (b) Cu concentration, (c) Zn concentration.

In addition to this dialysis strategy, another method of protein isolation was attempted using conjugation of the N-terminal fragment A β ₁₆ to NHS-activated agarose beads. WT A β ₁₆ and mutant A β _{16AAA} (where all three His residues are changed to Ala residues) were coupled to the surface of the agarose beads. These were then allowed to equilibrate in mixtures of various metal concentrations. Following equilibration, the beads were spun down and the metal concentration in the supernatant measured by ICP-MS. Any decrease in the metal concentration could be attributed to metal binding to the protein on the beads. In addition to the mutated A β _{16AAA} we also used empty nonconjugated beads as a control. Preliminary studies did not yield significant difference between groups (data not shown), however this protocol can still be optimized to yield observable differences by changing the metal concentrations and the protein loading.

Coumarin-3-carboxylic acid (CCA) is commonly used to measure the production of hydroxyl radical in solution. CCA is initially nonfluorescent but upon hydroxylation gets converted to 7-OHCCA, which is fluorescent [186]. This methodology is often employed in the

testing of A β therapeutics meant to target metal binding, in particular chelating agents, which bind to the Cu(II) resulting in a decrease in hydroxyl radical formation and thus a decrease in CCA fluorescence. Initially this assay was tested as a way to measure decreases in ROS production in response to Co(III)-sb treatment.

CCA fluorescence showed that neither A β alone (**Figure 4.3, purple**) nor Co(III)-sb (**Figure 4.3, gray**) are redox active. Cu(II) alone in solution (**Figure 4.3, blue**) resulted in the highest production of hydroxyl radical. Addition of equimolar A β and Cu(II) resulted in production of free radical, but to a much lower extent than free Cu(II) (**Figure 4.3, black**). Treating A β :Cu(II) with Co(III)-sb revealed a trend opposite to what we anticipated, where increasing the dose of Co(III)-sb resulted in higher production of ROS. This is likely due to displacement of the Cu(II) from A β , thus increasing the free pool of Cu(II).

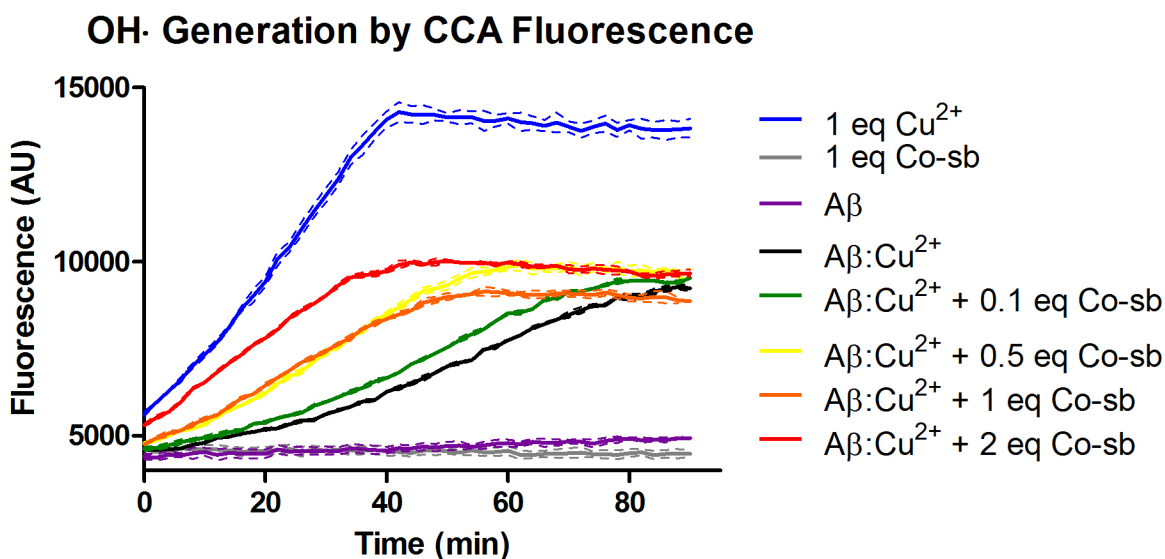


Figure 4.3: Metal displacement measured by CCA fluorescence. CCA becomes fluorescent upon hydroxylation. A β and Co(III)-sb alone are not redox active. Cu(II) alone exhibits the highest

ROS production. Addition of A β to Cu(II) decreases the ROS production compared to free Cu(II), but does show formation of hydroxyl radical. Addition of increasing doses of Co(III)-sb to A β :Cu(II) leads to increased ROS production, likely corresponding to displacement of the Cu(II) from A β by Co(III)-sb binding and overall increase in the free Cu(II) pool.

4.4.2 Studies on ROS Generation

Significant effort was spent attempting to measure changes in ROS in response to Co(III)-sb treatment. Our first approach was to use the cell-permeable ROS sensitive fluorophore DCFDA to measure changes in redox activity of the cells. Initial development involved dosing cells with various concentrations of oxidant such as hydrogen peroxide or TBHP and plate-based imaging using a fluorescence microscope. Qualitative changes in the DCFDA fluorescence with increased oxidant dose were observed but were not readily quantifiable. In order to expand quantification, we transitioned to using flow cytometry for fluorescence measurement.

While flow cytometry is more quantitative than microscopy, we encountered additional hurdles. For example, cell populations dosed with different amounts of oxidant did not separate well (**Figure 4.4**). Quantitation of average fluorescence for these populations can be seen in **Figure 4.5**. As the concentration of oxidant increased, a slight trend toward increased fluorescence was observed, however the groups did not separate well and are not statistically different. Given that the differences in oxidant dose between these groups was quite large and the small magnitude of expected changes due to Co(III)-sb treatment, this failure of the population to separate was very problematic.

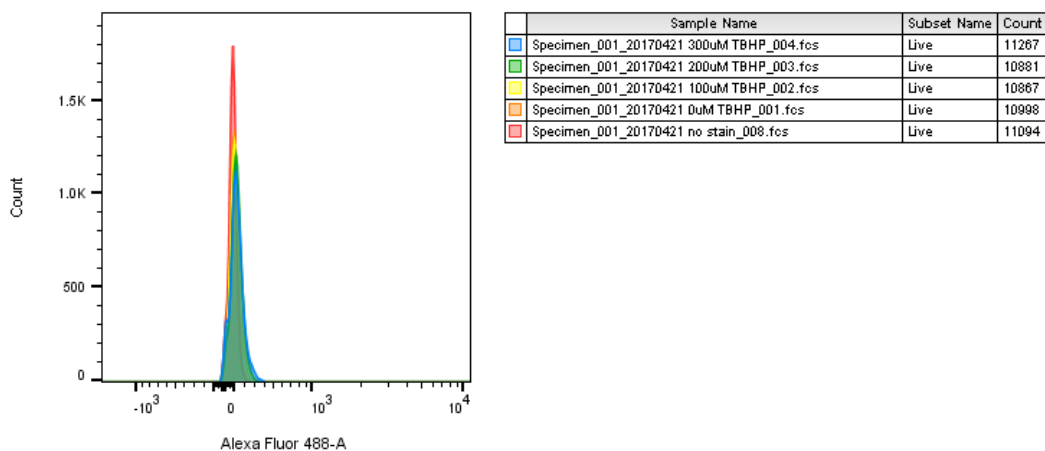


Figure 4.4: Flow cytometry distributions after treatment with TBHP measured by DCFDA fluorescence. As the concentration of oxidant increased, a slight shift toward increased fluorescence was observed, however the groups do not separate well. Red: unstained cells, orange: 0 μ M TBHP, yellow: 100 μ M TBHP, green: 200 μ M TBHP, and blue: 300 μ M TBHP.

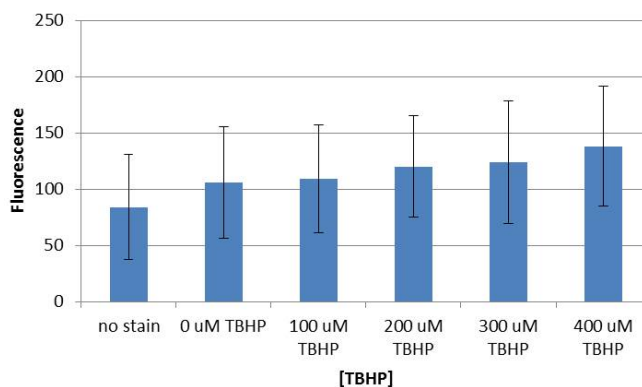


Figure 4.5: Average DCFDA fluorescence from flow cytometry distributions after treatment with TBHP. As the concentration of oxidant increased, a slight shift toward increased fluorescence was observed, however the groups do not separate well and are not statistically different.

Numerous optimization trials were conducted to improve the resolution of the DCFDA flow assay, but did not yield a viable protocol. When cells treated with various combinations of $A\beta$, Cu(II), and Co(III)-sb were tested, there were no observable trends and all conditions were within error of one another (**Figure 4.6**).

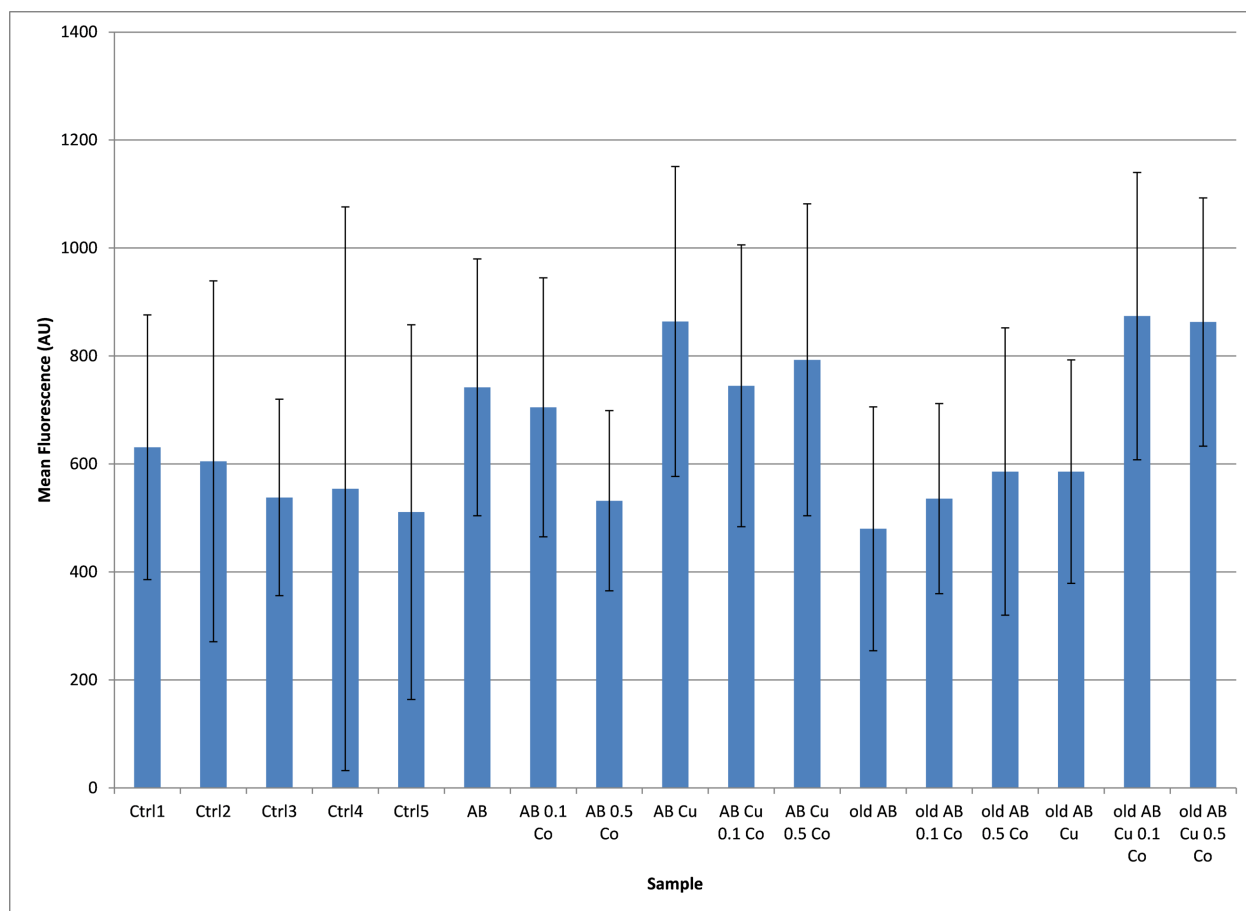


Figure 4.6: Average DCFDA fluorescence from flow cytometry distributions after treatment with $A\beta$, Cu(II), and Co(III)-sb. The conditions are not statistically different.

Given our proven difficulty using DCFDA fluorescence to measure ROS, as well as literature reports of its unreliability, we decided to use an alternative fluorescent probe to measure

changes in ROS by flow cytometry. We switched to a commercially available CellROX kit, which includes both a fluorescent probe for ROS called CellROX, as well as a cell viability probe called SYTOX. This kit was also tested using ROS induction by TBHP, and similarly failed to show significant differences between the groups despite relatively large differences in the oxidant dose (Figure 4.7).

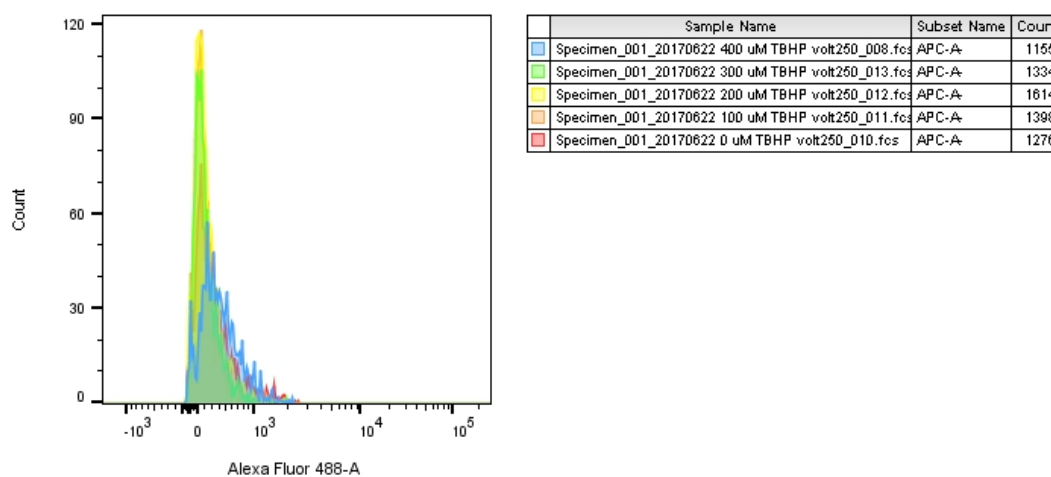


Figure 4.7: Flow cytometry distributions after treatment with TBHP measured by CellROX fluorescence. The groups do not separate well. Red: 0 μ M TBHP, orange: 100 μ M TBHP, yellow: 200 μ M TBHP, green: 300 μ M TBHP, and blue: 400 μ M TBHP.

Optimization included testing various concentrations of all relevant agents, using different cell lines, and contacting the company for technical support. However, despite all these manipulations, we were unable to observe any trends of note (Figure 4.8). This troubleshooting ultimately did not yield a successful method for measuring ROS by flow cytometry and this line of investigation was abandoned in favor of measuring cellular markers of oxidative stress.

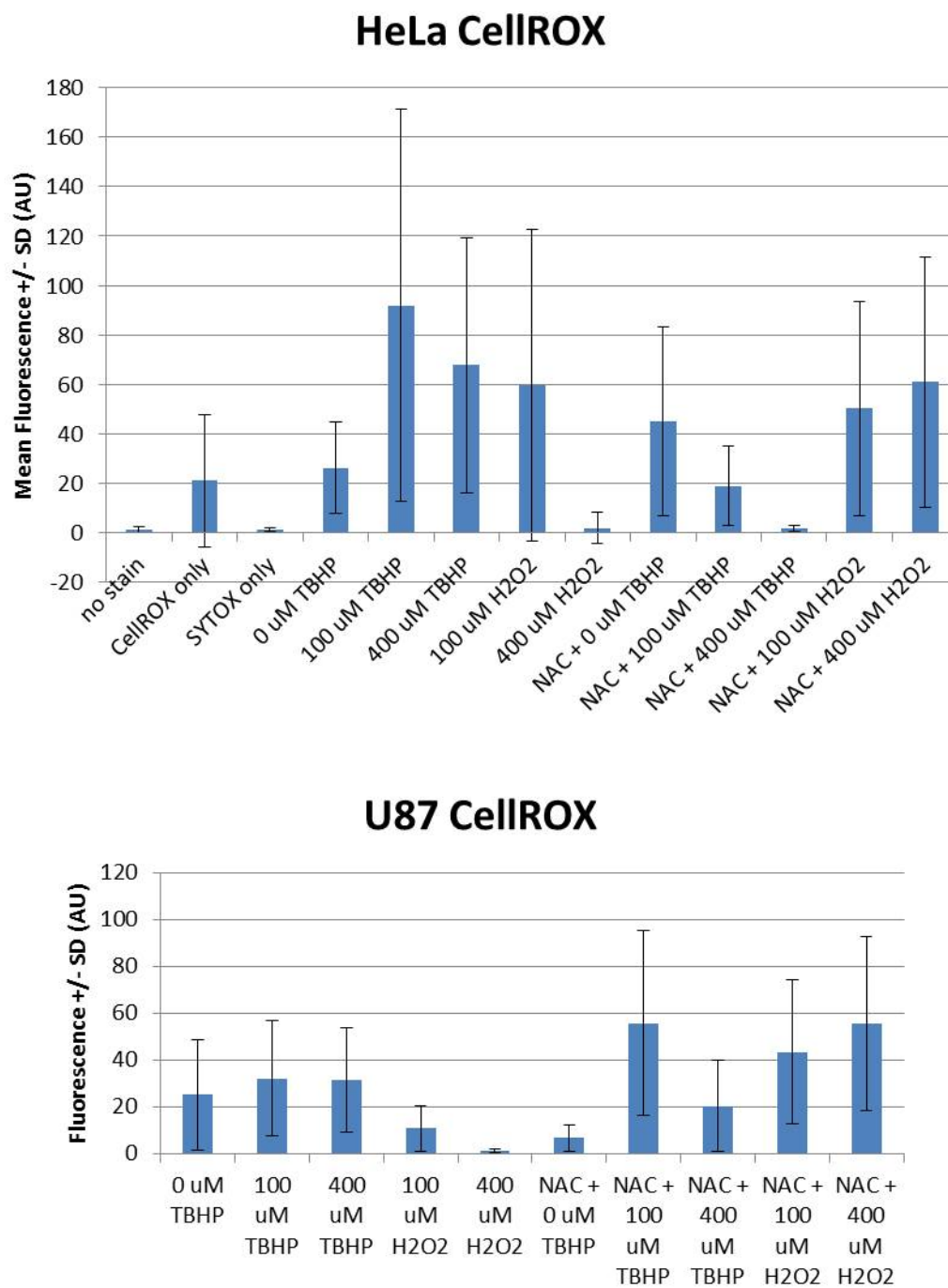


Figure 4.8: Average CellROX fluorescence from flow cytometry distributions after treatment with TBHP (oxidant) and NAC (antioxidant) in two different cell lines. The conditions are not statistically different.

Fearing that the reason we were unable to measure changes in ROS by flow cytometry was their transient nature, we switched to measuring a more stable marker of oxidative stress: malondialdehyde (MDA). MDA is a product of lipid peroxidation which is generated after exposure to ROS and is elevated in AD brains [188]. In this assay, cells are dosed then lysed. MDA in the sample is reacted with TBA to produce a colored byproduct that can be measured by either absorbance or fluorescence. A standard curve of known MDA concentration is generated for accurate quantitation.

While consistently linear standard curves demonstrated that the kit components were functional, we consistently observed very low signal from all cellular samples (always between the zero and first point on the standard curve). After dosing cells with A β O_s at various concentrations, we measured less MDA in samples that received A β O_s than in negative controls (**Figure 4.9**).

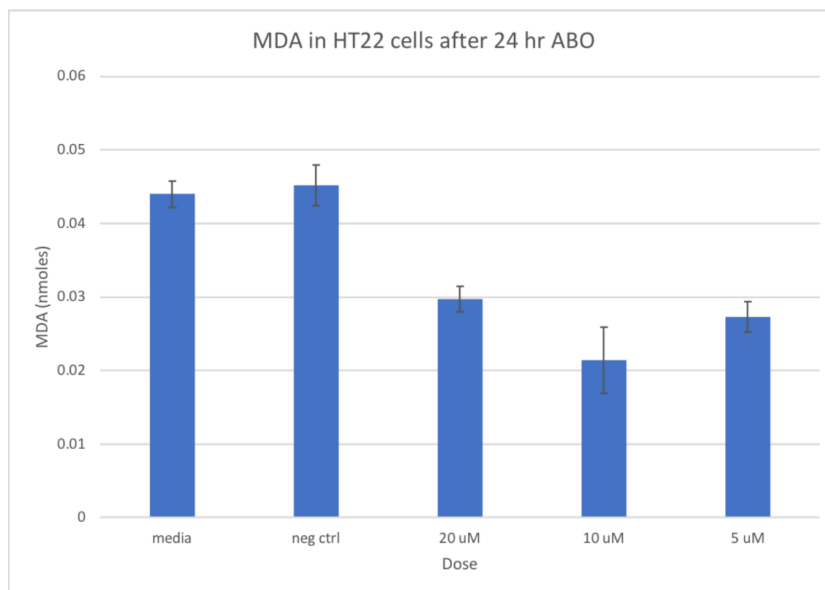


Figure 4.9: MDA concentration in cells following treatment with A β O_s. Negative controls show high levels of MDA than A β O_s-dosed cells. The absolute value of all conditions is very low.

4.4.3 Toxicity Studies

Because many things are known to affect A β aggregation, it is especially important to demonstrate a biological endpoint when developing an amyloid inhibitor. As such we utilized cell viability assays to explore the effects of Co(III)-sb on A β -mediated toxicity to cultured cells. We first demonstrated that Co(III)-sb itself is not toxic to cells at the concentrations used for aggregation inhibition (**Figure 4.10**).

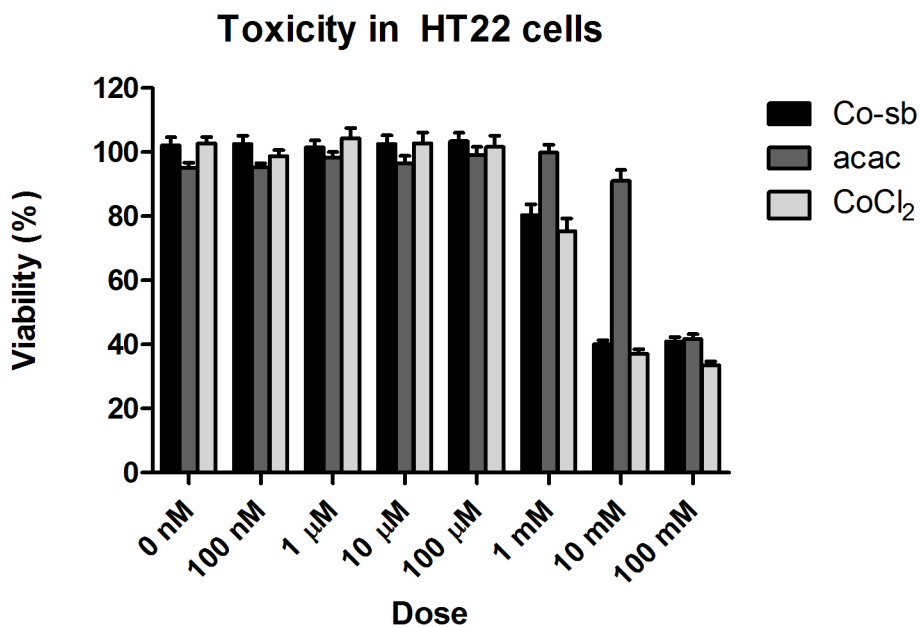


Figure 4.10: Toxicity of Co(III)-sb in HT22 cells by MTS assay. All three compounds show 100% viability at doses lower than 100 μ M. For reference, doses typically used for aggregation inhibition varied between 2.5 and 25 μ M.

We then demonstrated rescue of cellular A β toxicity with Co(III)-sb treatment (**Figure 4.11**). 0.5 equivalents of Co(III)-sb or acacen alone did not alter viability. Aggregated A β decreased cell viability to 70% of controls after 24 hours. A β aggregated in the presence of increased equivalents of Co(III)-sb showed increasing viability in a dose-dependent manner, while A β aggregated in the presence of the negative control acacen did not differ from untreated A β .

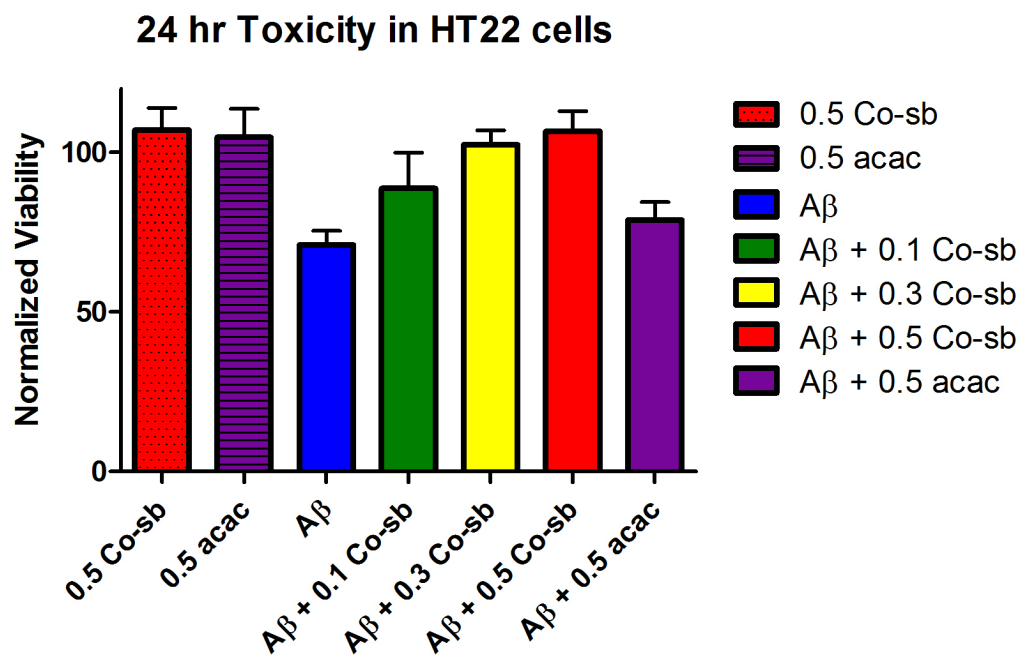


Figure 4.11: Rescue of A β toxicity by Co(III)-sb in HT22 cells by MTS assay. Treatment with Co(III)-sb reduced A β toxicity in a dose-dependent manner, while treatment with acacen had no effect. Data are normalized to the viability of vehicle treated controls and presented as mean \pm SEM.

4.5 Discussion

Attempts to directly measure metal competition for the N-terminal His residues of A β were not successful. However, these assays can still be further optimized to more accurately measure small changes in concentration. Indirect evidence from ThT aggregation inhibition in the presence of Cu(II), as well as the observed increases in ROS by CCA assay do offer some reassurance that Co(III)-sb is indeed capable of displacing Cu(II) from the N-terminal binding site of A β .

Although seemingly counterintuitive based on the premise of Co(III)-sb as an inhibitor of Cu(II)-A β mediated ROS, the CCA assay results are consistent with Co(III)-sb displacing Cu(II) from the A β binding site. Since free Cu(II) has the highest production, displacing it from A β actually leads to an increase in ROS. Unlike chelation agents that have demonstrated decreased ROS with this assay, our agent does not bind the metal, but rather targets the protein to prevent the interaction. In buffer, this results in an increase in free Cu(II) which manifests as higher ROS production. *In vivo*, this would not be the scenario since the free Cu(II) would likely be bound quickly and not remain labile.

Attempts to measure ROS in cells by flow cytometry were not successful and eventually abandoned in favor of measuring markers of oxidative stress in cells. Unfortunately, initial attempts to measure MDA also faced difficulty. This is likely caused by competing effects of A β on the cell. Because the assay measures MDA after lysis of living cells, MDA in dead cells is not factored into the measurement. As such the cells most heavily affected by oxidative damage are excluded from the measurement. If A β is causing significant cell death, the lower amount of MDA could be a reflection on a lower number of cells rather than indicating less oxidative stress. These hurdles could be overcome with further optimization to better characterize a subtoxic A β O dose.

Although we were unable to successfully measure changes in ROS or oxidative stress in response to Co(III)-sb treatment, we did observe convincing rescue of A β toxicity in cultured cells. This was a critical piece of the story, since many factors can affect amyloid aggregation without translating to biological benefits. While finding a way to study the effects of Co(III)-sb on metal binding and ROS is attractive given that this is the primary mechanism of action for other similar metal-targeted amyloid inhibitors, it may be that Co(III)-sb functions through an alternative mechanism completely. It has been demonstrated that coordination to the His residues alone can alter the structural properties of A β , without any effects of metal displacement. In addition, the effects on toxicity could be entirely attributable to changes in the aggregate populations with no role for ROS. As such, while success in these experiments would have been useful for identifying the mechanism of Co(III)-sb, it is not required for the viability of Co(III)-sb as an amyloid inhibitor.

4.6 Acknowledgements

We thank Keith MacRenaris and Becky Sponenburg from Northwestern's Quantitative Bio-element Imaging Center (QBIC) for running ICP-MS samples, and Keith MacRenaris from QBIC for help with confocal microscopy experiments.

This work was supported by the Northwestern University – Flow Cytometry Core Facility supported by Cancer Center Support Grant (NCI CA060553). Confocal microscopy was performed at the Northwestern University Quantitative Bio-element Imaging Center generously supported by the National Science Foundation CHE-9810378/005. Metal analysis was performed at the Northwestern University Quantitative Bio-element Imaging Center generously supported by NASA Ames Research Center NNA06CB93G.

4.7 Publication Information

Sections of this chapter will be published with the following citation information:

Roberts K.F., Brue C.R., Preston A.G., Baxter, D.N., Hertzog E., Varelas E., Heffern M.C., Roth E., Meade T.J. Inhibition of amyloid- β aggregation and toxicity by cobalt(III) Schiff base. (Submitted).

CHAPTER 5

**TEMarkers: Photoactivatable Contrast Agents to Investigate Synaptogenesis by
Transmission Electron Microscopy****5.1 Abstract**

Synaptic transmission facilitates communication between neurons and forms the basis for all neuronal signaling that underlies cognitive function. Yet despite the importance of synapses, the process of synaptogenesis remains poorly understood. Recent advances have made it possible for scientists to induce dendritic spine formation using two-photon uncaging of glutamate. However, subsequent study of the ultrastructure of newly formed synapses by transmission electron microscopy (TEM) remains difficult due to an inability to locate the induced synapses when switching between imaging modalities. Toward this end, we have designed small perfluorocarbon containing photoactivatable peptides (TEMarkers). TEMarkers consist of two charged amino acids coupled to a photocleavable group coupled to a perfluorocarbon tail. Upon activation, the perfluorocarbon tail is liberated and becomes insoluble forming an electrodense fluorine aggregate that provides contrast by transmission electron microscopy. As such, TEMarkers can be used as a road map to identify newly induced dendritic spines. Here we describe the synthesis and characterization of TEMarkers agents, as well as their use in an enrobed cell tissue model.

5.2 Introduction

Synaptic connections form the chemical and electrical link between neurons and underlie all neuronal communication. Many synapses are housed in dendritic spines, membranous protrusions that house the electrical and biochemical signaling machinery of the synapse. It has

been proposed that the growth and retraction of dendritic spines could play a role in experience - driven circuit changes during development and learning [189]. Yet despite the importance of synapse formation in neurobiology, the early development and evolution of synapses remains poorly characterized [190, 191]. For example, the precise mechanism by which neurons decide to form a synapse is widely debated. Some argue for molecular targeting mediated by expression of specific proteins on the cell surface that signal that a connection should be formed. Others emphasize the importance of neurotransmitter release for the attraction of synaptic binding partners. In addition to uncertainty about the mechanisms of synapse formation, the timeline of synapse development is also widely debated with estimates ranging orders of magnitude [189, 191].

Much of the work investigating early synaptogenesis has relied on the ability to induce *de novo* synaptogenesis via photocaged-neurotransmitters [191]. Photochemical control of a molecule is achieved by making an active biological molecule inactive through chemical modification via conjugation to a caging group. Irradiation via two-photon confocal microscopy breaks the bond to the caging group, releasing a small local amount of the active neurotransmitter ($\sim 1 \mu\text{m}^3$), and allowing it to perform its biological function in a photoactivatable manner. This technique gives researchers the opportunity to examine specific biological processes with tremendous specificity and precision [190, 191].

Glutamate is an excitatory neurotransmitter that is essential for understanding synaptic communication between neurons. Using two-photon microscopy, photocaged glutamate (MNI-L-glutamate) can be locally uncaged with high spatial precision near a neuronal process resulting in the rapid formation of a new dendritic spine [191]. Transmission electron microscopy (TEM) can then be used to investigate the ultrastructure of the early protosynapse, providing valuable insight

into the process of synaptogenesis [191]. However, there is currently no easy method for marking the newly induced synapse, so it is very difficult to find the region of interest when switching between confocal microscopy and TEM.

Current strategies employ the compound diaminobenzidine (DAB), which can be photo-oxidized to form a polymer used for marking neurons [190, 192]. Later when the tissue undergoes heavy metal staining for TEM using osmium tetroxide, the DAB polymer will stain darkly creating a marker for the point of photo-oxidation. Recently a variation of this strategy was employed by Roger Tsien's group to create color TEM images [193, 194]. Using versions of DAB tagged with various different heavy metals they induced localization and oxidation by a number of strategies, polymerizing the various labeled DAB complexes in different subcellular compartments. Then using energy dispersive x-ray (EDX) analysis of elemental composition, they were able to identify the various heavy metals and assign each a different color [193, 194].

Despite these recent modifications to DAB as a tissue marker for TEM, there are still a number of important drawbacks to relying on DAB polymerization for feature identification. Primarily, DAB is toxic to cells. Because it is critical that the marking agent be dissolved in the fluid at the time of synapse induction, it is important that the agent not affect the health of the cell or its ability to form synapses. In addition, DAB shows inefficient focal photoconversion. Finally DAB does not have any inherent contrast, but relies on increased uptake of the heavy metal contrast agent osmium tetroxide, which itself can introduce artifact into the images. As such, a superior marker agent would be non-toxic in solution, efficiently photocleave and aggregate upon photooxidation, and provide inherent contrast by TEM without the use of additional stains.

In TEM, contrast is created via interaction of the electron beam with electron dense material on the grid. Often in order to see biological materials made primarily of carbon, nitrogen,

oxygen, and hydrogen, they must be stained with heavy metals like osmium, uranium, lead, or gold. In a 2015 study, Sonzini et al. introduced the concept of using fluorine to provide TEM contrast by incorporating a small fluorinated moiety onto the N-terminus of the peptide sequence of A β ₁₆₋₂₃ (the core fibrillogenic sequence of A β ₄₂) [195]. After confirming that incorporation of the fluorinated moiety did not significantly alter aggregation kinetics (ThT fluorescence and CD spectroscopy) or morphology (AFM), the authors compared the TEM images of WT A β ₁₆₋₂₃ stained with uranyl acetate to unstained F-A β ₁₆₋₂₃. The fluorinated A β was easily visualized without staining once aggregated into amyloid fibrils due to dense packing of the fluorine in the amyloid aggregates. Contrast and resolution were both superior in the fluorinated A β aggregates compared to the uranyl acetate stained WT A β aggregates [195].

Leveraging this ability of electron dense fluorine to provide contrast by TEM and our groups previous experience designing responsive peptide amphiphiles, our group designed TEMarkers [196, 197]. The initial agent was designed by Adam Preslar and based on a peptide amphiphile structure that includes two charged lysine residues, a photocleavable amino acid, and a perfluorocarbon tail. The charged amino acids on one end are water soluble and ensure that the highly hydrophobic perfluorocarbon tail remains in solution as long as the structure is intact. Upon photocleavage, the perfluorocarbon tail is liberated and aggregates to form an electron rich TEM dye. In order to demonstrate proof of principle, our first agent incorporated a nitrobenzyl photocleavable group which cleaves under UV light for ease of characterization.

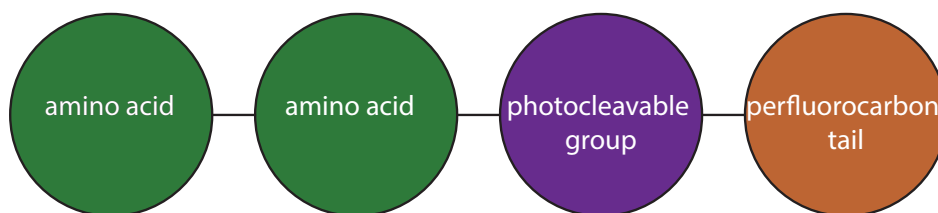


Figure 5.1: TEMarker schematic. The charged amino acids maintain solubility of the hydrophobic perfluorocarbon tail until the photocleavable group is cleaved, thus releasing the tail and allowing it to aggregate into an electron dense material. By using SPPS to generate TEMarkers, the synthesis is highly modular and allows easy interchange of the various components.

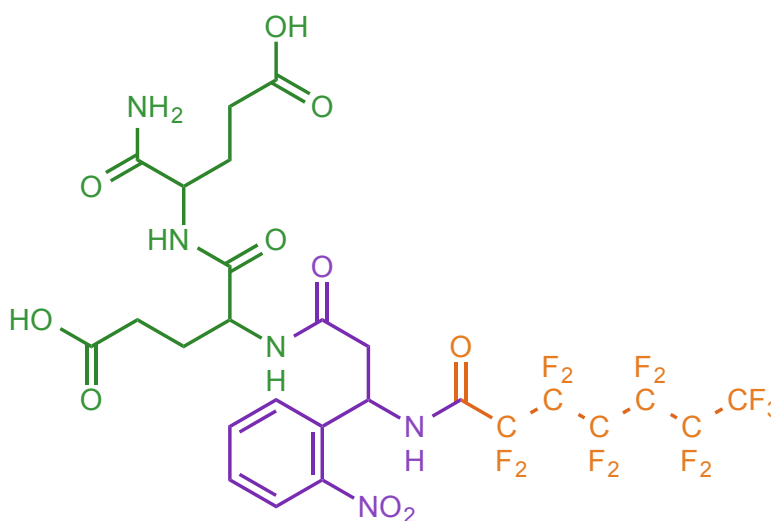


Figure 5.2: First-generation TEMarker chemical structure. This agent uses a nitrobenzyl photocleavable group which cleaves under UV light for easy characterization. Actual TEMarkers used for tissue labeling will be red-shifted for cleavage by two-photon excitation.

5.3 Materials and Methods

5.3.1 First-Generation Agent Synthesis and Characterization

Synthesis of the TEMarker agents was completed via hand coupling by SPPS in a 100 ml glass peptide synthesis flask (**Figure 5.3**). Agents were synthesized on Rink amide resin. Each step of the synthesis was checked using the Kaiser test for free amines. Briefly, 1 drop KCN in pyridine, 1 drop phenol in ethanol, and 1 drop ninhydrin in ethanol were combined with a tiny amount of the resin in a microcentrifuge tube. The tube was heated in sand at 100 °C for 3 minutes. Yellow/brown color was read as negative for free amines. Blue/black was read as positive for free amines.

The resin (0.25 mmol) was swollen in 25 ml in dry DCM for 15 min. DCM was removed through the stopcock by vacuum filtration and 25 ml 20% piperidine in DCM was added to Fmoc deprotect the resin. The peptide coupling flask was agitated for 10 minutes on a rotary shaker. Deprotection was confirmed via Kaiser test. Lysine Fmoc protected at the N terminus and BOC protected at the R group amine (1 mmol) was combined with HBTU (0.95 mmol) in minimal DCM to dissolve. A small amount of the DMF was added because HBTU was not soluble in DCM alone. Using a syringe, 300 µl of DIPEA was added to the Lys / HBTU mixture and activated for 10 minutes.

After 10 minutes of deprotection, the 20% piperidine solution was removed by vacuum filtration and the resin was washed four times with DCM. Kaiser test demonstrated positive free amines. The activated Lys mixture was added to the resin and allowed to couple for two hours (or until Kaiser test is negative) under agitation. After complete coupling the remaining Lys was removed, the resin washed and Fmoc deprotected as described above, and a second equivalent of Lys was coupled.

Following successful addition of the two lysine residues, we adapted the synthesis for the nitrobenzyl modified amino acid. Addition of the Lys residues utilized a small amount of DMF for solubilization of the HBTU, however we observed that the photocleavable group rapidly degrades in DMF. As such, we replaced the coupling reagent HBTU with PyBOP, which did not require DMF for solubility. In addition, we washed extensively with DCM between additions to ensure no residual DMF in the resin.

The final addition involved deprotection as above, then addition of the perfluorocarbon tail, tridecafluoroheptanoyl chloride (0.5 mmol). 111 μ l of the tail was combined with 2 ml dry TEA in 25 ml dry chloroform and added to the resin. The mixture was allowed to couple for 2 hours at room temperature in the rotary shaker. Following coupling confirmation by negative Kaiser test, the excess tail was removed and the resin washed four times with DCM. Next a small fraction of the resin was test cleaved and inspected for the full product by MALDI using 10 mg/ml CHCA as the matrix. Cleavage and deprotection of side chains was completed via the addition of TFA before dilution in water. Characterization of the final product was performed by NMR and MS.

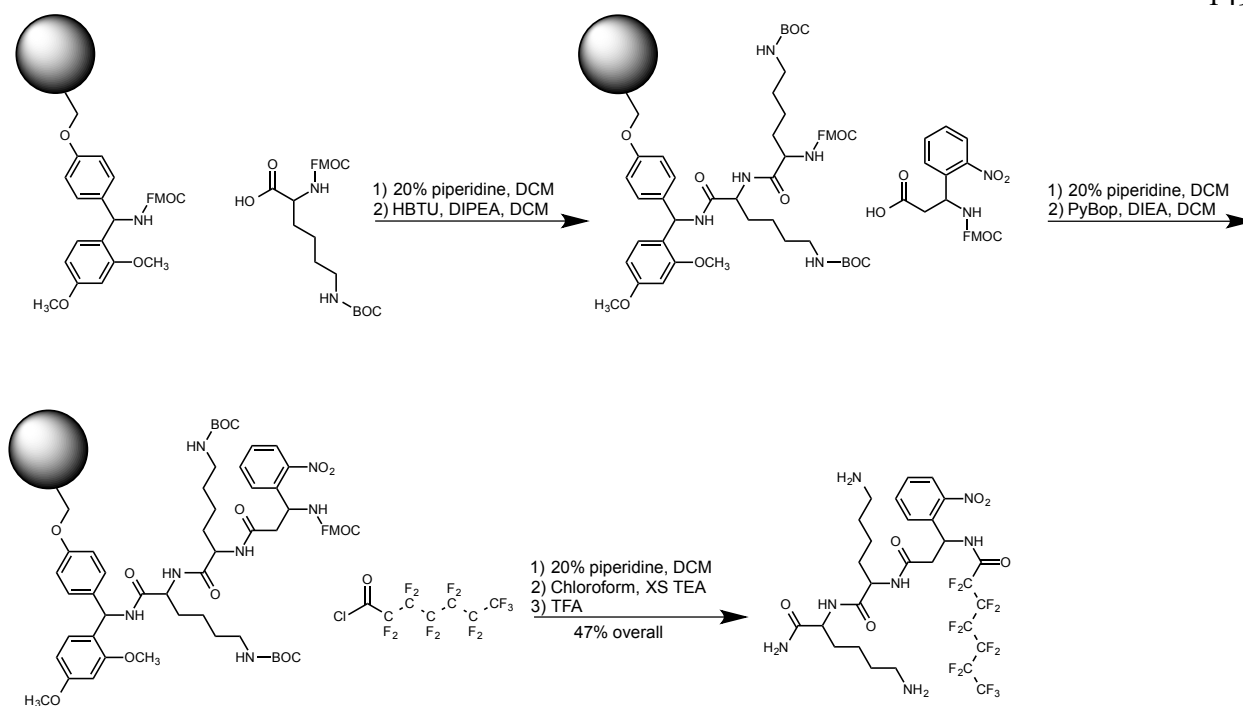


Figure 5.3: SPPS of first-generation TEMarker agent. Synthesis involves sequential deprotection and coupling of two lysine residues, a nitrobenzyl modified photocleavable amino acid group, and a perfluorocarbon tail. The complex is cleaved from the SPPS resin to a final yield of 47%.

5.3.2 Transmission Electron Microscopy

For standard on-grid UV activation studies, TEMarker solutions were prepared at 1 mg/ml in Millipore water and diluted to desired concentrations. 10 μ l of TEMarker solution was spotted onto Cu grids (Electron Microscopy Sciences). Grids were then activated under direct UV light at 365 nm for 5 minutes using a handheld UV lamp. Control grids were kept in the dark for the same amount of time. Excess solution was wicked off using filter paper and the grids were allowed to dry for 24 hours before imaging on a JEOL 1230 TEM operated at 100 kV. Images were processed using ImageJ.

For localization studies on the second-generation TEMarker agents, solutions were spotted onto London Finder Cu grids (Electron Microscopy Sciences). Activation was performed by placing London Finder Grids on glass coverslip plates. Plates were imaged by confocal microscopy on a Zeiss 510 LSM Inverted Confocal Microscope. Specific grid locations were selected in brightfield mode, then the agent was locally activated by two-photon excitation at 800 nm for the desired activation time (**Figure 5.4**). Following activation, excess solution was wicked off using filter paper. Grids were dried overnight and imaged on a JEOL 1230 TEM operated at 100 kV. Images were processed using ImageJ.

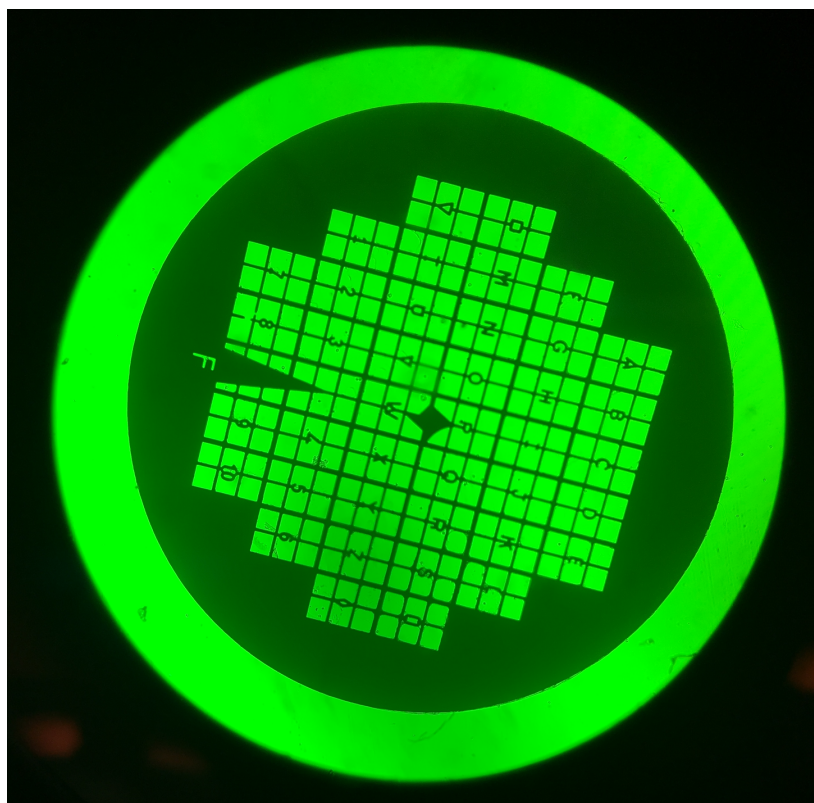


Figure 5.4: London Finder grid by brightfield microscopy showing alpha numeric positional markers. For localized activation studies, a specific region was selected for activation to study spatial precision of activation.

5.3.3 Nile Red CMC Assay

Nile Red (Sigma) was weighed out and resuspended in ethanol to a final concentration of 1.5 mM. TEMarker agents were resuspended at 1 mM in PBS and serially diluted downward to 500 μ M, 250 μ M, 125 μ M, 63 μ M, 31 μ M, 16 μ M, 8 μ M, and 4 μ M. Agents were plated in a 96 well plate at 100 μ l per well in triplicate. 10 μ l Nile Red in ethanol was added to each well. Solutions were left at room temperature for 15 minutes than mixed on a shaker for 15 minutes. After mixing, fluorescence was read at excitation 550 nm and emission 635 nm on a Synergy H1M plate reader.

5.3.4 UV-Vis Spectroscopy

Lyophilized TEMarker agent was resuspended in Millipore water. 300 μ l was transferred to a 1 mm quartz cuvette. The solution was wrapped in aluminum foil to prevent unwanted activation. The UV-Vis was blanked to water and an initial UV-Vis spectrum from 200 to 800 nm was obtained on a Agilent Cary 5000 UV-Vis-NIR spectrometer. After scanning, the solution was photoactivated under hand held UV lamp at 365 nm for 1 minute before being rescanned by UV-Vis. This was repeated for a total of 10 minutes of UV activation with scans at one minute intervals until we observed saturation of the changes in the UV-Vis spectrum.

5.3.5 Cell Culture

Cell culture experiments utilized two cell lines: HT22 mouse hippocampal neurons (Millipore Sigma SCC129) and U87-MG human glioblastoma cells (ATCC® HTB-14™). HT22 cells were grown in DMEM media and U87-MG cells were grown in EMEM media. In both cases,

500 ml base media was supplemented with 10% fetal bovine serum (FBS), 5 ml non-essential amino acids, 5 ml L-glutamine, and 5 ml sodium pyruvate. Cells were passaged at approximately 70% confluence using trypsin.

For localization studies, London Finder grids were coated in polylysine to improve cell adherence. Polylysine was diluted in sterile water at 1 mg/ml and spotted onto the shiny side of grids at 10 μ l per grid. Grids were allowed to sit for 5 minutes before the solution was aspirated. Grids were washed three times with sterile water to remove residual polylysine and allowed to dry in 6 well plates before use.

5.3.6 Agarose Enrobing Procedure

Cellular agarose noodles were prepared as a tissue model system for TEM imaging with help from Charlene Wilke in BIF. Cultured cells were trypsinized, aliquoted into separate tubes for each condition, and pelleted. 2% low melt agarose in water was prepared in a hot water bath and an ice bath for rapid cooling was set up. Approximately 7-15 μ l low temperature agarose was drawn up from the heated agarose solution using a Pasteur pipette and added to the cell pellets. These solutions were then carefully pipetted up and down to mix without introducing air bubbles. A volume of the agarose cell suspension was drawn up using the Pasteur pipette and allowed to cool slightly in the pipette tip. The pipette was then submerged in ice cooled PBS containing the TEMarker agent and the agarose noodle ejected from tip producing cells suspended in an agarose matrix. Careful handling to ensure that the noodle did not completely solidify within the glass pipette was required. Several noodles were prepared and stored in PBS with agent.

For two-photon activation, noodles were transferred to glass plates. Laser activation was performed along the long axis of the noodles with amplitude set at 10% on a 1 watt laser at 750

nm using a Zeiss 510 LSM Inverted Confocal Microscope with a Spectra Physics Mai Tai DeepSee 2-Photon Laser. The line down the long axis of the noodle was drawn by manually moving the stage since this microscope did not have a motorized stage. Following activation, the noodles were brought to Charlene Wilke for fixation.

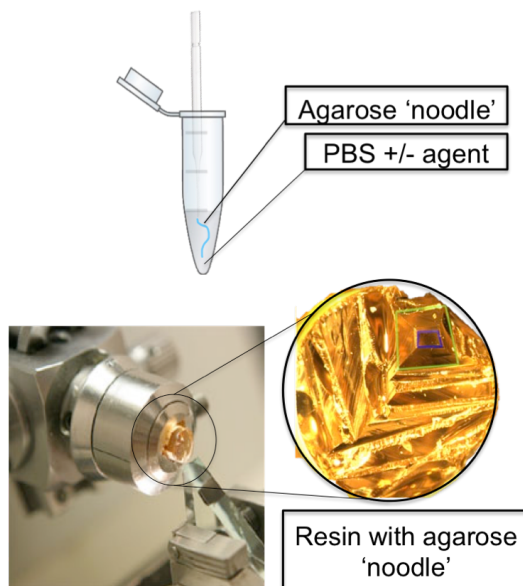


Figure 5.5: Schematic of agarose enrobing protocol to form cell suspension in agarose matrix as a tissue model for TEM imaging. Cells were resuspended in agarose, extruded into cold PBS, activated by confocal microscopy, fixed, embedded in resin, sectioned, and mounted to grids for TEM imaging.

Primary fixation of the cellular agarose noodles involved suspension in Karnovsky fixative (2% paraformaldehyde, 2.5% glutaraldehyde, in 100 mM PBS) for 2 hours at room temperature. After primary fixation the noodles were rinsed three times with buffer before being heavy metal stained in 2% osmium tetroxide for 2 hours at room temperature. The osmium tetroxide solution was removed and the noodles were washed three times with buffer. Next, the cells were

dehydrated by incubation in increasingly concentrated ethanol solutions (50%, 70%, 80%, 90%, and 100%) for 10 minutes each. Following dehydration the cells were infiltrated using increasing concentration of epoxy resin in ethanol (3:1 ethanol:resin, 2:1, 1:1, 100% resin, 100% resin) for 1 hour each at 50 °C. Once transferred to 100% resin, the noodles were embedded in capsules and allowed to polymerize overnight at 70 °C. Once hardened, the resin infiltrated noodles were sectioned via microtome to 50 µm thin sections which were subsequently mounted to Cu TEM grids for imaging.

5.3.7 MTS Toxicity

Cellular viability was assessed using the CellTiter 96 AQueous One Solution Cell Proliferation Assay (Promega). Cells were plated in 96 well tissue culture treated plates at a density of 5,000 cells/well. Once cells had adhered, agents were dosed in replicate into the media at the desired concentrations. Viability was generally measure at 24 hours unless specified otherwise. After 24 hours, the media containing the agent was aspirated and replaced with 100 µl fresh media. 20 µl of 50% CellTiter solution in PBS was added to each well. Cells were incubated with the MTS reagent until signal was in the linear range (0.1 to 1 absorbance). 75 µl of the media containing the MTS reagent was then transferred to a new plate (to avoid absorbance error caused by cells on the bottom of the plate). Absorbance was measured at 490 nm on a Synergy H1M plate reader.

5.3.8 Second-Generation Agents Synthesis and Characterization

Following successful activation of our first generation nitrobenzyl TEMarker, we sought to expand our library of agents and produce red-shifted TEMarkers compatible with activation by

two-photon excitation. Toward this goal, four new agents were synthesized by chemists in the lab Hao Li and Chris Brue (**Figure 5.6**). The synthesis of these agents is beyond the scope of this thesis, but their characterization by TEM is described below. All agents were synthesized, aliquoted, lyophilized, and stored at $-80\text{ }^{\circ}\text{C}$ until use.

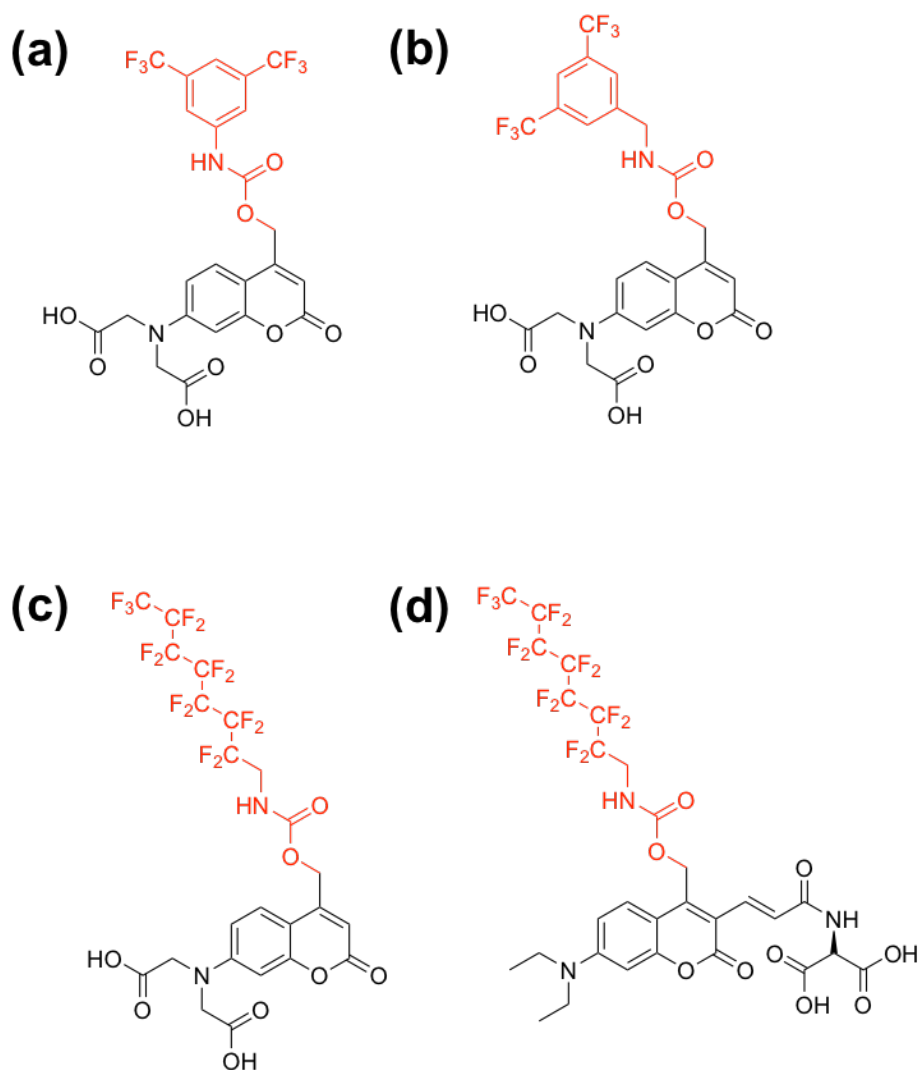


Figure 5.6: Four second generation red-shifted TEMarker agents. These agents replace the nitrobenzyl photocleavable group with coumarin derivatives that have two-photon excitation in the near IR region. Agents (c) and (d) employ the same perfluorocarbon tail used in the generation

one agent for contrast. Agents (a) and (b) instead use perfluorinated benzene derivatives to generate contrast.

5.4 Results

5.4.1 First-generation Agent Characterization

The premise of TEMarkers agents is the solubilization of a highly hydrophobic perfluorocarbon moiety via conjugation to a charged hydrophilic group. Upon photocleavage, the perfluorocarbon would no longer remain soluble and aggregate rapidly into an electron dense material that would provide contrast when viewed by TEM (**Figure 5.7**). Selective photoactivation of this agent could thus be used as marker in tissues to highlight areas where photoactivation occurred, making localization by TEM facile. This tool would have special utility in the field of neurobiology where two-photon uncaging of neurotransmitters is often utilized for induction of synaptogenesis. Ideally, a TEMarker agent would simultaneously photoactivate at the location of uncaging and rapidly aggregate with focal precision, producing a dark aggregate that could be used as a roadmap to newly induced synapses.

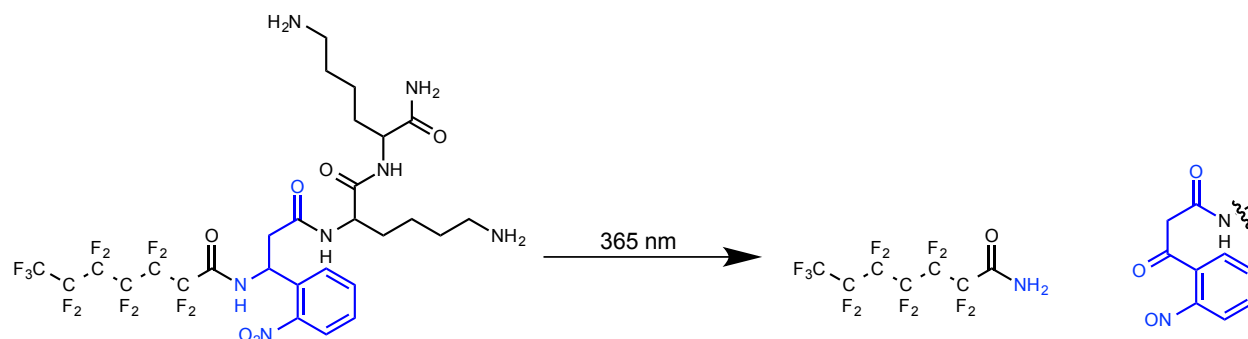


Figure 5.7: Schematic of UV photocleavage of the first generation TEMarker agent. Upon excitation at 365 nm, the nitrobenzyl group will cleave liberating the perfluorocarbon tail. This will then aggregate to form an electron dense material visible by TEM.

The first step in testing our design of the TEMarker agent was to ensure that the aggregated perfluorocarbon tail would indeed have enough electron density to be viewable by TEM. To test this assumption, we synthesized an analog of the perfluorocarbon tail released upon photoactivation by reacting tridecafluoroheptanoyl chloride with isopropylamine. This reaction rapidly yielded a near solid substance that had significant contrast by TEM.

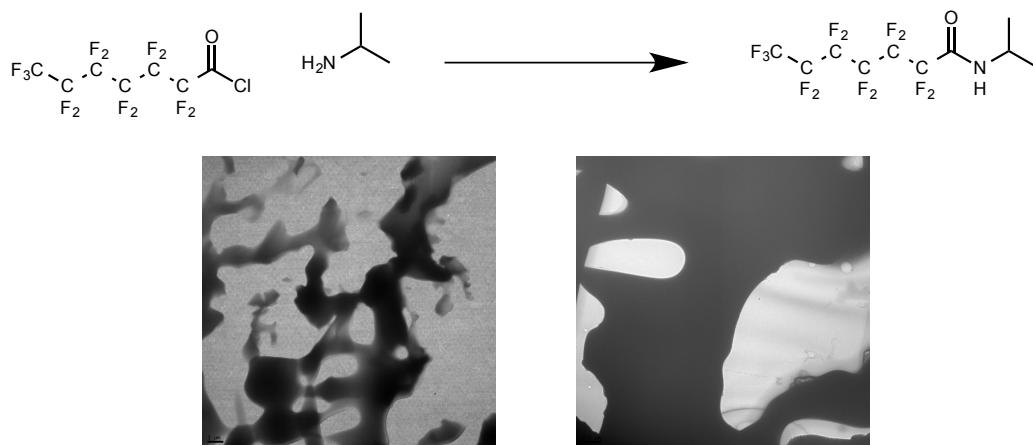


Figure 5.8: Generation of an analog of the released perfluorocarbon tail demonstrates rapid aggregation and electron dense contrast by TEM.

After synthesizing and purifying the full TEMarker agent, we tested whether or not the agent would cleave under UV light and liberate the perfluorocarbon tail required for TEM contrast.

To measure this cleavage, we used a handheld UV lamp at 365 nm to irradiate a solution of the agent. We then used MALDI to look for the cleaved fragment. Because the perfluorocarbon tail is expected to rapidly aggregate and fall out of solution, we instead followed the soluble portion of the cleavage product and were able to see both the intact agent and the soluble cleaved portion by MALDI (**Figure 5.9**).

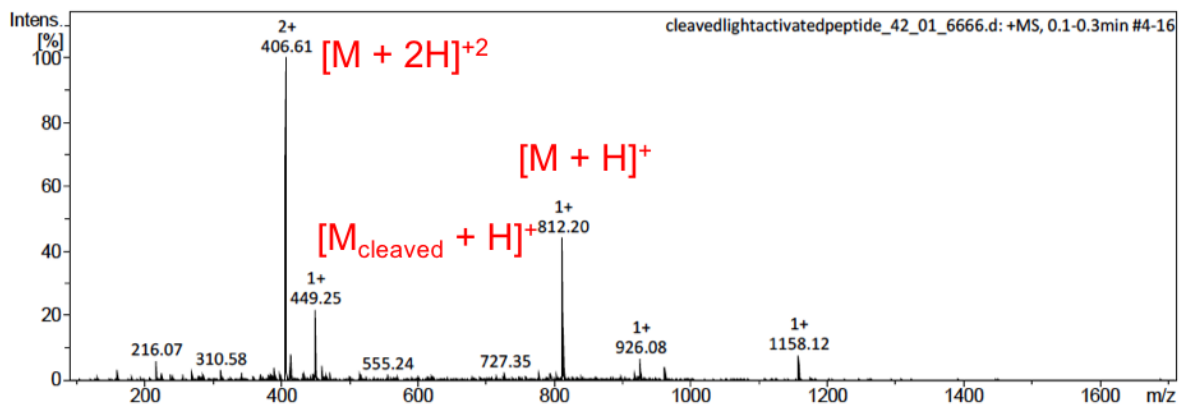
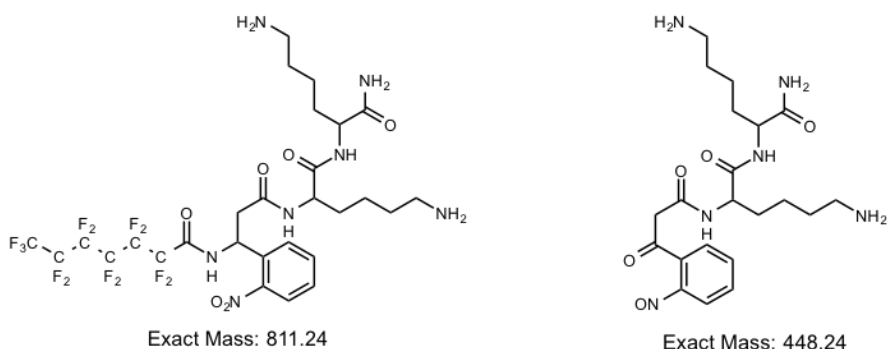


Figure 5.9: Test cleavage of first-generation TEMarker by MALDI. Following UV irradiation by handheld lamp, we observe the intact TEMarker as well as the soluble cleaved fragment by MALDI. The perfluorocarbon tail is expected to aggregate and rapidly crash out of solution thus it is not surprising that it is not observed.

Having demonstrated that cleavage by UV is possible, we explored the kinetics of that cleavage using UV-Vis spectroscopy. The agent was resuspended in water and placed in a quartz cuvette where it underwent ten rounds of sequential irradiation at 365 nm by handheld UV lamp for 1 minute (**Figure 5.10**). Initially, there is no signal at 405 nm, however with subsequent exposures to the UV lamp, a peak grows in at this wavelength. In addition, the absorbance at ~290 nm shows a steady decrease over subsequent rounds of exposure. This can be interpreted as loss of the nitrobenzyl group (~290 nm) and formation of the nitrosobenzyl group in the cleavage product (405 nm). Very similar activation kinetics were reported for photouncaging of MNI-glutamate, which also uses a nitrobenzyl group for photocleavage [198]. Activation is approximately one third of the max absorbance after the first minute of irradiation and two thirds of the max absorbance after the second minute of irradiation. After approximately five minutes, the increase at 405 nm saturates and very little change is observed in the UV-Vis spectra at later time points.

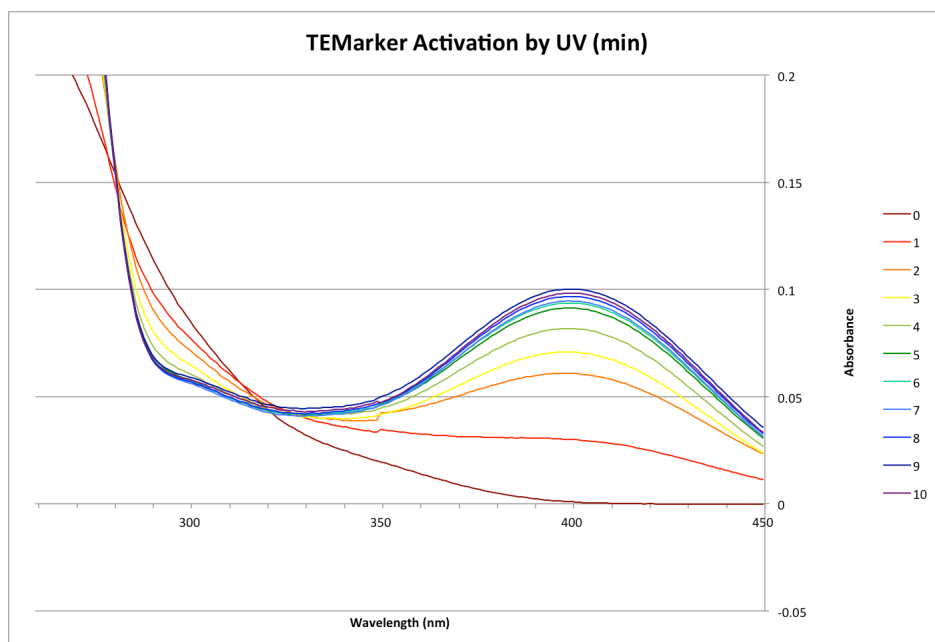


Figure 5.10: Cleavage of first-generation TEMarker agent followed by UV-Vis spectroscopy. As irradiation time increases, there is a decrease at 290 nm and an increase at 405 nm corresponding to the conversion of the nitrobenzyl in the intact agent to the nitrosobenzyl in the cleaved soluble fragment. Cleavage is approximately 66% complete after two rounds of irradiation by hand held UV lamp for 1 min and the effects of irradiation saturate at five minutes.

In addition to the aforementioned changes in the UV-Vis spectra of the soluble cleaved fragment, we also visually observed a progressive yellowing of the solution, as well as the formation of multiple small visually obvious aggregates within the cuvette. These likely correspond to foci of the aggregated perfluorocarbon tail and optimistically indicate that the tail will be able to rapidly self-assemble into similar aggregates in tissue samples.

In order to observe photocleavage leading to TEM contrast, solutions of TEMarker agent were activated on TEM grids using hand held UV. Because UV-Vis demonstrated saturation of cleavage after 5 minutes, this irradiation time was used to maximize potential signal. Control grids were spotted with agent but stored in the dark for 5 minutes. TEMarker solutions were prepped at three concentrations: 1.2 mM, 0.3 mM, and 75 μ M. 10 μ l was spotted onto the grids for each condition. Imaging revealed small electron dense aggregates on the photoactivated grids, but not on the dark controls (**Figure 5.11**). While the aggregates were sparse, the number and size of the aggregates seemed to be proportional to the initial concentration of the agent.

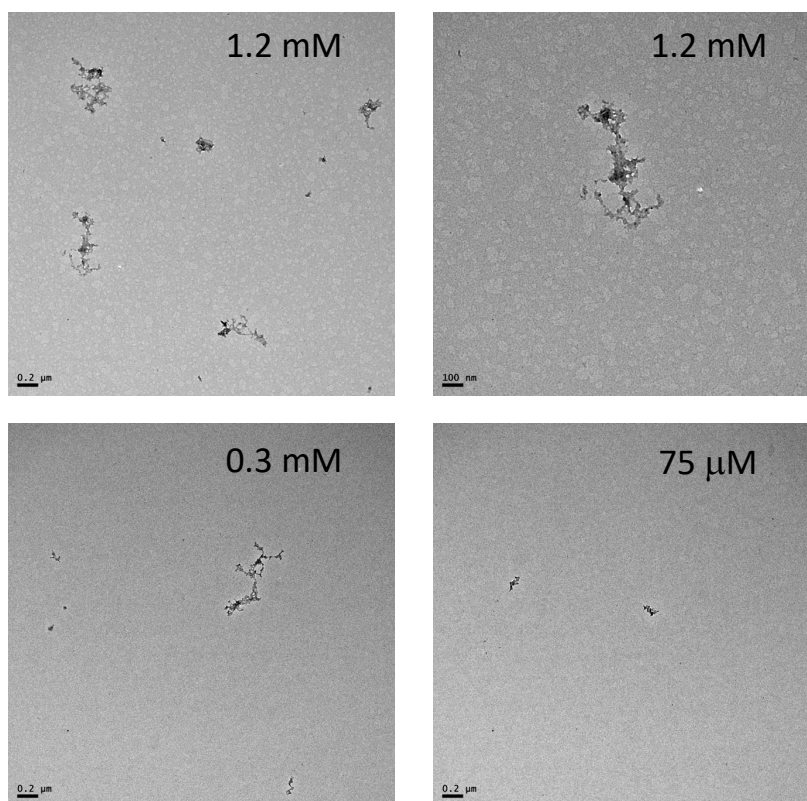


Figure 5.11: TEMarker contrast by TEM following on grid activation by handheld UV lamp. Small electron dense aggregates are apparent after photocleavage but are not present in samples kept in the dark. Aggregates are relatively sparse but seem to increase in size and number with increasing concentration of the agent.

Further characterization of the TEMarker agent was performed using a Nile Red assay to determine the critical micellar concentration (CMC). Because the full TEMarker agent is amphipathic with a hydrophilic charged end (lysines) and a hydrophobic end (perfluorocarbon tail), we hypothesized that it would form micelles in solution prior to cleavage. The fluorophore Nile Red is commonly used for identification of CMC as it shows a drastic increase in fluorescence when it is incorporated into the hydrophobic environment at the center of a micelle. Here we

observed that fluorescence increase between 1 mM and 5 mM, indicating that at the relevant doses for use in biological systems, the compound does for micelles (**Figure 5.12**).

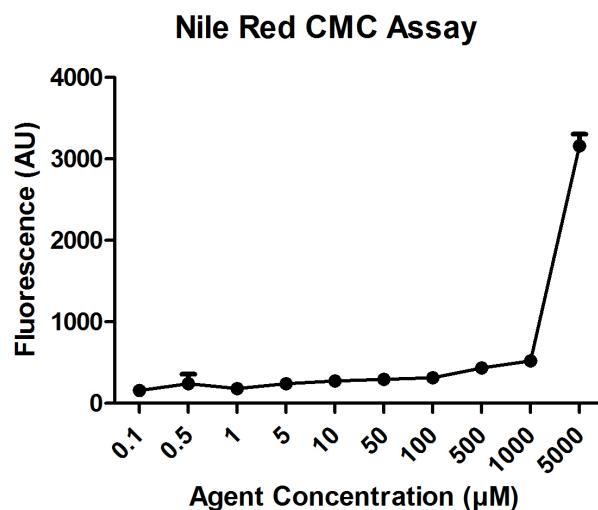


Figure 5.12: Critical micellar concentration for first-generation TEMarker as measured by Nile Red fluorescence. The CMC is between 1 and 5 mM, which is higher than the concentrations expected to be used in biological systems.

In order to further optimize the dosing concentration for biological systems, we measured cell viability via MTS assay (**Figure 5.13**). HT22 cells were dosed with increasing concentrations of the agents and viability was measured after 24 hours. Measurements were normalized to vehicle treated controls. At concentrations below 100 µM, the TEMarker agent showed no toxicity. The highest dose tested (500 µM) exhibited around 70% viability after 24 hours.

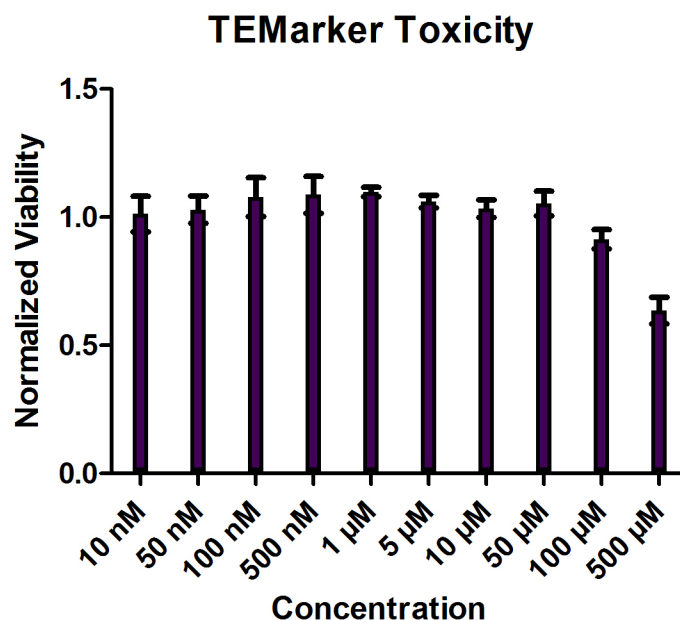


Figure 5.13: Cellular viability after 24 hours was assessed using the CellTiter 96 AQueous One Solution MTS Cell Proliferation Assay. At doses lower than 100 μM , no decrease in viability was observed.

Having successfully demonstrated UV activation of the TEMarker agent on grid, we next sought to activate by two-photon excitation in a spatially precise manner. To do this we created a model tissue system composed of cells suspended in an agarose noodle. The TEMarker agent was dissolved in PBS and the agarose noodles were placed in a solution containing the agent allowing free diffusion into the noodle matrix. Activation was achieved by illuminating in a line down the long axis of the noodle with a two-photon laser at 750 nm on an inverted confocal microscope. After activation, the noodles were fixed, dehydrated, embedded in resin, sectioned, and mounted on grids for TEM imaging.

Imaging data from the agarose embedding experiment was not conclusive. While certain areas of high and low contrast were identified, we had no way to distinguish where agent was activated and not activated. The imprecision associated with the activation method made it impossible to discern what signal was directly related to activation of the TEMarker agent. As such we focused on reworking the testing system to more accurately identify precise spatial locations of activation. Toward this end, we purchased London Finder grids, which are alpha numerically encoded grids that let you identify specific points in the TEM viewing window (Figure 5.4).

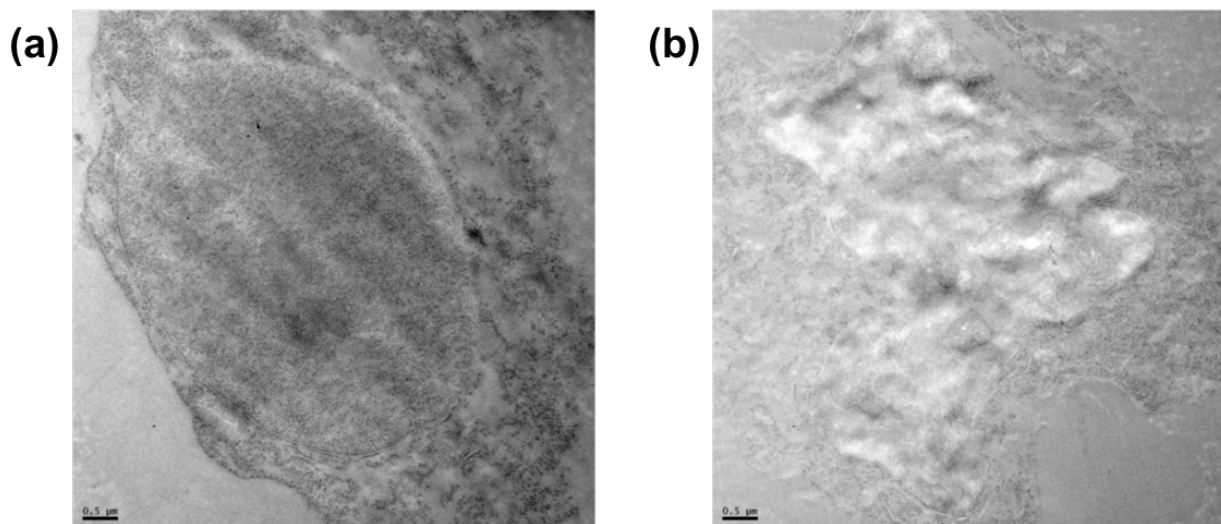


Figure 5.14: TEM images of agarose noodle embedded cells following two-photon activation. The cell on the left demonstrates significantly higher contrast and was from the activated noodle, while the cell on the right has poor contrast and was from the unactivated noodle. Despite the distinction between these two cells, there was no clear boundary between areas that were and were not activated. Therefore, it is impossible to conclude that these changes in contrast are solely attributable to TEMarker activation.

5.4.2 Second-generation Agent Characterization

Given the preliminary success of the first generation TEMarker agent, we also spent considerable synthetic effort developing a second generation of TEMarkers. These agents replaced the nitrobenzyl photocleavable group with a more red-shifted coumarin derivative. This allowed for two-photon excitation in the near IR region, improving tissue penetration and decreasing spectral overlap with the fluorescent proteins used to label the cells of interest, thus allowing simultaneous multiwavelength imaging.

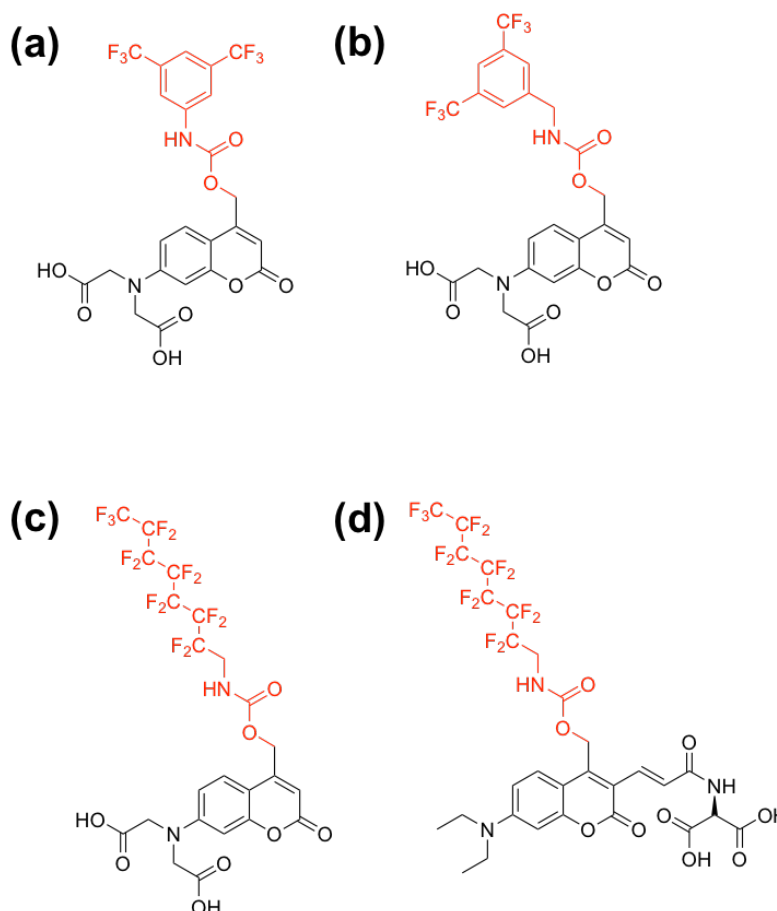


Figure 5.6: Four second generation red-shifted TEMarker agents. These agents replace the nitrobenzyl photocleavable group with coumarin derivatives that have two-photon excitation in

the near IR region. Agents (c) and (d) employ the same perfluorocarbon tail used in the generation one agent for contrast. Agents (a) and (b) instead use perfluorinated benzene derivatives to generate contrast.

Four new second generation agents were developed (**Figure 5.6**). Agent (a) TEMarker800 and agent (b) TEMarker800S replaced both the photocleavable group and the fluorinated moiety. These agents used fluorinated benzene derivatives instead of the perfluorocarbon tails used in the first-generation agent. When tested for photoactivation by hand held UV activation on grid, these agents demonstrated specific formation of electron dense aggregates after exposure to UV for 5 minutes (**Figure 5.15b and d**). Grids containing agent kept in the dark did not show any background activation (**Figure 5.15a and c**). Despite very similar chemical structures, the morphological character of the fluorous aggregates produced by TEMarker800 (**Figure 5.15b**) and TEMarker800S (**Figure 5.15d**) were visually distinct. Both generated aggregates that formed a reticular background of fibrils with darker foci of contrast scattered through. For TEMarker800S, the foci were considerable larger and more globular. These aggregates are very morphologically distinct compared to those observed for the first generation TEMarker (**Figure 5.11**), although this is not unexpected given that the perfluorinated group was replaced.

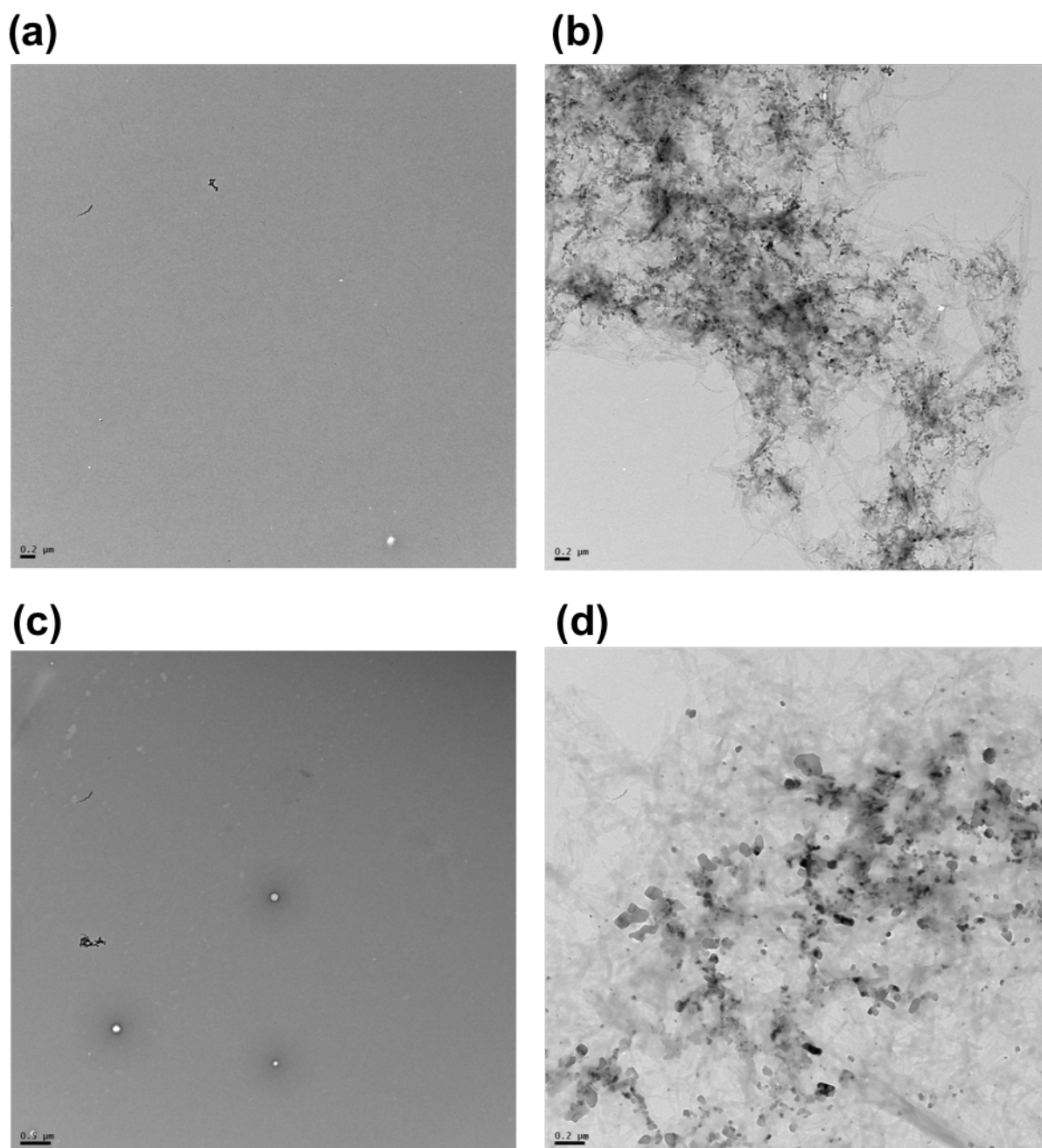


Figure 5.15: Second generation non-tail TEMarker contrast by TEM following on grid activation by handheld UV lamp. (a) TEMarker800 (Figure 5.6a) dark control, (b) TEMarker800 (Figure 5.6a) 5 min at 365 nm, (c) TEMarker800S (Figure 5.6b) dark control, (d) TEMarker800S (Figure 5.6b) 5 min at 365 nm.

5.6b) 5 min at 365 nm. No aggregates are identified in the dark controls. UV activation demonstrates reticular aggregates with small foci of increased contrast throughout.

Two additional second-generation agents were synthesized (**Figure 5.6c and d**). These agents adopted the new red-shifted coumarin photocleavable groups but retained the original perfluorocarbon tail of the first-generation agent. In contrast to the successful UV activation of TEMarker800 and 800S, these agents exhibited high background signal in the non-irradiated dark samples (**Figure 5.16**). In fact, the dark samples showed much higher contrast than the UV activated samples, with a shift from round punctate balls of contrast to more diffuse patchy activation after irradiation.

Given that both of the perfluorocarbon tail agents displayed this same high background signal with identical morphological features that did not completely go away but decreased after activation, we wondered if these round spots could represent large micelles of the unactivated agent. To test this hypothesis, we performed fluorescence microscopy on the grids and observed that some of the puncta had fluorescence matching the coumarin, however not all of them did (**Figure 5.17**). This suggested that the background aggregates might be heterogeneous in nature, with only some of them corresponding to aggregates of uncleaved agent. To check if these agents exhibited a low CMC, we performed a Nile Red assay (data not shown). The quality of the data from the Nile Red assay was poor, but we were able to estimate CMC values for the four second generation agents of (a) 200 μM , (b) 800 μM , (c) 200 μM , and (d) > 1 mM. The data for agent (d) was particularly poor, however the assay consumes a large amount of agent, so given our limited supply we elected not to repeat the CMC measurements.

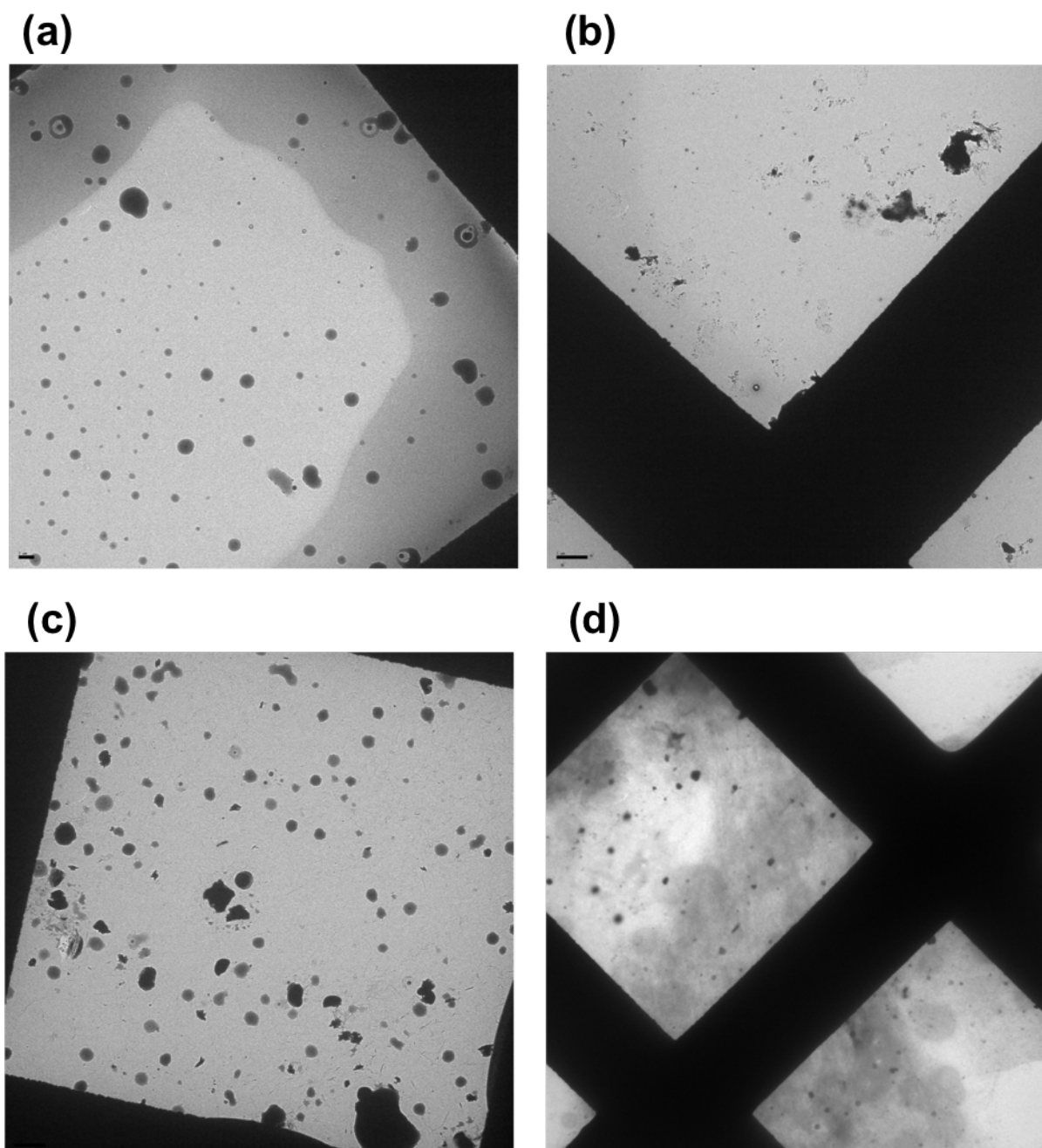


Figure 5.16: Second-generation tail TEMarker contrast by TEM following on grid activation by handheld UV lamp. (a) (**Figure 5.6c**) dark control, (b) (**Figure 5.6c**) 5 min at 365 nm, (c) (**Figure 5.6d**) dark control, (b) (**Figure 5.6d**) 5 min at 365 nm.

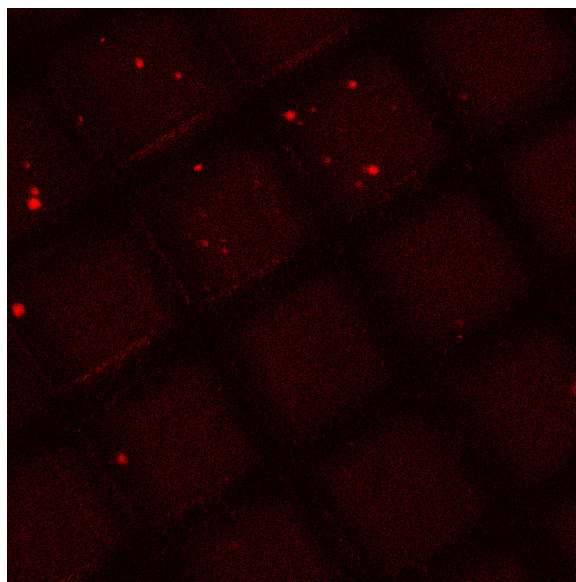
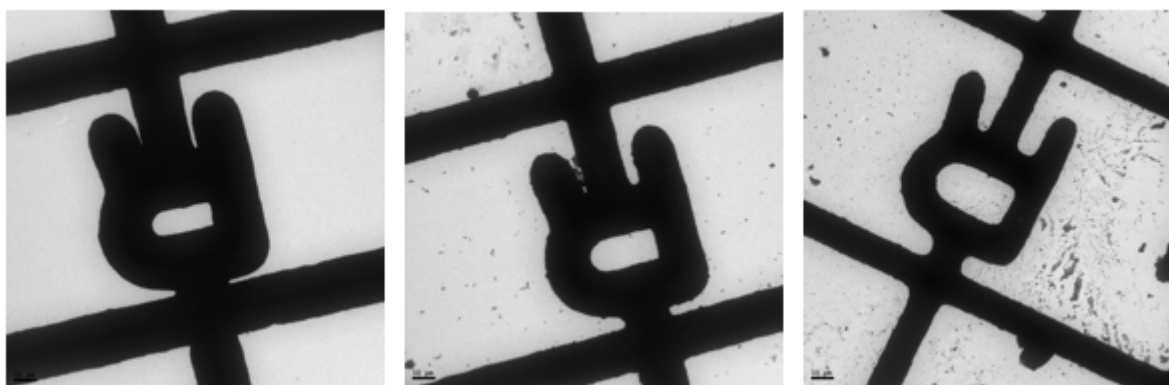


Figure 5.17: Fluorescence imaging of grid from **Figure 5.16c** demonstrates that some of the blobs of contrast are aggregates of the uncleaved agent. However, there are many more balls of contrast visible by TEM than identified by fluorescence, suggesting that the background contrast might be heterogeneous.

While progress on the second-generation tail agents was halted due to their high background signal, we proceeded with characterization of the two non-tail agents: TEMarker800 and TEMarker800S. Having successfully shown activation specific contrast by UV activation, we decided to test the agents for spatial precision by two-photon activation on London Finder grids. Because we were concerned about grid manipulation resulting in movement of the aggregates, we tested a variety of techniques for activation (**Figure 5.18**).

For two-photon activation studies, 10 μl of the suspended agent is spotted onto a grid. An alphanumeric position on the grid is identified by brightfield microscopy and then irradiated by two-photon for 1 minute. Excess fluid must be removed before the grid can be imaged. Traditionally this is accomplished via blotting with filter paper, which wicks excess solution off

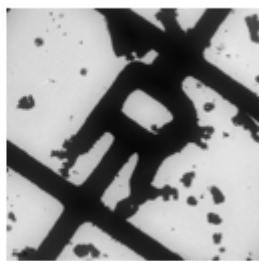
the grid. However, concerned that this wicking action was causing the aggregates to move from the precise point of activation, we tested other methods including blotting before the activation, and drying the grids by evaporation. Drying by evaporation did not work since the agent crashed out as it dried forming electron dense contrast. Comparison of blotting before and after activation showed similar levels of contrast. While blotting beforehand reduces the fluid movement once the aggregates are formed, it drastically decreases the amount of agent available for photoactivation to only a thin meniscus left coating the surface of the grid. In contrast, blotting after the activation leads to increased fluid flow, but a much higher amount of agent available for activation. Based on this experiment, we concluded that blotting before activation reduces the agent concentration too much to be a viable strategy. As such we moved forward with our protocol development utilizing the activate then blot methodology.



10 ul, no activation, blot

10 ul, 1 min 2PE, blot

10 ul, blot, 1 min



3 ul, no activation, evap



3 ul, 1 min 2PE, evap

Figure 5.18: Two-photon activation of TEMarker800 on London Finder grids for determination of blotting methodology. All grids were activated at the R position according the above described methods indicating 1) volume of agent on the grid, 2) activation method, 3) excess solution removal method. Evaporation was not an effective way to remove excess agent since it just crashed out. Both conditions that were activated showed enhanced contrast compared to the dark control. Neither shows good spatial localization.

Two-photon activation of TEMarker800S on London Finder grids demonstrates the primary issue faced with these second-generation agents: namely spatial aggregation precision. A grid was activated for 60 seconds at position K, a second grid was activated at position R for 5 seconds. A third grid was not activated at all. This grid did not show signal, reinforcing the idea that the contrast generated by these agents is photoactivation specific. However, the grids that were activated for 5 and 60 seconds both showed diffuse contrast throughout, not limited to the positions at which the activation occurred. The contrast did appear to be proportional to the radiation length, with the 60 second exposure grid have more aggregates than the 5 second exposure grid.

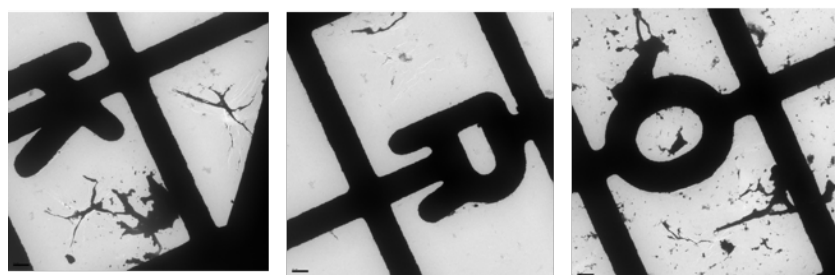


Figure 5.19: Two-photon activation of TEMarker800S on London Finder grid demonstrating spatial imprecision. These grids were activated for 60 seconds at position K and 5 seconds at

position R. The final image is the O position on the grid that irradiated for 60 seconds. This position shows significant contrast even though activation was only performed at position K.

5.5 Discussion

In this chapter, the feasibility of using fluoruous aggregates as TEM contrast agents was investigated. Successful synthesis and characterization of the first-generation proof of principle TEMarker was used to develop methodologies for testing these TEM contrast agents. We demonstrated successful photocleavage by MALDI and UV-Vis spectroscopy before measuring contrast directly using TEM. There we first demonstrated successful cleavage by hand held single photon UV excitation and observed the formation of electron dense aggregates only in photoactivated samples. We then explored methodologies for measuring spatial precise activation by two-photon excitation using enrobed cell agarose noodle tissue models as well as London Finder grids.

In order to create agents with the ideal excitation wavelengths, the synthesis was adapted to feature coumarin based photocleavable groups, as well as two kinds of fluorinated aggregation moieties. These new agents were also characterized by TEM. The second-generation tail agents were found to exhibit high background contrast and were thus unsuitable for use as an activatable contrast agent. Further inquiry into the exact cause of the high background showed some evidence of micelle formation but was ultimately inconclusive.

The second-generation non-tail agents TEMarker800 and TEMarker800S exhibited more promising activation results by UV activation. However, neither demonstrated exclusive signal only in the region of two-photon activation, indicating either that the activation is spatially imprecise (unlikely due to the use of two-photon excitation which has a small excitation volume)

or that the aggregates are moving once activated. Because removal of the excess fluids by blotting generates a significant fluid force across the grid surface, it is likely that this is the cause for the spatial instability.

5.6 Future Directions

While significant work was completed toward the TEMarkers project, there are still critical hurdles that must be addressed before this work is publishable. These hurdles can be summarized as follows from most to least serious: 1) failure of the second-generation tail agent negative controls, 2) spatial imprecision of the fluoruous aggregates, 3) spatial imprecision of the activation strategy, and 4) shifting biological applications based on synthetic alterations.

The first and most serious issue is that the two second generation perfluorocarbon tail agents demonstrate significant TEM signal before activation (**Figure 5.16**). Because the primary function of TEMarkers is to highlight areas of interest after photoactivation, this problem inhibits any potential for utility of these agents. It may be that agents are contaminated with excess perfluorocarbon tail, however this would have likely been purified out and is seen in both agents. It is unlikely that the problem is caused by the perfluorous tail itself, since this was not observed for the first-generation agent which also used the same perfluorocarbon tail. For these two agents to be viable TEMarkers, these experiments must be repeated with a new batch of agent, which would require considerable synthetic effort. Alternatively, these two agents could be dropped in favor of the two non-tail second generation agents: TEMarker800 and TEMarker800S.

In contrast to the second-generation tail agents, TEMarker800 and 800S exhibited excellent activation by UV-Vis with the dark controls showing no signal compared to the formation of electron dense aggregates in the photoactivated samples (**Figure 5.15**). The primary failure of

TEMarker800 and 800s is not in their ability to specifically photocleave, but in their ability to aggregate in a spatially precise manner. For biological utility, the TEMarker must only effectively cleave in response to photoactivation, but the fluororous part must aggregate quickly and in a spatially precise manner. In order to test this, we conducted two photo activation tests using London Finder grids where activation was limited to specific geographic locations on the grids. Unfortunately, we observed that signal did not remain at the focus of activation, but rather freely diffused around the grid (**Figure 5.18 and 5.19**). This is likely caused by two separate problems 1) imprecision in the two-photon activation method and 2) imprecision in the spatial localization of the fluororous aggregates. Both of these must be addressed for successful development of TEMarker800 and TEMarker800S.

Activation imprecision is the easier of these problems to address. Our current method of activation involves manually moving the microscope stage while concurrently scanning with the laser. Utilizing a confocal microscope with a motorized stage (available downtown) and systematically mapping out the area of activation in 3D would likely greatly improve the ability to distinguish contrast caused by activation from background. In addition, a better appreciation of the area of activation would make optimization of the assay much higher throughput and allow better determination of other variables such as agent dose, radiation time, laser power, etc. As such, this problem should be addressed first.

While poor aggregate localization after photocleavage is a significant problem since spatial precision is mandatory for a successful TEMarker, it may be an artificial one. Our current method of measuring spatial activation involves only the TEMarker solution on an empty grid. An actual biological system would involve cells and extracellular matrix. It may be that the inability of the TEMarker to deposit in a precise manner is solely due to the emptiness of the grid and that when

introduced to the complex geography of a biological matrix it would easily adhere. This could be readily tested by switching to either tissue or cells grown on a TEM grid. However, steps complicating the surface of the grid should only be undertaken once a more rigorous activation protocol is established.

Finally, changes in the agent design necessitate changes in the biological function of these agents. While originally designed to markers of induced synaptogenesis for TEM imaging, the non-tail second generation agents (TEMarker800 and TEMarker800S) are not compatible with this application. By switching away from the tail design, the fluoruous aggregates are no longer stable in ethanol, which is a required component in the fixation and embedding of brain tissue such as would be used for induced synaptogenesis studies. If the primary motivation is to develop agents for use in the original biological application, the non-tail agents will not work. However, with the growing popularity of cryoEM, the need for ethanol-based fixation could be bypassed.

For example, a potential biological application involving a collaboration with Klein lab is detailed below. After developing a more systematic two-photon activation method, primary neuronal cells could be grown on polylysine coated gold London Finder grids. Using photocaged MNI-L-glutamate, *de novo* synapse formation could be induced at precise cellular locations (further identified by precise London Finder coordinates), concurrently photoactivating the TEMarker agent. The effects of A β O_s on early synapse generation could be studied at the single synapse level using cryoEM using the TEMarker aggregate (correlated with the London Finder coordinates) to identify the newly induced synapse. If cellular processes are thin enough frozen cells could be directly imaged. If not thinning techniques such as Focused Ion Beam (FIB) milling could be employed to produce windows of adequate thickness for imaging.[199] Following

success with cells in grids, this technique could be expanded to study the effects of A β O_s on early synapse development in acute tissue slices at the single synapse level.

5.7 Acknowledgements

Significant synthetic contributions were made to this project by chemists Adam Preslar, Hao Li, and Chris Brue. We thank Charlene Wilke from Northwestern's NUANCE Facility for help with agarose enrobing and TEM imaging, Keith MacRenaris for help with two-photon confocal microscopy, and Professor Genia Kozorovitskiy for early conceptual development of this project. We thank Kang Du and the Harris lab for use of their UV-Vis spectrometer. We thank the Stupp group for use of their peptide synthesis materials.

This work made use of the EPIC facility of Northwestern University's NUANCE Center, which has received support from the Soft and Hybrid Nanotechnology Experimental (SHyNE) Resource (NSF ECCS-1542205); the MRSEC program (NSF DMR-1720139) at the Materials Research Center; the International Institute for Nanotechnology (IIN); the Keck Foundation; and the State of Illinois, through the IIN.

CHAPTER 6

6 Summary and Future Directions**6.1 Summary**

The work outlined in this thesis details the development of Co(III)-sb complexes as inhibitors of amyloid aggregation. We have shown potent inhibition of aggregation by a variety of methodologies and for various isoform ratios. Aggregation studies consistently demonstrate that binding of Co(III)-sb to A β rapidly alters the peptide structure, favoring formation of off-pathway high molecular weight aggregates. Taken together these effects are promising because the interaction of Co(III)-sb with A β seems to drive the aggregation quickly passed the small oligomeric stage, which is most heavily implicated in toxicity. While *in vitro* amyloid aggregation studies are subject to many confounding variables, each is well suited to certain applications. Thus the use of multiple modalities allows collection of complementary data that reinforces observed aggregation effects.

Work on the aggregation effects of Co(III)-sb binding, was further complemented with the addition of computational modeling. While all experimental methods for measuring aggregation are at the bulk scale, and the computational work described was either at the monomer or pentamer scale, the integration of these two diverse methodologies gives a more mechanistic understanding of A β dynamics during aggregation.

In addition to measuring the effects of Co(III)-sb on aggregation, we also explored competitive metal displacement, measurement of ROS and markers of oxidative stress, and effects of Co(III)-sb on A β -mediated cellular toxicity. While direct measurement of metal competitive binding experiments were not successful, indirect evidence by ThT fluorescence and CCA assay demonstrate that Co(III)-sb is indeed able to displace Cu(II) from the N-terminal His residues of

A β . Additionally, while assay to measure oxidation failed, we did successfully demonstrate compelling rescue of A β -mediated cellular toxicity in response to treatment with Co(III)-sb.

Finally, we outlined the development of novel photocleavable contrast agents for TEM. We successfully synthesized and characterized five agents that undergo photocleavage and release a fluorinated moiety which aggregates and provides contrast by TEM. Additional development and demonstration of the biological utility of these agents is underway.

6.2 Future Directions

Here I will outline some future directions for the Co(III)-sb A β project. Future directions for TEMarkers are detailed in **Section 5.6**.

The work presented here includes a thorough characterization of bulk aggregation effects. However, oligomers have been identified as the most biologically interesting aggregate species, yet are often poorly characterized by the majority of techniques employed here. As such, the logical next direction for this project is to measure the effects of Co(III)-sb on oligomeric population dynamics. Chris has already initiated this work.

The second obvious direction for this project is the addition of a targeting moiety. All of the *in vitro* work described in this thesis did not require a targeted agent since it only involved protein in solution. However, any hope for eventual utility *in vivo* is entirely dependent on the identification and synthesis of a specific targeting moiety that will facilitate BBB penetration. Reviews of various groups used for targeting A β are available in the literature and could act as a starting point. However, unlike the ZFTFs which have a highly specific binding partner, many of the A β targeting groups just rely on small nonspecific peptide interactions. This will make the generation of a selective A β inhibitor much more difficult. Computational modeling could be

leveraged to facilitate the design of the targeted agents by modeling the binding energies of the various targeting groups and choosing the strongest binders for synthesis and characterization.

Further cellular work could use primary neurons to study downstream mechanisms of toxicity including effects on tau hyperphosphorylation, membrane deficits, aberrant calcium signaling, mitochondrial and metabolic changes, etc. In addition, pending the development of a specific A β -targeted Co(III)-sb complex, mouse models of AD could be used to investigate both biological effects of Co(III)-sb treatment as well as behavioral effects.

References

1. Thies, W., L. Bleiler, and A. Alzheimer's, *2013 Alzheimer's disease facts and figures*. *Alzheimers Dement*, 2013. **9**(2): p. 208-45.
2. Hardy, J. and D.J. Selkoe, *The amyloid hypothesis of Alzheimer's disease: progress and problems on the road to therapeutics*. *Science*, 2002. **297**(5580): p. 353-6.
3. Greenough, M.A., J. Camakaris, and A.I. Bush, *Metal dyshomeostasis and oxidative stress in Alzheimer's disease*. *Neurochem Int*, 2013. **62**(5): p. 540-55.
4. Smith, D.G., R. Cappai, and K.J. Barnham, *The redox chemistry of the Alzheimer's disease amyloid beta peptide*. *Biochim Biophys Acta*, 2007. **1768**(8): p. 1976-90.
5. Miura, T., et al., *Metal binding modes of Alzheimer's amyloid beta-peptide in insoluble aggregates and soluble complexes*. *Biochemistry*, 2000. **39**(23): p. 7024-31.
6. Bush, A.I., *The metal theory of Alzheimer's disease*. *J Alzheimers Dis*, 2013. **33 Suppl 1**: p. S277-81.
7. Viles, J.H., *Metal ions and amyloid fiber formation in neurodegenerative diseases. Copper, zinc and iron in Alzheimer's, Parkinson's and prion diseases*. *Coordination Chemistry Reviews*, 2012. **256**(19-20): p. 2271-2284.
8. Huang, X., et al., *Cu(II) potentiation of alzheimer abeta neurotoxicity. Correlation with cell-free hydrogen peroxide production and metal reduction*. *J Biol Chem*, 1999. **274**(52): p. 37111-6.
9. Curtain, C.C., et al., *Alzheimer's disease amyloid-beta binds copper and zinc to generate an allosterically ordered membrane-penetrating structure containing superoxide dismutase-like subunits*. *J Biol Chem*, 2001. **276**(23): p. 20466-73.

10. Opazo, C., et al., *Metalloenzyme-like activity of Alzheimer's disease beta-amyloid. Cu-dependent catalytic conversion of dopamine, cholesterol, and biological reducing agents to neurotoxic H(2)O(2)*. J Biol Chem, 2002. **277**(43): p. 40302-8.
11. Selkoe, D.J., *Alzheimer's disease: genes, proteins, and therapy*. Physiol Rev, 2001. **81**(2): p. 741-66.
12. Zempel, H., et al., *Abeta oligomers cause localized Ca(2+) elevation, missorting of endogenous Tau into dendrites, Tau phosphorylation, and destruction of microtubules and spines*. J Neurosci, 2010. **30**(36): p. 11938-50.
13. Eichner, T. and S.E. Radford, *A diversity of assembly mechanisms of a generic amyloid fold*. Mol Cell, 2011. **43**(1): p. 8-18.
14. Fitzpatrick, A.W., et al., *Atomic structure and hierarchical assembly of a cross-beta amyloid fibril*. Proc Natl Acad Sci U S A, 2013. **110**(14): p. 5468-73.
15. Gremer, L., et al., *Fibril structure of amyloid-beta(1-42) by cryo-electron microscopy*. Science, 2017. **358**(6359): p. 116-119.
16. Klein, W.L., *Synaptotoxic amyloid-beta oligomers: a molecular basis for the cause, diagnosis, and treatment of Alzheimer's disease?* J Alzheimers Dis, 2013. **33 Suppl 1**: p. S49-65.
17. Benilova, I., E. Karran, and B. De Strooper, *The toxic Abeta oligomer and Alzheimer's disease: an emperor in need of clothes*. Nat Neurosci, 2012. **15**(3): p. 349-57.
18. Lambert, M.P., et al., *Diffusible, nonfibrillar ligands derived from Abeta1-42 are potent central nervous system neurotoxins*. Proc Natl Acad Sci U S A, 1998. **95**(11): p. 6448-53.
19. McLean, C.A., et al., *Soluble pool of Abeta amyloid as a determinant of severity of neurodegeneration in Alzheimer's disease*. Ann Neurol, 1999. **46**(6): p. 860-6.

20. Bao, F., et al., *Different beta-amyloid oligomer assemblies in Alzheimer brains correlate with age of disease onset and impaired cholinergic activity*. Neurobiol Aging, 2012. **33**(4): p. 825 e1-13.
21. Stine, W.B., Jr., et al., *In vitro characterization of conditions for amyloid-beta peptide oligomerization and fibrillogenesis*. J Biol Chem, 2003. **278**(13): p. 11612-22.
22. Lee, C.F., et al., *Combined effects of agitation, macromolecular crowding, and interfaces on amyloidogenesis*. J Biol Chem, 2012. **287**(45): p. 38006-19.
23. Benseny-Cases, N., O. Klementieva, and J. Cladera, *In vitro Oligomerization and Fibrillogenesis of Amyloid-beta Peptides*. Subcell Biochem, 2012. **65**: p. 53-74.
24. Burgold, S., et al., *In vivo imaging reveals sigmoidal growth kinetic of beta-amyloid plaques*. Acta Neuropathol Commun, 2014. **2**(1): p. 30.
25. Murakami, K., et al., *Neurotoxicity and physicochemical properties of Abeta mutant peptides from cerebral amyloid angiopathy: implication for the pathogenesis of cerebral amyloid angiopathy and Alzheimer's disease*. J Biol Chem, 2003. **278**(46): p. 46179-87.
26. Wogulis, M., et al., *Nucleation-dependent polymerization is an essential component of amyloid-mediated neuronal cell death*. J Neurosci, 2005. **25**(5): p. 1071-80.
27. Bartolini, M., et al., *Kinetic characterization of amyloid-beta 1-42 aggregation with a multimethodological approach*. Anal Biochem, 2011. **414**(2): p. 215-25.
28. Bruggink, K.A., et al., *Methods for analysis of amyloid-beta aggregates*. J Alzheimers Dis, 2012. **28**(4): p. 735-58.
29. Atwood, C.S., et al., *Role of free radicals and metal ions in the pathogenesis of Alzheimer's disease*. Met Ions Biol Syst, 1999. **36**: p. 309-64.

30. Lovell, M.A., et al., *Copper, iron and zinc in Alzheimer's disease senile plaques*. J Neurol Sci, 1998. **158**(1): p. 47-52.
31. Schrag, M., et al., *Iron, zinc and copper in the Alzheimer's disease brain: a quantitative meta-analysis. Some insight on the influence of citation bias on scientific opinion*. Prog Neurobiol, 2011. **94**(3): p. 296-306.
32. Cherny, R.A., et al., *Aqueous dissolution of Alzheimer's disease A β amyloid deposits by biometal depletion*. J Biol Chem, 1999. **274**(33): p. 23223-8.
33. Phinney, A.L., et al., *In vivo reduction of amyloid-beta by a mutant copper transporter*. Proc Natl Acad Sci U S A, 2003. **100**(24): p. 14193-8.
34. Cherny, R.A., et al., *Treatment with a copper-zinc chelator markedly and rapidly inhibits beta-amyloid accumulation in Alzheimer's disease transgenic mice*. Neuron, 2001. **30**(3): p. 665-76.
35. Bush, A.I., et al., *Rapid induction of Alzheimer A β amyloid formation by zinc*. Science, 1994. **265**(5177): p. 1464-7.
36. Atwood, C.S., et al., *Dramatic aggregation of Alzheimer abeta by Cu(II) is induced by conditions representing physiological acidosis*. J Biol Chem, 1998. **273**(21): p. 12817-26.
37. Chen, W.T., et al., *Distinct effects of Zn²⁺, Cu²⁺, Fe³⁺, and Al³⁺ on amyloid-beta stability, oligomerization, and aggregation: amyloid-beta destabilization promotes annular protofibril formation*. J Biol Chem, 2011. **286**(11): p. 9646-56.
38. Faller, P., C. Hureau, and O. Berthoumieu, *Role of metal ions in the self-assembly of the Alzheimer's amyloid-beta peptide*. Inorg Chem, 2013. **52**(21): p. 12193-206.
39. Atrian-Blasco, E., et al., *Cu and Zn coordination to amyloid peptides: From fascinating chemistry to debated pathological relevance*. Coord Chem Rev, 2018. **375**: p. 38-55.

40. Hane, F. and Z. Leonenko, *Effect of Metals on Kinetic Pathways of Amyloid- β Aggregation*. *Biomolecules*, 2014. **4**(1): p. 101-116.
41. Sarell, C.J., et al., *Copper(II) binding to amyloid-beta fibrils of Alzheimer's disease reveals a picomolar affinity: stoichiometry and coordination geometry are independent of Abeta oligomeric form*. *Biochemistry*, 2009. **48**(20): p. 4388-402.
42. Alies, B., et al., *Zinc(II) Binding Site to the Amyloid-beta Peptide: Insights from Spectroscopic Studies with a Wide Series of Modified Peptides*. *Inorg Chem*, 2016. **55**(20): p. 10499-10509.
43. Miller, Y., B. Ma, and R. Nussinov, *Metal binding sites in amyloid oligomers: Complexes and mechanisms*. *Coordination Chemistry Reviews*, 2012. **256**(19-20): p. 2245-2252.
44. Tougu, V., A. Tiiman, and P. Palumaa, *Interactions of Zn(II) and Cu(II) ions with Alzheimer's amyloid-beta peptide. Metal ion binding, contribution to fibrillization and toxicity*. *Metallomics*, 2011. **3**(3): p. 250-61.
45. Atwood, C.S., et al., *Characterization of copper interactions with alzheimer amyloid beta peptides: identification of an attomolar-affinity copper binding site on amyloid beta1-42*. *J Neurochem*, 2000. **75**(3): p. 1219-33.
46. Talmard, C., A. Bouzan, and P. Faller, *Zinc binding to amyloid-beta: isothermal titration calorimetry and Zn competition experiments with Zn sensors*. *Biochemistry*, 2007. **46**(47): p. 13658-66.
47. Faller, P. and C. Hureau, *Bioinorganic chemistry of copper and zinc ions coordinated to amyloid-beta peptide*. *Dalton Trans*, 2009(7): p. 1080-94.
48. Huang, X., et al., *Zinc-induced Alzheimer's Abeta1-40 aggregation is mediated by conformational factors*. *J Biol Chem*, 1997. **272**(42): p. 26464-70.

49. Tougu, V., A. Karafin, and P. Palumaa, *Binding of zinc(II) and copper(II) to the full-length Alzheimer's amyloid-beta peptide*. J Neurochem, 2008. **104**(5): p. 1249-59.
50. Noel, S., et al., *Use of a new water-soluble Zn sensor to determine Zn affinity for the amyloid-beta peptide and relevant mutants*. Metallomics, 2014. **6**(7): p. 1220-2.
51. Conte-Daban, A., et al., *Link between Affinity and Cu(II) Binding Sites to Amyloid-beta Peptides Evaluated by a New Water-Soluble UV-Visible Ratiometric Dye with a Moderate Cu(II) Affinity*. Anal Chem, 2017. **89**(3): p. 2155-2162.
52. Frederickson, C.J., et al., *Concentrations of extracellular free zinc (pZn) in the central nervous system during simple anesthetization, ischemia and reperfusion*. Exp Neurol, 2006. **198**(2): p. 285-93.
53. Frederickson, C.J. and G. Danscher, *Zinc-containing neurons in hippocampus and related CNS structures*. Prog Brain Res, 1990. **83**: p. 71-84.
54. Hartter, D.E. and A. Barnea, *Evidence for release of copper in the brain: depolarization-induced release of newly taken-up 67copper*. Synapse, 1988. **2**(4): p. 412-5.
55. Lee, J.Y., et al., *Contribution by synaptic zinc to the gender-disparate plaque formation in human Swedish mutant APP transgenic mice*. Proc Natl Acad Sci U S A, 2002. **99**(11): p. 7705-10.
56. Huang, X., et al., *Trace metal contamination initiates the apparent auto-aggregation, amyloidosis, and oligomerization of Alzheimer's Abeta peptides*. J Biol Inorg Chem, 2004. **9**(8): p. 954-60.
57. Sarell, C.J., S.R. Wilkinson, and J.H. Viles, *Substoichiometric levels of Cu²⁺ ions accelerate the kinetics of fiber formation and promote cell toxicity of amyloid- β from Alzheimer disease*. J Biol Chem, 2010. **285**(53): p. 41533-40.

58. Tougu, V., et al., *Zn(II)- and Cu(II)-induced non-fibrillar aggregates of amyloid-beta (1-42) peptide are transformed to amyloid fibrils, both spontaneously and under the influence of metal chelators*. J Neurochem, 2009. **110**(6): p. 1784-95.
59. Yoshiike, Y., et al., *New insights on how metals disrupt amyloid beta-aggregation and their effects on amyloid-beta cytotoxicity*. J Biol Chem, 2001. **276**(34): p. 32293-9.
60. Pedersen, J.T., et al., *Cu(II) mediates kinetically distinct, non-amyloidogenic aggregation of amyloid-beta peptides*. J Biol Chem, 2011. **286**(30): p. 26952-63.
61. Smith, D.P., et al., *Concentration dependent Cu²⁺ induced aggregation and dityrosine formation of the Alzheimer's disease amyloid-beta peptide*. Biochemistry, 2007. **46**(10): p. 2881-91.
62. Sharma, A.K., et al., *The effect of Cu(2+) and Zn(2+) on the Abeta42 peptide aggregation and cellular toxicity*. Metallomics, 2013. **5**(11): p. 1529-36.
63. Raman, B., et al., *Metal ion-dependent effects of clioquinol on the fibril growth of an amyloid {beta} peptide*. J Biol Chem, 2005. **280**(16): p. 16157-62.
64. Innocenti, M., et al., *Trace copper(II) or zinc(II) ions drastically modify the aggregation behavior of amyloid-beta1-42: an AFM study*. J Alzheimers Dis, 2010. **19**(4): p. 1323-9.
65. Smith, D.G., et al., *Histidine 14 modulates membrane binding and neurotoxicity of the Alzheimer's disease amyloid-beta peptide*. J Alzheimers Dis, 2010. **19**(4): p. 1387-400.
66. Nakamura, M., et al., *Three histidine residues of amyloid-beta peptide control the redox activity of copper and iron*. Biochemistry, 2007. **46**(44): p. 12737-43.
67. Huang, X., et al., *The A beta peptide of Alzheimer's disease directly produces hydrogen peroxide through metal ion reduction*. Biochemistry, 1999. **38**(24): p. 7609-16.

68. Reybier, K., et al., *Free Superoxide is an Intermediate in the Production of H₂O₂ by Copper(I)-Abeta Peptide and O₂*. *Angew Chem Int Ed Engl*, 2016. **55**(3): p. 1085-9.
69. Naslund, J., et al., *Relative abundance of Alzheimer A beta amyloid peptide variants in Alzheimer disease and normal aging*. *Proc Natl Acad Sci U S A*, 1994. **91**(18): p. 8378-82.
70. Cuajungco, M.P., et al., *Evidence that the beta-amyloid plaques of Alzheimer's disease represent the redox-silencing and entombment of abeta by zinc*. *J Biol Chem*, 2000. **275**(26): p. 19439-42.
71. Behl, C., et al., *Hydrogen peroxide mediates amyloid beta protein toxicity*. *Cell*, 1994. **77**(6): p. 817-27.
72. Crouch, P.J., et al., *Mechanisms of A beta mediated neurodegeneration in Alzheimer's disease*. *Int J Biochem Cell Biol*, 2008. **40**(2): p. 181-98.
73. Santos, M.A., K. Chand, and S. Chaves, *Recent progress in multifunctional metal chelators as potential drugs for Alzheimer's disease*. *Coordination Chemistry Reviews*, 2016. **327-328**: p. 287-303.
74. Crouch, P.J., et al., *The Alzheimer's therapeutic PBT2 promotes amyloid-beta degradation and GSK3 phosphorylation via a metal chaperone activity*. *J Neurochem*, 2011. **119**(1): p. 220-30.
75. Matlack, K.E., et al., *Clioquinol promotes the degradation of metal-dependent amyloid-beta (Abeta) oligomers to restore endocytosis and ameliorate Abeta toxicity*. *Proc Natl Acad Sci U S A*, 2014. **111**(11): p. 4013-8.
76. Haas, K.L. and K.J. Franz, *Application of metal coordination chemistry to explore and manipulate cell biology*. *Chem Rev*, 2009. **109**(10): p. 4921-60.

77. Biran, Y., et al., *Pharmacotherapeutic targets in Alzheimer's disease*. J Cell Mol Med, 2009. **13**(1): p. 61-86.
78. Barnham, K.J., et al., *Platinum-based inhibitors of amyloid-beta as therapeutic agents for Alzheimer's disease*. Proc Natl Acad Sci U S A, 2008. **105**(19): p. 6813-8.
79. Ma, G., et al., *Identification of [PtCl₂(phen)] binding modes in amyloid-beta peptide and the mechanism of aggregation inhibition*. Chemistry, 2011. **17**(41): p. 11657-66.
80. Heffern, M.C., et al., *Cobalt derivatives as promising therapeutic agents*. Curr Opin Chem Biol, 2013. **17**(2): p. 189-96.
81. Collin, F., et al., *Pt(II) compounds interplay with Cu(II) and Zn(II) coordination to the amyloid-beta peptide has metal specific consequences on deleterious processes associated to Alzheimer's disease*. Chem Commun (Camb), 2013. **49**(21): p. 2130-2.
82. Sasaki, I., et al., *Interference of a new cyclometallated Pt compound with Cu binding to amyloid-beta peptide*. Dalton Trans, 2012. **41**(21): p. 6404-7.
83. Kenche, V.B., et al., *Development of a platinum complex as an anti-amyloid agent for the therapy of Alzheimer's disease*. Angew Chem Int Ed Engl, 2013. **52**(12): p. 3374-8.
84. Bradley, Y.M., et al., *Group 9 metal-based inhibitors of β -amyloid (1-40) fibrillation as potential therapeutic agents for Alzheimer's disease*. Chemical Science, 2011. **2**: p. 917-921.
85. Messori, L., et al., *Promising in Vitro anti-Alzheimer Properties for a Ruthenium(III) Complex*. ACS Med Chem Lett, 2013. **4**(3): p. 329-32.
86. Valensin, D., et al., *fac-{Ru(CO)(3)}(2+) selectively targets the histidine residues of the beta-amyloid peptide 1-28. Implications for new Alzheimer's disease treatments based on ruthenium complexes*. Inorg Chem, 2010. **49**(11): p. 4720-2.

87. Kumar, A., et al., *Inhibition of Abeta42 peptide aggregation by a binuclear ruthenium(II)-platinum(II) complex: Potential for multi-metal organometallics as anti-amyloid agents.* ACS Chem Neurosci, 2010. **2010**(10): p. 691-701.
88. Man, B.Y.-W., et al., *Group 9 metal-based inhibitors of β -amyloid (1–40) fibrillation as potential therapeutic agents for Alzheimer's disease.* Chemical Science, 2011. **2**(5).
89. Heffern, M.C., et al., *Modulation of Amyloid-beta Aggregation by Histidine-coordinating Co(III) Schiff Base Complexes.* Chembiochem, 2014.
90. Jones, M.R., et al., *Modulation of the Abeta peptide aggregation pathway by KP1019 limits Abeta-associated neurotoxicity.* Metallomics, 2015. **7**(1): p. 129-35.
91. Yellol, G.S., et al., *Synthesis of 2-pyridyl-benzimidazole iridium(III), ruthenium(II), and platinum(II) complexes. study of the activity as inhibitors of amyloid-beta aggregation and neurotoxicity evaluation.* Inorg Chem, 2015. **54**(2): p. 470-5.
92. Lu, L., et al., *Inhibition of Beta-Amyloid Fibrillation by Luminescent Iridium(III) Complex Probes.* Sci Rep, 2015. **5**: p. 14619.
93. He, L., et al., *Methionine oxidation of amyloid peptides by peroxovanadium complexes: inhibition of fibril formation through a distinct mechanism.* Metallomics, 2015. **7**(12): p. 1562-72.
94. Wong, C., et al., *Dual inhibition and monitoring of beta-amyloid fibrillation by a luminescent iridium(III) complex.* Current Alzheimer Research, 2015. **12**(5): p. 439-444.
95. Chan, S.L., et al., *A novel tetradentate ruthenium(II) complex containing Tris(2-pyridylmethyl)amine (tpa) as an inhibitor of beta-amyloid fibrillation.* Current Alzheimer Research, 2015. **12**(5): p. 434-438.

96. Vyas, N.A., et al., *Ruthenium(II) polypyridyl complexes with hydrophobic ancillary ligand as Abeta aggregation inhibitors*. Eur J Med Chem, 2016. **121**: p. 793-802.
97. Conte-Daban, A., et al., *A metallo pro-drug to target Cu(II) in the context of Alzheimer's disease*. Chemistry, 2018.
98. Böttcher, A., et al., *Spectroscopy and Electrochemistry of Cobalt(III) Schiff Base Complexes*. Inorganic Chemistry, 1997. **36**(12): p. 2498-2504.
99. Harney, A.S., et al., *Targeted inhibition of Snail family zinc finger transcription factors by oligonucleotide-Co(III) Schiff base conjugate*. Proc. Natl. Acad. Sci. U. S. A., 2009. **106**(33): p. 13667-13672, S13667/1-S13667/3.
100. Harney, A.S., et al., *Targeted inhibition of Snail family zinc finger transcription factors by oligonucleotide-Co(III) Schiff base conjugate*. Proc Natl Acad Sci U S A, 2009. **106**(33): p. 13667-72.
101. Harney, A.S., T.J. Meade, and C. LaBonne, *Targeted Inactivation of Snail Family EMT Regulatory Factors by a Co(III)-Ebox Conjugate*. PLoS ONE, 2012. **7**(2): p. e32318.
102. Harney, A.S., T.J. Meade, and C. LaBonne, *Targeted inactivation of Snail family EMT regulatory factors by a Co(III)-Ebox conjugate*. PLoS One, 2012. **7**(2): p. e32318.
103. Heffern, M.C., J.W. Kurutz, and T.J. Meade, *Spectroscopic Elucidation of the Inhibitory Mechanism of Cys2His2 Zinc Finger Transcription Factors by Cobalt(III) Schiff Base Complexes*. Chem. - Eur. J., 2013. **19**(50): p. 17043-17053.
104. Heffern, M.C., et al., *Tuning cobalt(III) Schiff base complexes as activated protein inhibitors*. Inorg Chem, 2015. **54**(18): p. 9066-74.
105. Heffern, M.C., et al., *Modulation of Amyloid- β Aggregation by Histidine-Coordinating Cobalt(III) Schiff Base Complexes*. ChemBioChem, 2014. **15**(11): p. 1584-1589.

106. Heffern, M.C., et al., *Modulation of amyloid-beta aggregation by histidine-coordinating Cobalt(III) Schiff base complexes*. *Chembiochem*, 2014. **15**(11): p. 1584-9.
107. Hurtado, R.R., et al., *Specific inhibition of the transcription factor Ci by a cobalt(III) Schiff base-DNA conjugate*. *Mol Pharm*, 2012. **9**(2): p. 325-33.
108. Louie, A.Y. and T.J. Meade, *A cobalt complex that selectively disrupts the structure and function of zinc fingers*. *Proc Natl Acad Sci U S A*, 1998. **95**(12): p. 6663-8.
109. Manus, L.M., et al., *Axial ligand exchange of N-heterocyclic cobalt(III) Schiff base complexes: molecular structure and NMR solution dynamics*. *Inorg Chem*, 2013. **52**(2): p. 1069-76.
110. Matosziuk, L.M., et al., *Rational design of [Co(acacen)L2]⁺ inhibitors of protein function*. *Dalton Trans*, 2013. **42**(11): p. 4002-12.
111. Vistain, L.F., et al., *Targeted Inhibition of Snail Activity in Breast Cancer Cells by Using a CoIII-Ebox Conjugate*. *ChemBioChem*, 2015. **16**(14): p. 2065-2072.
112. Quintal, S.M., Q.A. de Paula, and N.P. Farrell, *Zinc finger proteins as templates for metal ion exchange and ligand reactivity. chemical and biological consequences*. *Metallomics*, 2011. **3**(2): p. 121-139.
113. Brayer, K.J. and D.J. Segal, *Keep your fingers off my DNA: protein-protein interactions mediated by C2H2 zinc finger domains*. *Cell Biochem. Biophys.*, 2008. **50**(3): p. 111-131.
114. Heffern, M.C., et al., *Cobalt derivatives as promising therapeutic agents*. *Current Opinion in Chemical Biology*, 2013. **17**: p. 189-196.
115. Hurtado, R.R., et al., *Specific Inhibition of the Transcription Factor Ci by a Cobalt(III) Schiff Base-DNA Conjugate*. *Molecular Pharmaceutics*, 2012. **9**: p. 325-333.

116. Dumurgier, J., et al., *Cerebrospinal fluid amyloid-beta 42/40 ratio in clinical setting of memory centers: a multicentric study*. *Alzheimers Res Ther*, 2015. **7**(1): p. 30.
117. Mawuenyega, K.G., et al., *Decreased clearance of CNS beta-amyloid in Alzheimer's disease*. *Science*, 2010. **330**(6012): p. 1774.
118. Head, E. and I.T. Lott, *Down syndrome and beta-amyloid deposition*. *Curr Opin Neurol*, 2004. **17**(2): p. 95-100.
119. Bateman, R.J., et al., *Autosomal-dominant Alzheimer's disease: a review and proposal for the prevention of Alzheimer's disease*. *Alzheimers Res Ther*, 2011. **3**(1): p. 1.
120. Xie, L., et al., *Sleep drives metabolite clearance from the adult brain*. *Science*, 2013. **342**(6156): p. 373-7.
121. Bilgel, M., et al., *Effects of amyloid pathology and neurodegeneration on cognitive change in cognitively normal adults*. *Brain*, 2018.
122. Knowles, T.P., et al., *An analytical solution to the kinetics of breakable filament assembly*. *Science*, 2009. **326**(5959): p. 1533-7.
123. Cohen, S.I., et al., *Nucleated polymerization with secondary pathways. III. Equilibrium behavior and oligomer populations*. *J Chem Phys*, 2011. **135**(6): p. 065107.
124. Cohen, S.I., et al., *Nucleated polymerization with secondary pathways. II. Determination of self-consistent solutions to growth processes described by non-linear master equations*. *J Chem Phys*, 2011. **135**(6): p. 065106.
125. Cohen, S.I., et al., *Nucleated polymerization with secondary pathways. I. Time evolution of the principal moments*. *J Chem Phys*, 2011. **135**(6): p. 065105.
126. Khurana, R., et al., *Mechanism of thioflavin T binding to amyloid fibrils*. *J Struct Biol*, 2005. **151**(3): p. 229-38.

127. Biancalana, M. and S. Koide, *Molecular mechanism of Thioflavin-T binding to amyloid fibrils*. *Biochim Biophys Acta*, 2010. **1804**(7): p. 1405-12.
128. Lee, S.J., et al., *Towards an understanding of amyloid-beta oligomers: characterization, toxicity mechanisms, and inhibitors*. *Chem Soc Rev*, 2017. **46**(2): p. 310-323.
129. Evangelisti, E., et al., *Binding affinity of amyloid oligomers to cellular membranes is a generic indicator of cellular dysfunction in protein misfolding diseases*. *Scientific Reports*, 2016. **6**: p. 32721.
130. Meisl, G., et al., *Molecular mechanisms of protein aggregation from global fitting of kinetic models*. *Nat Protoc*, 2016. **11**(2): p. 252-72.
131. Crespo, R., et al., *A generic crystallization-like model that describes the kinetics of amyloid fibril formation*. *J Biol Chem*, 2012. **287**(36): p. 30585-94.
132. Xue, C., et al., *Thioflavin T as an amyloid dye: fibril quantification, optimal concentration and effect on aggregation*. *R Soc Open Sci*, 2017. **4**(1): p. 160696.
133. Blennow, K., M.J. de Leon, and H. Zetterberg, *Alzheimer's disease*. *Lancet*, 2006. **368**(9533): p. 387-403.
134. Mattson, M.P., *Pathways towards and away from Alzheimer's disease*. *Nature*, 2004. **430**(7000): p. 631-9.
135. Jakob-Roetne, R. and H. Jacobsen, *Alzheimer's disease: from pathology to therapeutic approaches*. *Angew Chem Int Ed Engl*, 2009. **48**(17): p. 3030-59.
136. Pauwels, K., et al., *Structural basis for increased toxicity of pathological abeta42:abeta40 ratios in Alzheimer disease*. *J Biol Chem*, 2012. **287**(8): p. 5650-60.
137. Benseny-Cases, N., O. Klementieva, and J. Cladera, *In vitro oligomerization and fibrillogenesis of amyloid-beta peptides*. *Subcell Biochem*, 2012. **65**: p. 53-74.

138. Tickler, A.K., et al., *Methylation of the imidazole side chains of the Alzheimer disease amyloid-beta peptide results in abolition of superoxide dismutase-like structures and inhibition of neurotoxicity*. J Biol Chem, 2005. **280**(14): p. 13355-63.
139. Poduslo, J.F., et al., *HH domain of Alzheimer's disease Abeta provides structural basis for neuronal binding in PC12 and mouse cortical/hippocampal neurons*. PLoS One, 2010. **5**(1): p. e8813.
140. Dorlet, P., et al., *Pulse EPR spectroscopy reveals the coordination sphere of copper(II) ions in the 1-16 amyloid-beta peptide: a key role of the first two N-terminus residues*. Angew Chem Int Ed Engl, 2009. **48**(49): p. 9273-6.
141. Man, B.Y.-W., et al., *Group 9 metal-based inhibitors of β -amyloid (1-40) fibrillation as potential therapeutic agents for Alzheimer's disease*. Chemical Science, 2011. **2**(5): p. 917-921.
142. Heffern, M.C., J.W. Kurutz, and T.J. Meade, *Spectroscopic elucidation of the inhibitory mechanism of Cys2His2 zinc finger transcription factors by cobalt(III) Schiff base complexes*. Chemistry, 2013. **19**(50): p. 17043-53.
143. Qiao, Y., et al., *A computational study of self-assembled hexapeptide inhibitors against amyloid- β ($A\beta$) aggregation*. Physical Chemistry Chemical Physics, 2017. **19**(1): p. 155-166.
144. Lemkul, J.A. and D.R. Bevan, *Destabilizing Alzheimer's Abeta(42) protofibrils with morin: mechanistic insights from molecular dynamics simulations*. Biochemistry, 2010. **49**(18): p. 3935-46.
145. Triguero, L., R. Singh, and R. Prabhakar, *Molecular dynamics study to investigate the effect of chemical substitutions of methionine 35 on the secondary structure of the amyloid*

- beta (Abeta(1-42)) monomer in aqueous solution. J Phys Chem B, 2008. 112(7): p. 2159-67.*
146. Buchete, N.V., R. Tycko, and G. Hummer, *Molecular dynamics simulations of Alzheimer's beta-amyloid protofilaments. J Mol Biol, 2005. 353(4): p. 804-21.*
147. Wu, C., J. Scott, and J.E. Shea, *Binding of Congo red to amyloid protofibrils of the Alzheimer Abeta(9-40) peptide probed by molecular dynamics simulations. Biophys J, 2012. 103(3): p. 550-7.*
148. de Almeida, N.E.C., et al., *1,2,3,4,6-penta-O-galloyl-beta-D-glucopyranose Binds to the N-terminal Metal Binding Region to Inhibit Amyloid beta-protein Oligomer and Fibril Formation. Int J Mass Spectrom, 2017. 420: p. 24-34.*
149. Urbanc, B., et al., *In silico study of amyloid beta-protein folding and oligomerization. Proc Natl Acad Sci U S A, 2004. 101(50): p. 17345-50.*
150. Bellesia, G. and J.E. Shea, *Self-assembly of beta-sheet forming peptides into chiral fibrillar aggregates. J Chem Phys, 2007. 126(24): p. 245104.*
151. Hanwell, M.D., et al., *Avogadro: an advanced semantic chemical editor, visualization, and analysis platform. J Cheminform, 2012. 4(1): p. 17.*
152. Schmidt, M.W., et al., *General atomic and molecular electronic structure system. Journal of Computational Chemistry, 1993. 14(11): p. 1347-1363.*
153. Becke, A.D., *Density-functional thermochemistry. III. The role of exact exchange. The Journal of Chemical Physics, 1993. 98(7): p. 5648-5652.*
154. Lee, C., W. Yang, and R.G. Parr, *Development of the Colle-Salvetti correlation-energy formula into a functional of the electron density. Physical Review B, 1988. 37(2): p. 785-789.*

155. Ali-Torres, J., et al., *Structures and stabilities of Fe^{2+/3+} complexes relevant to Alzheimer's disease: an ab initio study*. J Phys Chem A, 2011. **115**(45): p. 12523-30.
156. Bayly, C.I., et al., *A well-behaved electrostatic potential based method using charge restraints for deriving atomic charges: the RESP model*. The Journal of Physical Chemistry, 1993. **97**(40): p. 10269-10280.
157. Case, D.A., et al., *AMBER 2016*. 2016: University of California, San Francisco.
158. Wang, J., et al., *Development and testing of a general amber force field*. J Comput Chem, 2004. **25**(9): p. 1157-74.
159. Cheatham, T.E., 3rd and P.A. Kollman, *Insight into the stabilization of A-DNA by specific ion association: spontaneous B-DNA to A-DNA transitions observed in molecular dynamics simulations of d[ACCCGCGGGT]₂ in the presence of hexaamminecobalt(III)*. Structure, 1997. **5**(10): p. 1297-311.
160. Berendsen, H.J.C., D. van der Spoel, and R. van Drunen, *GROMACS: A message-passing parallel molecular dynamics implementation*. Computer Physics Communications, 1995. **91**(1): p. 43-56.
161. Abraham, M.J., et al., *GROMACS: High performance molecular simulations through multi-level parallelism from laptops to supercomputers*. SoftwareX, 2015. **1-2**: p. 19-25.
162. Lindorff-Larsen, K., et al., *Improved side-chain torsion potentials for the Amber ff99SB protein force field*. Proteins, 2010. **78**(8): p. 1950-8.
163. Crescenzi, O., et al., *Solution structure of the Alzheimer amyloid beta-peptide (1-42) in an apolar microenvironment. Similarity with a virus fusion domain*. Eur J Biochem, 2002. **269**(22): p. 5642-8.

164. Jorgensen, W.L., et al., *Comparison of simple potential functions for simulating liquid water*. The Journal of Chemical Physics, 1983. **79**(2): p. 926-935.
165. Hess, B., *P-LINCS: A Parallel Linear Constraint Solver for Molecular Simulation*. Journal of Chemical Theory and Computation, 2008. **4**(1): p. 116-122.
166. Bussi, G., D. Donadio, and M. Parrinello, *Canonical sampling through velocity rescaling*. J Chem Phys, 2007. **126**(1): p. 014101.
167. Nosé, S. and M.L. Klein, *Constant pressure molecular dynamics for molecular systems*. Molecular Physics, 1983. **50**(5): p. 1055-1076.
168. Parrinello, M. and A. Rahman, *Polymorphic transitions in single crystals: A new molecular dynamics method*. Journal of Applied Physics, 1981. **52**(12): p. 7182-7190.
169. Grubmüller, H., et al., *Generalized Verlet Algorithm for Efficient Molecular Dynamics Simulations with Long-range Interactions*. Molecular Simulation, 1991. **6**(1-3): p. 121-142.
170. Darden, T., D. York, and L. Pedersen, *Particle mesh Ewald: An $N \log(N)$ method for Ewald sums in large systems*. The Journal of Chemical Physics, 1993. **98**(12): p. 10089-10092.
171. Essmann, U., et al., *A smooth particle mesh Ewald method*. The Journal of Chemical Physics, 1995. **103**(19): p. 8577-8593.
172. Kabsch, W. and C. Sander, *Dictionary of protein secondary structure: pattern recognition of hydrogen-bonded and geometrical features*. Biopolymers, 1983. **22**(12): p. 2577-637.
173. Humphrey, W., A. Dalke, and K. Schulten, *VMD: Visual molecular dynamics*. Journal of Molecular Graphics, 1996. **14**(1): p. 33-38.
174. Larini, L. and J.E. Shea, *Role of beta-hairpin formation in aggregation: the self-assembly of the amyloid-beta(25-35) peptide*. Biophys J, 2012. **103**(3): p. 576-86.

175. Kochanczyk, T., A. Drozd, and A. Krezel, *Relationship between the architecture of zinc coordination and zinc binding affinity in proteins--insights into zinc regulation*. Metallomics, 2015. **7**(2): p. 244-57.
176. Borghesani, V., B. Alies, and C. Hureau, *Cu(II) binding to various forms of amyloid-beta peptides. Are they friends or foes?* Eur J Inorg Chem, 2018. **2018**(1): p. 7-15.
177. Roychaudhuri, R., et al., *Amyloid beta-protein assembly and Alzheimer disease*. J Biol Chem, 2009. **284**(8): p. 4749-53.
178. Butterfield, D.A., et al., *Evidence that amyloid beta-peptide-induced lipid peroxidation and its sequelae in Alzheimer's disease brain contribute to neuronal death*. Neurobiol Aging, 2002. **23**(5): p. 655-64.
179. Williams, T.L. and L.C. Serpell, *Membrane and surface interactions of Alzheimer's A β peptide--insights into the mechanism of cytotoxicity*. FEBS J, 2011. **278**(20): p. 3905-17.
180. Butterfield, D.A., et al., *Roles of amyloid beta-peptide-associated oxidative stress and brain protein modifications in the pathogenesis of Alzheimer's disease and mild cognitive impairment*. Free Radic Biol Med, 2007. **43**(5): p. 658-77.
181. Jomova, K., et al., *Metals, oxidative stress and neurodegenerative disorders*. Mol Cell Biochem, 2010. **345**(1-2): p. 91-104.
182. Haeffner, F., et al., *Model studies of cholesterol and ascorbate oxidation by copper complexes: relevance to Alzheimer's disease beta-amyloid metallochemistry*. J Inorg Biochem, 2005. **99**(12): p. 2403-22.
183. Williams, T.I., et al., *Increased levels of 4-hydroxynonenal and acrolein, neurotoxic markers of lipid peroxidation, in the brain in Mild Cognitive Impairment and early Alzheimer's disease*. Neurobiol Aging, 2006. **27**(8): p. 1094-9.

184. Pamplona, R., et al., *Proteins in human brain cortex are modified by oxidation, glycooxidation, and lipoxidation. Effects of Alzheimer disease and identification of lipoxidation targets.* J Biol Chem, 2005. **280**(22): p. 21522-30.
185. Chromy, B.A., et al., *Self-assembly of Abeta(1-42) into globular neurotoxins.* Biochemistry, 2003. **42**(44): p. 12749-60.
186. Manevich, Y., K.D. Held, and J.E. Biaglow, *Coumarin-3-carboxylic acid as a detector for hydroxyl radicals generated chemically and by gamma radiation.* Radiat Res, 1997. **148**(6): p. 580-91.
187. Pollard, T.D., *A guide to simple and informative binding assays.* Mol Biol Cell, 2010. **21**(23): p. 4061-7.
188. Skoumalová, A. and J. Hort, *Blood markers of oxidative stress in Alzheimer's disease.* J Cell Mol Med, 2012. **16**(10): p. 2291-300.
189. Zito, K., et al., *Rapid functional maturation of nascent dendritic spines.* Neuron, 2009. **61**(2): p. 247-58.
190. Knott, G.W., et al., *Spine growth precedes synapse formation in the adult neocortex in vivo.* Nat Neurosci, 2006. **9**(9): p. 1117-24.
191. Kwon, H.B. and B.L. Sabatini, *Glutamate induces de novo growth of functional spines in developing cortex.* Nature, 2011. **474**(7349): p. 100-4.
192. Nagerl, U.V., et al., *Protracted synaptogenesis after activity-dependent spinogenesis in hippocampal neurons.* J Neurosci, 2007. **27**(30): p. 8149-56.
193. Scotuzzi, M., et al., *Multi-color electron microscopy by element-guided identification of cells, organelles and molecules.* Scientific Reports, 2017. **7**(1).

194. Adams, S.R., et al., *Multicolor Electron Microscopy for Simultaneous Visualization of Multiple Molecular Species*. *Cell Chem Biol*, 2016. **23**(11): p. 1417-1427.
195. Sonzini, S., et al., *Simple fluorinated moiety insertion on Abeta 16-23 peptide for stain-free TEM imaging*. *Analyst*, 2015. **140**(8): p. 2735-40.
196. Preslar, A.T., et al., *(19)F Magnetic Resonance Imaging Signals from Peptide Amphiphile Nanostructures Are Strongly Affected by Their Shape*. *ACS Nano*, 2016. **10**(8): p. 7376-84.
197. Williams, P.E., et al., *A facile method for the stain-free visualization of hierarchical structures with electron microscopy*. *Journal of Polymer Science Part A: Polymer Chemistry*, 2015. **53**(7): p. 842-845.
198. Comitz, R.L., Y.P. Ouedraogo, and N. Nesnas, *Unambiguous evaluation of the relative photolysis rates of nitro indolanyl protecting groups critical for brain network studies*. *Analytical Chemistry Research*, 2015. **3**: p. 20-25.
199. Nogales, E., *Cryo-EM*. *Curr Biol*, 2018. **28**(19): p. R1127-R1128.

KALEIGH FILISA ROBERTS

Telephone: 618-363-4321 Email: kaleigh-roberts@northwestern.edu

EDUCATION

- 2013 – present Ph.D. Candidate
Interdisciplinary Biological Sciences Program
Northwestern University
GPA: 4.00/4.00
Evanston, IL
- 2011 – present M.D. Candidate
Medical Scientist Training Program
Northwestern University Feinberg School of Medicine
Chicago, IL
- 2006 – 2011 B.S. Bioengineering with High Honors Minor: Chemistry
University of Illinois at Urbana-Champaign
GPA: 3.87/4.00
Champaign, IL

RESEARCH EXPERIENCE

- 2013 - present Thesis Research, Advisor: Tom Meade Ph.D.
Northwestern University, Department of Chemistry
 - Cobalt-based inhibitors of metal-mediated amyloid- β toxicity in Alzheimer's disease
 - Photoactivatable contrast agents for transmission electron microscopy
- 2012 Research Rotation, Advisor: Lester Binder Ph.D.
Northwestern University, Department of Cellular and Molecular Biology
 - The role of tau oligomers in Alzheimer's disease and traumatic brain injury
- 2010 – 2011 Statistical Data Analyst, Advisor: Randall Bateman M.D.
Washington University School of Medicine, Department of Neurology
 - Brain efflux of amyloid- β
- 2008 – 2010 Undergraduate Research, Advisor: Paul Gold Ph.D.
University of Illinois at Urbana-Champaign, Neuroscience Program
 - Glucose and epinephrine modulation of age-related memory impairment

TEACHING EXPERIENCE

- 2015 Biochemistry Teaching Assistant
Northwestern University, Department of Biological Sciences
- 2008 – 2010 General Chemistry Teaching Assistant
University of Illinois at Urbana-Champaign, Department of Chemistry
 - Sole responsibility for teaching Discussion section
- 2008 Engineering Orientation Teaching Assistant
University of Illinois at Urbana-Champaign, Department of Bioengineering

CLINICAL EXPERIENCE

- 2013 OB/GYN Clerkship
Stroger Hospital
Chicago, IL

AWARDS AND HONORS

- 2017 Highest Recruiter to Alzheimer's TrialMatch in Chicago Metro

KALEIGH FILISA ROBERTS

Telephone: 618-363-4321 Email: kaleigh-roberts@northwestern.edu

2016	Department of Defense Peer Reviewed Cancer Research Program Horizon Award
2015	Illinois Hospitals Research and Education Foundation Scholarship
2014	Alumnae of Northwestern Grant
2010	School of Chemical Sciences Teaching Scholarship
2008 – 2010	List of Teachers Ranked as Excellent by their Students
2007 – 2010	Dean's List
2006 – 2010	Edmund J. James Scholar Honors in Engineering
2006 – 2010	Corporate Actions Division Scholarship
2008	St. Nicholas Scholarship
2006	National Merit Scholar
2006	Illinois State Scholar
2006	American Hellenic Educational Progressive Association Scholarship

CERTIFICATIONS

2011 – present	BLS for Healthcare Providers (CPR and AED)
2010	Six Sigma

ACTIVITIES AND AFFILIATIONS

2014 – present	Alzheimer's Association Community Representative, Greater Illinois Chapter
2010 – present	Volunteer Radio Reader, Mindseye Information Service
2013 – 2015	Health and Science Educator, Cook County Jail
2011 – 2013	MSTP Student Council, Feinberg Senate Representative 2011
2011 – 2012	Alzheimer's Buddy Program, Northwestern University CNADC
2010 – 2011	Fairview Heights Public Library Trustee
2010 – 2011	Alzheimer's Association Health Fair Representative, St. Louis Chapter
2010 – 2011	Alzheimer's Association Illinois Young Professionals, St. Louis Chapter

PUBLICATIONS

Roberts KF, Brue CR, Preston AG, Baxter, DN, Hertzog E, Varelas E, Heffern MC, Roth E, Meade TJ. "Inhibition of amyloid- β aggregation and toxicity by cobalt(III) Schiff base." (In preparation).

Isken A*, Kim J*, **Roberts KF***, Brue CR, Schatz G, Meade TJ. "Inhibition of Amyloid- β Aggregation by Cobalt(III) Schiff Base Complexes: A Computational and Experimental Approach." (In preparation).

*authors contributed equally to this work

Bajema E, **Roberts KF**, Meade TJ. "Cobalt-Schiff Base Complexes: Preclinical Research and Potential Therapeutic Uses. Metal Ions in Life Sciences." Volume 19, Edited by Astrid Sigel, Eva Freisinger, and Roland K. O. Sigel. © Walter de Gruyter GmbH, Berlin, Germany 2019, www.mils-WdG.com.

Roberts KF, Elbert DL, Kasten T, Patterson BW, Sigurdson W, Connors R, Ovod V, Munsell L, Mawuenyega K, Miller-Thomas MM, Moran CJ, Cross DT, Derdeyn CP, Bateman RJ. "Amyloid- β efflux from the CNS into the plasma." *Annals of Neurology*. 76(6):837-844, 2014. PMID: PMC4355962.

Ward SM, Himmelstein DS, Ren Y, Fu Y, Yu XW, **Roberts K**, Binder LI, Sahara N. "TOCI: A valuable tool in assessing the disease progression in the rTg4510 mouse model of tauopathy." *Neurobiology of Disease*. 67:37-48, 2014. PMID: PMC4055868.

Vidula MK*, Wadhvani A*, **Roberts K***, Berkowitz L. "Use of a Once Daily NSAID in Treatment of Cyclic Vomiting Syndrome." *Journal of General Internal Medicine*. 29:543-546, 2014. PMID: PMC3930795.

*authors contributed equally to this work

KALEIGH FILISA ROBERTS

Telephone: 618-363-4321 Email: kaleigh-roberts@northwestern.edu

POSTERS

Roberts K, Brue C, Preslar A, Lilley L, Varelas E, Preston A, Wilke C, Meade TJ. "TEMarkers: Photoactivatable contrast agents to investigate synaptogenesis by transmission electron microscopy." Poster Presentation. 2016 Imaging in 2020 Conference. Jackson Hole, WY.

Roberts KF, Heffern M, Meade TJ. "Cobalt(III) Schiff base complexes as inhibitors of metal-mediated amyloid- β toxicity in Alzheimer's disease." Poster Presentation. 2014 Drug Discovery Symposium. Northwestern University.

Roberts KF, Morris KA, Gold PE. "Age-related changes in alpha-endosulfine, an endogenous K-ATP channel modulator." Poster Presentation. 2010 Undergraduate Research Symposium. University of Illinois at Urbana Champaign.

Roberts KF*, Blum S*. "A pinpression device for MRI head placement." Poster Presentation. 2010 Bioengineering Day. University of Illinois at Urbana-Champaign.

*authors contributed equally to this work

Gupta R*, Koval J*, **Roberts K***, Saggere L. "Microelectromechanical systems: Applications to microactuators and microgrippers." Poster Presentation. 2005 IMSAloquium. Illinois Mathematics and Science Academy.

*authors contributed equally to this work